



Synthesis and study of the optical, structural and morphological properties of TiO₂:Co alloys prepared by Co-Sputtering

Andrés Jhovanny Bohórquez Garzón

Universidad Nacional de Colombia
Science Faculty, Physics Department
Bogotá, Colombia

2018

Synthesis and study of the optical, structural and morphological properties of TiO₂:Co alloys prepared by Co-Sputtering

Andrés Jhovanny Bohórquez Garzón

Thesis presented as a partial requisite to apply for the title of:

Master in Science - Physics

Director:

Ph.D., Anderson Dussan Cuenca

Line of Research:

Diluted Magnetic Semiconductors

Research Group:

Nanostructured Materials and Their Applications

Universidad Nacional de Colombia
Science Faculty, Physics Department
Bogotá, Colombia

2018

To my parents

Acknowledgements

Having taken another important step in my academic, scientific career, I would like to express my most sincere gratitude to my parents, Jose Ignacio Bohórquez Bohórquez and Betty Garzón Naranjo, without which this entire work would not have had the meaning it now holds to me, and whom have been my main motivation for the completion of my very own goals and life projects; to them, I have nothing more to give than my uttermost respect and compromise.

To my sister and brother, whom along my entire life have always been a source of motivation and personal overcoming, I hold for them tremendous gratitude and respect for being so distinguished in their own academic fields, and I always procure to be at their level, because I know that if they can perform the way they do in their respective areas of work, then it means that I can also distinguish myself as a materials science researcher.

To the Group of Nanostructured Materials and their Applications, especially to professor Anderson Dussan, I would also like to offer my gratitude and compromise in the different scientific goals it has set for itself. Without the academic, economic, and overall tremendous support from this research group, the work presented in the next pages would not have taken place. My group mates have been tremendously helpful in this stage of my life, and I would like to thank the time they spent with me, analyzing, discussing and brainstorming through days filled with knowledge, camaraderie and overall fun. This work was supported by Universidad Nacional de Colombia DIB – Project Code Quipú 201010026991 and COLCIENCIAS – Project Code Quipú 201010020943

Last, but absolutely not least, to the love of my life Camila, this work is also dedicated to her, because without her unconditional support, care and motivation I could not have taken this step in my life. To her I express my unwavering love, knowing that every future steps I take in my life would have a greater meaning if she is present in them, starting with the finalization of this work.

Abstract

In this work, cobalt-doped titanium dioxide thin films were synthesized using the advantageous DC Magnetron Co-sputtering method varying different fabrication parameters like deposition time, substrate temperature and type of substrate employed; a portion of the fabricated samples was then subject to annealing processes in uncontrolled atmosphere. The resulting material was an opaque, seemingly uniform thin film of black appearance which became more transparent and brown-like after annealing at temperatures beyond 500 °C. The fabricated samples were submitted to structural, morphological, optical, compositional and magnetic characterizations, evidencing a limited crystallization, low grain size (less than 200 nm), elevated reflectance (up to 95% in the IR region), low transmittance (less than 0.8% for cobalt-containing samples) and superparamagnetic behavior of the as-deposited thin films, which, after the annealing processes were performed, became severely more crystalline, transparent and increased their grain size (reaching values of even 1000 nm), maintaining its granular morphology in the surface. Cobalt oxide (Co₃O₄) and cobalt titanate (CoTi₂O₅) were among the crystalline phases found via X-ray diffraction, the latter pertaining a spinel-like structure in which the cobalt atoms exist in two separate oxidation states, namely +2 and +3. These results prompted the successful conclusion of the fabrication of an intermetallic alloy thin film, which in turn supports one of the main contributions of this work to the materials science research field. The synthesis of the ternary CoTi₂O₅ phase with this configuration of the sputtering technique had not, until now, yet been reported.

Keywords: Titanium dioxide, intermetallic alloy, X-ray diffraction, PPMS, sputtering.

Resumen

En este trabajo, se fabricaron películas delgadas de dióxido de titanio dopado con cobalto usando el ventajoso método de la co-pulverización catódica asistida por campo magnético variando distintos parámetros de fabricación tales como el tiempo de depósito, temperatura de sustrato y el tipo de sustrato empleado; una porción de las muestras fabricadas fue sometida a procesos de recocido en atmósfera no controlada. El material resultante fueron películas delgadas de apariencia opaca, visiblemente uniformes y de color negro las cuales se tornaron más transparentes y de color café luego de recocerlas a temperaturas mayores a 500 °C. Las muestras fabricadas fueron sometidas a caracterizaciones de tipo estructural, morfológico, óptico, composicional y magnético, evidenciando una cristalización limitada, bajo tamaño de grano (inferior a 200 nm), reflectancia elevada (hasta 95% en la región IR), baja transmitancia (menor a 0.8% para muestras que contenían cobalto) y comportamiento superparamagnético para las películas depositadas, las cuales luego de aplicar los procesos de recocido, se tornaron más cristalinas, transparentes e incrementaron su tamaño de grano (alcanzando valores incluso de 1000 nm), manteniendo su morfología granular en la superficie. Se identificaron fases cristalinas de óxido de cobalto (Co_3O_4) y titanato de cobalto (CoTi_2O_5) usando la técnica de difracción de rayos-X; la primera de ellas exhibe una estructura tipo espinel, en la cual los átomos de cobalto existen en dos estados de oxidación separados, a saber: +2 y +3. Los anteriores resultados llevaron a la exitosa conclusión de la fabricación de películas delgadas hechas de una aleación intermetálica, lo cual constituye una de las principales contribuciones de éste trabajo a la ciencia de materiales. La síntesis de la fase ternaria CoTi_2O_5 con esta configuración de la técnica de pulverización catódica no había sido, hasta el momento, reportada.

Palabras claves: Dióxido de titanio, aleación intermetálica, difracción de rayos-X, PPMS, pulverización catódica.

Table of contents

	<u>Pág.</u>
1. Theoretical aspects	3
1.1 State of the art	3
1.2 Properties of impurity-doped TiO ₂	7
1.3 Fabrication reports of the TiO ₂ :Co compound.....	9
1.4 Structural properties of materials	12
1.5 Morphological and topographical properties of materials.....	17
1.6 Optical properties of materials.....	21
1.7 Physical properties of TiO ₂ and Co	24
2. Experimental aspects	27
2.1 Fabrication and synthesis parameters of the TiO ₂ :Co alloys	27
2.2 Characterization techniques.....	35
2.2.1 X-Ray diffraction.....	35
2.2.2 Scanning electron microscopy (SEM).....	40
2.2.3 Atomic force microscopy	44
2.2.4 UV-Vis-NIR spectroscopy.....	47
3. Results and discussion.....	51
3.1 Structural characterization	51
3.1.1 Characterization of as-deposited thin films	51
3.1.2 Characterization of thin films subject to annealing processes	55
3.2 Morphological and topographical characterization	62
3.2.1 SEM characterization of as-deposited thin films.....	62
3.2.2 SEM characterization of annealed thin films	69
3.2.3 AFM study.....	73
3.3 Optical characterization	75
3.3.1 Characterization of as-deposited thin films	76
3.3.2 Characterization of annealed thin films.....	80
3.4 Additional characterizations.....	89
3.4.1 XPS measurements	89
3.4.2 PPMS measurements	91
4. Conclusions and perspectives	95
4.1 Conclusions.....	95
4.2 Perspectives	96

List of figures

Pág.

Fig. 1-1: Diffraction pattern of a polycrystalline titanium foil sample. Results are generally presented as Intensity vs. 2θ	14
Fig. 1-2: SEM micrograph of potato starch particles [49].....	18
Fig. 1-3: Band diagram for: a) A conducting material, b) a semiconductor material and c) an insulating material [57].	25
Fig. 2-1: Particle mean free path as a function of the system pressure [61].....	28
Fig. 2-2: Voltage behavior as a function of the electric current of a gas inside a vacuum chamber. Region A indicates the ideal conditions for sputtering to occur [61]......	29
Fig. 2-3: Schematic diagram of the Magnetron Sputtering method [61]......	30
Fig. 2-4: Schematic diagram of the DC Magnetron Co-Sputtering technique.	31
Fig. 2-5: a) X-Ray tube diagram. 1) Cathode, 2) Focus, 3) Anode, 4) Vacuum environment, 5) Diaphragm, 6) X-Ray beam, b) Operation schematics of an X-Ray diffractometer [65].	35
Fig. 2-6: Diagram of the X-Ray emission process by electronic incidence [67]......	37
Fig. 2-7: Diagram of the X-Ray emission process by photonic incidence. Two incident waves are reflected with the same phase from the sample.	38
Fig. 2-8: X-Ray diffraction pattern of: a) A monocrystal (ZnO over a glass substrate) [68] and b) Amorphous soda-lime glass [69]......	38
Fig. 2-9: Block diagram of a SEM equipment.....	40
Fig. 2-10: Schematic diagram of the interaction between the incident electrons and the surface of a sample. The different types of particles emitted from it are also presented [72].	42
Fig. 2-11: Diagram of the Lennard-Jones potential for two interacting particles [75]......	46
Fig. 2-12: Typical operation modes of an AFM microscope [76]......	47
Fig. 2-13: Block diagram of an UV-Vis-NIR spectrophotometer. Black arrows show the path that light undergoes inside the apparatus.	48
Fig. 3-1: Comparative diffractograms of samples deposited on: a) Titanium foil, b) Soda-lime glass and c) Silicon wafer.	52
Fig. 3-2: Diffractograms of the samples from Series 2 deposited on: a) Titanium foil, b) Soda-lime glass and c) Silicon wafer.	53
Fig. 3-3: Diffractograms of the samples from Series 4 deposited on: a) Titanium foil, b) Soda-lime glass and c) Silicon wafer.	54
Fig. 3-4: Comparative diffractograms of samples annealed at $500\text{ }^{\circ}\text{C}$	56
Fig. 3-5: Comparative diffractograms of samples annealed at $550\text{ }^{\circ}\text{C}$	57
Fig. 3-6: Comparative diffractograms of samples annealed at $600\text{ }^{\circ}\text{C}$	58

Fig. 3-7: Diffractograms of the Series 2 samples annealed at: a) 550 °C and b) 600 °C for 5 hours.....	59
Fig. 3-8: Phase diagram of the CoO-TiO ₂ system.	60
Fig. 3-9: Diffractograms of the Series 4 samples annealed at: a) 550 °C and b) 600 °C for 5 hours.....	61
Fig. 3-10: SEM micrographs of samples from Series 1 deposited on: a) Titanium foil, b) Glass and c) Silicon wafer.	63
Fig. 3-11: SEM micrographs of samples from Series 2 deposited on: a) Titanium foil, b) Glass and c) Silicon wafer. Deposition time was 15 minutes.....	64
Fig. 3-12: SEM micrographs of samples from Series 2 deposited on: a) Titanium foil, b) Glass and c) Silicon wafer. Deposition time was 30 minutes.....	65
Fig. 3-13: SEM micrographs of samples from Series 2 deposited on: a) Titanium foil, b) Glass and c) Silicon wafer. Deposition time was 45 minutes.....	66
Fig. 3-14: SEM micrographs of samples from Series 3 deposited on: a) Titanium foil, b) Glass and c) Silicon wafer. Deposition time was 30 minutes.....	67
Fig. 3-15: SEM micrographs of samples from Series 4 deposited on: a) Titanium foil, b) Glass and c) Silicon wafer. Substrate temperature was 100 °C.....	68
Fig. 3-16: SEM micrographs taken of samples from: a) Series 1, b) Series 2 (30 min) and c) Series 3, annealed at 600 °C for 5 hours.....	69
Fig. 3-17: SEM micrographs taken from the annealed second series of fabrication using: a) 15 minutes, b) 30 minutes and c) 45 minutes of deposition time.....	70
Fig. 3-18: SEM micrographs taken from the annealed fourth series of fabrication using: a) 250 °C and b) 100 °C T_s . Inset shows a magnification of the sample with 100 °C T_s	71
Fig. 3-19: a) SEM micrograph of a TiO ₂ :Co thin film deposited with 15 minutes t_d and b) HR-SEM transversal micrograph of the TiO ₂ :Co thin film with 30 minutes t_d	73
Fig. 3-20: AFM micrograph of an as-deposited TiO ₂ :Co thin film deposited on glass.....	74
Fig. 3-21: a) AFM micrograph of a TiO ₂ :Co thin film annealed at 600 °C for 5 hours in uncontrolled atmosphere, b) Distribution of the height points over the thin film surface.	75
Fig. 3-22: Specular reflectance measurements of the: a) TiO ₂ and b) Co thin films deposited on the three different substrates.	77
Fig. 3-23: Specular reflectance measurements of the TiO ₂ :Co thin films using a) 15 min. b) 30 min and c) 45 min of deposition time, over the three distinct substrates.	78
Fig. 3-24: Specular reflectance measurements of the TiO ₂ :Co thin films using a) 100 °C and b) 250 °C substrate temperature, over the three distinct substrates.	79
Fig. 3-25: Transmittance spectra for samples deposited on glass from Series 1 (blue) Series 2 (red) and Series 3 (black). Inset shows an amplification of the low transmittance region...80	80
Fig. 3-26: Transmittance spectra of the thin films from Series 1, 2 (30 min.) and 3 annealed after deposition at: a) 500 °C and b) 550 °C in an air atmosphere.....	81
Fig. 3-27: Transmittance spectra of the thin films from Series 1, 2 (30 min.) and 3 annealed after deposition at 600 °C in an air atmosphere.....	82
Fig. 3-28: Transmittance spectra of the thin films from Series 2 annealed after deposition at: a) 500 °C and b) 550 °C in an air atmosphere.	83

Fig. 3-29: Transmittance spectra of the thin films from Series 2 annealed after deposition at 600 °C in an air atmosphere.	84
Fig. 3-30: Transmittance spectra of the thin films from Series 4 annealed after deposition at: a) 500 °C and b) 550 °C in an air atmosphere.	85
Fig. 3-31: Transmittance spectra of the thin films from Series 4 annealed after deposition at 600 °C in an air atmosphere.	86
Fig. 3-32: $(\alpha h\nu)^{1/2}$ vs. $(h\nu)$ plot for a TiO ₂ thin film from series 1 annealed at 600 °C for 5 hours.	87
Fig. 3-33: $(\alpha h\nu)^{1/2}$ vs. $(h\nu)$ plot for: a) TiO ₂ :Co thin film from series 2 (15 min.) annealed at 500 °C and b) TiO ₂ :Co thin film from series 4 (100 °C) annealed at 500 °C.	88
Fig. 3-34: XPS spectra of an annealed TiO ₂ :Co thin film using a t_d of 30 minutes. Insets a) and b) highlight the Co 2p and Ti 2p peaks of the spectrum, respectively.	90
Fig. 3-35: PPMS measurement of an as-deposited TiO ₂ :Co thin film from Series 2, using a t_d of 30 minutes, the data was collected at a sample temperature of a) 4 K and b) 50 K.	93
Fig. 3-36: PPMS measurement of an as-deposited TiO ₂ :Co thin film from Series 2, using a t_d of 30 minutes, the data was collected at a sample temperature of a) 150 K and b) 300 K.	94

List of tables

	<u>Pág.</u>
Table 1-1: Physical properties of cobalt [56].	25
Table 1-2: Physical properties of titanium dioxide [2].	26
Table 2-1: Synthesis parameters used in the fabrication of the samples presented in this work.	34
Table 3-1: Gap energies calculates for the TiO ₂ :Co thin films deposited on glass.	88
Table 3-2: Elemental composition of a TiO ₂ :Co thin film measured via XPS data.....	90

Introduction

The science of materials is a constantly growing discipline within the entire scientific community. Nowadays it would seem like an eternity ago when William Shockley, Walter Brattain and John Bardeen were working in the Bell Laboratories on a suitable way to replace the energy consuming vacuum tubes that were used as one of the principal communications sources in the Second World War [1].

In the year 1951 they stumbled upon a revolutionary, low-cost, low-energy consuming device which is now present in virtually any type of electronic equipment we have now at our disposal: The transistor. This elegant and simple solution to the power consuming problem that the general public was encountering, was based on a straightforward juncture between very special materials, which in turn allowed the amplification or switching of electric signals and electric power. The effects it had on the quality of life and overall communications systems granted them the physics Nobel Prize in 1956, but perhaps even more important than the device itself and its global distribution, is the physical principle behind the transistor. A transistor rests on the particular, directional electron transfer processes that occur when two semiconductor materials are placed adjacent to each other; no other type of material was capable of doing the things that a semiconductor could, it was an innovative, new and exciting type of material whose physical properties and potential scope were only starting to be discovered; and if it were not for those three remarkable researchers and their filiation with the material science field we would not have made the tremendous, unbelievable progress we as human race have made in chemistry, electronics, photovoltaic devices, spintronics, space exploration, engineering, etcetera.

From that point forward, the investigation on material science became one of the most relevant lines of research for the academic community, the miniaturization and enhancement of the efficiency of electronic devices became one of the main objectives to accomplish. Anybody who would hold the most efficient and reliable device could reclaim their patent and stand on top

of its field, and it was probably this sort of competition that prompted the increased investigation on the discovery of new materials (not necessarily semiconductors), or even on the further research on the already known materials.

Within the framework of this past events, and with the progress of the material-science field of the country on sight, is where this entire work is founded. This thesis is the compilation of several disciplined, enlightening and sometimes exhausting hours of work and research on the extremely useful semiconductor material: Titanium dioxide (TiO₂). Understanding the physical properties of this semiconductor and the applications it offers is a truly exciting field of investigation for anyone involved in the physics area, and that is one of the reasons why this dissertation took place, along with the potential recognition it may hold for my research group.

However, this work is not only based on the study of the physical properties of TiO₂; research groups, too numerous to count, have already concerned themselves with this area, evaluating the properties of the material in bulk form, or as thin film form prepared by several methods of fabrication. It is clearly not the goal of this work the re-production of past research, rather to innovate in the field by synthesizing an intermetallic alloy of this semiconductor with a transition metal, namely: Cobalt; and it does so by using an advantageous deposition technique for thin films called the 'DC-Magnetron Co Sputtering' method, which has never been used before for the preparation of said alloy and therefore offers an un-scouted horizon for the investigation on semiconductor materials. This study is funded and performed within the Diluted Magnetic Semiconductor line of research.

The cobalt-doped titanium dioxide thin films were prepared varying different synthesis parameters in order to evaluate the potential change in their physical properties, which could not have been measured or studied if it were not for the remarkable resources the Universidad Nacional de Colombia offers, along with the special academic collaboration with other institutions such as the Universidad de los Andes and the Universidad del Valle. The results that this research brought were not only interesting and unpredictable, but they were also enlightening and I consider them to be an important contribution to my field of research. I can only hope that anyone who takes the time to analyze them would hold them in the same regard.

1. Theoretical aspects

Having shown at first glance the importance of this research, it is important to understand the theoretical framework surrounding this semiconductor because it will be one of the cornerstones in the development of this investigation. First, a compilation of the state of the art in TiO_2 research will be presented, followed by some aspects regarding transition metal-doped semiconductors, subsequently some relevant fabrication reports of the $\text{TiO}_2\text{:Co}$ material and lastly, a complete theoretical scope of the structural, optical and morphological properties of materials, along with the main physical properties of TiO_2 and Co .

1.1 State of the art

Titanium dioxide (TiO_2), also known as “Titania”, is a semiconductor material which can be found naturally in the crust of the earth in three characteristic crystalline forms: Rutile, Anatase and Brookite [2], the first one constitutes the most thermodynamically stable phase of TiO_2 , whilst the other two correspond to metastable phases. The extraction of this compound is carried out parting from the mineral known as Ilmenite [2], which is chemically processed to remove the iron oxide groups present in the rock and subsequently crystallize and filter the iron sulfate (II) byproduct, leaving only the titanium salt which is again processed to obtain the final titanium dioxide product (in the form of a white powder).

As it was mentioned in the previous section, TiO_2 in its macroscopic form is commercially employed in several applications, to give some examples, this material can be used as paint pigment, sunblock and even as an anti-corrosive coating for building structures [2]. All of this is possible given the exceptional physical and chemical properties this compound exhibits, some of which are: Null toxicity, biocompatibility, corrosion resistance and UV radiation absorption; this goes without mentioning that TiO_2 is an inorganic material which does not impose a detriment to the environment. Due to all these facts, ever since the 1970s, materials science has kept its gaze directed at the study of TiO_2 from different perspectives in order to

determine if this compound can be employed in alternative disciplines of science and industry additional to the previously mentioned ones.

An initial and significant study concerning the development in TiO₂ research was reported in the year 1972, by the groups of Fujishima and Honda in Japan [3], this work reports for the first time the use of a TiO₂ electrode to achieve water photolysis¹ (such process had not yet been accomplished by any other method) and as a consequence, research studies regarding the catalyst properties that TiO₂ exhibits were vastly considered among the scientific community.

Although the previous study corresponds to the chemical sciences, titanium dioxide has also been applied in the physics line of research, namely in 1968 when the group of Gerischer and Tribusch [4] in Germany explored and published the use of organic compounds for the sensitization of crystals made of inorganic oxides like zinc oxide (ZnO) in order to obtain measurable photocurrents; these results represented a milestone among the physics community because it established one of the first steps in the photovoltaic devices research and it is important because titanium dioxide is one of the most commonly used inorganic crystals in this sort of devices. Consequently, around the year 1980, the laboratory of M.P. Edwards and J.B. Goodenough et al. [5], performed in the United Kingdom the first experiments in TiO₂ photosensitization using ruthenium based dyes. Later, in the year 1991, the group of Grätzel and O'Reagan [6] in Switzerland used all these previous research to develop and report the fabrication of a fully functional, dye-sensitized solar cell based on a TiO₂ thin film, reporting energy conversion efficiencies comparable to commercial solar cells. In this regard, ever since the last decade of the twentieth century, the number of publications concerning TiO₂ has increased drastically in several scientific journals due to the numerous research possibilities this material offers [7].

Given the global emergence of new and more accessible technologies for materials characterization, the research groups which occupy themselves with titanium dioxide investigation were able to leave aside the macroscopic properties of this compound, in order

¹ Chemical process by which a water molecule splits into hydrogen and oxygen due to the interaction with UV light [99].

to take the leap towards the study of its properties at microscopic and even nanometric scales. The Electron Microscopy technique has been an important tool to propel the discovery of nanostructures present in TiO₂ thin films fabricated by different method, this is why until the year 2016 there have been scientific reports of nanotube [8], nanorod [9], nanoflower [10] and nanosphere-like [11] structures; aside the evident morphological difference among said structures, titanium dioxide formations behave differently as well; for example, whilst nanosphere-like formations exhibit generally the Rutile crystalline phase in its structure [11], nanotubes majorly present the metastable Anatase phase [8], causing at the same time different types of behaviors in optical properties such as the gap energy and the absorption coefficient.

The beginning of the new millennium, brought with it another significant step forward in the study of TiO₂ thin films, specifically in the year 2001, when the group of Asahi, et al. [12] reported for the first time the successful modification of the gap energy in titanium dioxide by doping its structure using nitrogen atoms. To justify this physical phenomenon, the researchers associated the change in gap energy to an increment of the valence band in the semiconductor given the interactions between the implanted p states of nitrogen with the *O2P* states of the matrix. The main reason to perform doping with electronically active agents into the TiO₂ lattice is to obtain a decrease in its gap in order to make the material sensitive to an even wider range of the solar spectrum, in other words, a titanium dioxide sample typically presents gap energies of around 3.2 eV, which implies that it absorbs light only from the UV region, this means that just 7% of the solar spectrum is absorbed by the compound; by doping a TiO₂ matrix with another appropriate element, the range of absorption in the entirety of the material can be broadened, making its application in solar cells even more practical due to the fact that it can capture a greater amount of energy from the Sun [13].

Numerous recent reports can be found regarding the doping of titanium dioxide with several elements; the majority of the transition metals from the 3d block, such as: Titanium [14], Vanadium [15], Chromium [16], Manganese [17], Iron [18], Cobalt [19], Nickel [20] and Copper [21] and elements from the 4d block, like: Niobium [16], Molybdenum [22], Ruthenium [23], Rhodium [24], Palladium [25], and Silver [26] as well as all the alkaline elements: Lithium [27], Sodium [28], Potassium [29] and Cesium [30] and also Aluminum [31] have been used in TiO₂ doping (the most relevant elements from the 5d block have also been studied, namely Iridium

[32], Platinum [33] and Gold [34]). A review on the different properties which titanium dioxide presents as some of these elements are added to its matrix is presented in the following section.

The element used as dopant in this thesis is Cobalt (Co), which is a metallic, ferromagnetic and gray-silver colored material; its melting point is relatively elevated (1768 K) and its electric conductivity is four times lower than that of copper ($17.2 \times 10^6\text{ S/m}$), section 1.7 contains some additional properties regarding this transition element. The interest in fabricating TiO₂:Co lays on the fact that, as mentioned before, these thin films are conductive, ferromagnetic and optically transparent at ambient temperature [35], such properties make it a possible candidate for spintronic applications [36], photocatalysis [37] and photovoltaic devices [10]. Shao, et al. [19] were one of the first research groups that explored the addition of cobalt to the TiO₂ lattice even before the year 2000, however in this case not only cobalt doping was studied, but cobalt oxide (CoO) as well, and this was done in order to understand the chemical interactions and changes in dispersion from photoemission spectra.

From that point forward, a great variety of reports on TiO₂:Co can be found in the literature, delivering relevant results for the progress of materials science. As an example, in the year 2004, a study carried out by Geng and Kim [38] concerning the theoretical aspects of TiO₂:Co was reported, in that work they investigated the inclusion processes of cobalt into the titanium dioxide lattice using the Density Functional Theory (DFT), finding that the most stable type of diffusion in the solid solution was substitutional; another important result consisted of an explanation of the measured fluctuations in magnetization which TiO₂:Co presented in the laboratory. In 2006, Huang, et al. [39] published a study on the structural and optical properties of Ti_{1-x}Co_xO₂ thin films prepared by the sol-gel method coupled with spin-coating, in it they found that these films exhibited ferromagnetism at ambient temperature, which is a consequence of the vacancies left by the oxygen atoms ejected from the lattice, which at the same time were ejected due to the substitution of the Ti atoms for the Co atoms in the crystalline lattice. More recent studies (2014) emphasize in the morphological characterization of TiO₂:Co alloys prepared by the modified sol-gel method, finding nanoflower structures in its surface [40]. However, it is not enough to maintain these investigations at a laboratory level, on the contrary, the capabilities of the material must be expanded towards different grounds and applications in devices and new technology; in this

regard, an application of this compound was reported in the year 2015 by Kim and Choi [41], who in their work describe the fabrication of copper doped TiO₂ nanotube thin films with the purpose of improving the electrochemical performance of Li-ion batteries²; as a result, they found an improvement of 23.6% in the reversible capacity and 35.5% in the discharge capacity (after 300 cycles) of the battery when the copper-coated titanium anode was used instead of the pure titanium.

In this manner, considering all the previous studies as a fundamental background, it was the main objective of this thesis to fabricate TiO₂:Co thin films using the DC Magnetron Co-Sputtering technique varying the amounts of cobalt in the TiO₂ matrix in order to perform structural, morphological and optical studies on the material, and in this way investigate the influence of the synthesis parameters in the physical properties that the films exhibit. This analysis allowed us to establish the potential applications of the compound in research areas like spintronics or photovoltaic devices.

1.2 Properties of impurity-doped TiO₂.

Following the same thread from the previous section, the following lines aim to expose some of the most interesting and relevant studies regarding the research of titanium dioxide as a semiconductor host for different types of impurities, extending the reach of this compound in material science and engineering.

Recalling the work from Dake and Lad [31], their research focused on the existing interaction at the interface of a monocrystalline (110) layer of TiO₂ with aluminum (Al) impurities. The sample preparation was realized by cutting a single crystal TiO₂ boule, into a parallelepiped bulk, and then polishing mechanically the surface to enhance the surface uniformity and simplify the stoichiometric obtaining process; additional annealing processes, along with inert gas bombardment was carried out in high vacuum, which further reduced the sample bulk. The addition of aluminum was made using the physical evaporation method, employing a tungsten heater and a 99.99% pure aluminum wire, and in order to examine the interactions at the interface, XPS, UPS and Auger spectra were measured, along with LEED measurements. Some of the most interesting results obtained by this group yielded the interaction of Al with both

² These batteries often use anodes made exclusively of titanium.

stoichiometric and oxygen-deficient titanium dioxide at room temperature, highlighting the difference between depositing a monolayer of Al in the surface and depositing a multilayer; the first of these configurations causes a reduction of the TiO₂, which in turn oxidizes the aluminum monolayer, creating an alumina extra-layer; for the second regime (higher doses of aluminum), a heterogeneous overlayer is formed consisting in both metallic and oxidized aluminum. The main reason for this difference lies on the fact that, according to the electric interactions, the charge transfer in the Al monolayer occurs from the aluminum to the superficial cations of Ti, thereby reducing it, a fact which does not take place in the higher dose configuration. In addition to this, the research also wonders the possibility of the formation of an intermetallic phase of Ti₃Al, which would represent a significant change in electronic and chemical properties at the interface, however their experiments did not find any evidence of the formation of this phase, which is most likely associated to its proper thermodynamic instability.

Crisan, et al [42] worked on the addition of iron (Fe) to a titanium dioxide matrix, via the commonly used sol-gel method, in this case, their goal was to evaluate the variation in performance of TiO₂ nanopowder as a photocatalytic once iron was added to its structure. To that objective they performed standard X-Ray, TEM, XPS and magnetic measurements for the structural characterization, and also photocatalytic performance tests to determine the change in material properties. As a result, they found that the addition of iron in a weight percentage of 0.5% to the TiO₂ xerogel exhibited the best photocatalytic activity in the degradation process of nitrobenzene from water, a fact that points towards an important application regarding the de-contamination of wastewaters from a great variety of toxic and refractory pollutants such as nitrophenols and nitrotoluenes. Physical effects, such as lattice distortion, crystalline phase acceptance and change in magnetic behavior (from diamagnetic in pure TiO₂ to paramagnetic in doped TiO₂) directly incur in the performance of this doped semiconductor as a photocatalytic material.

Further bibliographic investigation granted an interesting study regarding the adsorption process of lithium (Li) on the surface of polycrystalline Titania; a phenomenon that was studied by Ageev and Solovev [27] in 2001. Using the electron-stimulated desorption technique, they were able to determine the desorption of Lithium atoms from a TiO₂ surface previously deposited over a tungsten sample, the purpose of the study was to determine the

variation of the desorption process compared with the desorption of alkali metals over tungsten oxide surfaces given the fact that alkali metals are commonly used as catalytic promoters on oxide supports. The TiO_2 grown over the tungsten substrate was deposited by evaporating a titanium rod and the submitting the resulting material to oxidation in a reactive atmosphere; the Lithium was then deposited again using the thermal evaporation technique, this time using as precursor the mixture of Li_2CO_3 and CaO , and then reducing it with an aluminum powder at 700 K .

As a result, they found that the elevated kinetic energies measured for the electron-stimulated desorption (ESD) of lithium over titanium compared to lithium over tungsten oxide suggested a stronger bonding energy between Li and TiO_2 , also the annealing processes between 1200 and 1700 K which the samples were subject to, showed a strong irreversible surface reconstruction in the freshly deposited TiO_2 layers [27]. The determination of desorption of lithium atoms and oxygen atoms was calculated using the ESD yield as a ratio between the ion current (whether it be lithium or oxygen ions) desorbing from the TiO_2 surface and the bombarding electron current, both measured with an electrometer.

1.3 Fabrication reports of the $\text{TiO}_2\text{:Co}$ compound

Having explored several studies regarding the doping of TiO_2 thin films with different metals, we will now focus solely on the preparation of alloys similar to the ones present in this work, namely, titanium dioxide with cobalt as an additive. To that end, a bibliographic scrutiny is necessary in order to have a greater understanding on some of the deposition techniques and relevant results found by different research groups.

For instance, it was remarked in section 1.1 a review of the work made by Huang, et al. [39] where they synthesized $\text{TiO}_2\text{:Co}$ thin films through the sol-gel method coupled with spin-coating; a further evaluation of this work shows that the employed substrates in the deposition were silicon wafers with preferential orientation (111); fabrication of the films originated from an aqueous mix of tetrabutyltitanate ($[\text{Ti}(\text{OC}_4\text{H}_9)]_4$) and ethanol, with the addition of deionized water and acetyl acetone for hydrolysis and polycondensation, obtaining as a result the titanium dioxide Sol. The cobalt precursor added to the mixture was the compound $\text{Co}(\text{NO}_3)_2 \cdot 6\text{H}_2\text{O}$ varying the metallic ion concentration between $x = 0$ and $x = 0.07$, with x being

the atomic percentage of said ion. The obtained sol was left 48 hours for aging before being submitted to spin coating at *2000 rpm* 1 minute to achieve a better covering of the substrate. The resulting compound has therefore the chemical formula Ti_{1-x}Co_xO₂ where *x* varies between *0.0* and *0.7*; the samples were structurally and optically characterized using X-Ray diffraction and photoluminescence technique, in addition a relevant study on the magnetic properties of the material was done. The most relevant result the work presents, concerns the ferromagnetic nature of the compound as the metallic ion is added to the TiO₂ matrix, the substitution of Co causes a disorder in the lattice and as a consequence, O₂ vacancies occur, which at the same time are responsible for the ferromagnetic behavior of the material.

Another synthesis method of this compound was developed and reported by the group of Bouaine and Schmerber, et al. in 2012 [43]. In this case, a TiO₂:Co powder was prepared, instead of a thin film. The concentration of cobalt varied between *0.0* and *0.5 at.%*; the final product differs from a thin film disposition due to the fact that in this case, the solid state reaction method was used. Experimentally, the investigation consisted in continually mixing TiO₂ powder in anatase phase with CoCo₃·H₂O powder for subsequent sintering at *1000 °C* for 10 hours in an air atmosphere. After this process, the mixture was grinded in an agate mortar to avoid magnetic contamination, selecting only a few samples for post-synthesis annealing at *450 °C* for 10 hours in an N₂/H₂ atmosphere with the goal of creating O₂ vacancies in the lattice. After various structural, morphological, optical and magnetic studies, they found that the TiO₂:Co samples crystallized in the Rutile phase, and due to the cobalt doping, the gap energy decreased in comparison with that of pure TiO₂. Additionally, the measurements of magnetization resulted in a paramagnetic behavior for the powder without any posterior treatment, whilst the annealed samples exhibited the ferromagnetic property.

A mainly physical method of fabrication is the Pulsed Laser Deposition (PLD); Rou, et al. [44] reported in the year 2013 the use of this technique to obtain TiO₂:Co thin films. To correctly apply this type of experiments, they used a krypton fluoride (KrF) laser of wavelength $\lambda = 248$ nm, which implies that the incident light from the device is not visible and highly energetic; by making the radiation interact with a ceramic TiO₂ target (rutile titanium dioxide mixed with *1 mol%* of Co₃O₄), several particles are ejected from it and are deposited on a substrate made of Alumina (Al₂O₃). Because the light must be carefully propelled towards the target, the researchers must use a determined frequency at a definite time, in this case, the work reports

a *30 ns* pulse duration, coupled with a repetition rate of *20 Hz*. Another fundamental aspect of this technique is the atmosphere in which the experiment is carried out (this is because the oxygen in the ambient atmosphere can cause unwanted reactions in both the target and the substrate), typically, an inert argon atmosphere is employed³. Substrate temperature also plays an important role in PLD to activate the free bonds in its surface; additional aspects like the incident angle of the light and target-substrate distance are also relevant. The main result in this work corresponds to the reduction of the energy gap determined by optical measurements as cobalt is introduced into the TiO₂, this directly implies the usage of the compound in the photovoltaics area of investigation, and is therefore relevant to our study.

Finally, an additional method of fabrication reported for the synthesis of the nanostructured compound was developed by Savio, Fletcher and Hernandez [45] and consists on the sonication of a titanium isopropoxide (Ti[OCH(CH₃)₂]₄) aqueous solution mixed with the additive element. Specifically, they added *30 mL* of deionized water drop by drop into *150 mL* of isopropoxide to later add the different dopants for sonication, namely they used aluminum (Al), carbon (C), cobalt (Co), iron (Fe) and rhodium (Rh); the resulting colloids were put in a heating plate at *60 °C* for 24 hours. As a result, they obtained TiO₂ powder doped with the mentioned elements which they later submitted to thermal processes in order to crystallize the amorphous TiO₂ obtained with this technique. The main objective of this work was to evaluate the variation on the band gap energy of TiO₂ in different crystalline forms as the distinct additives were added to its matrix, as a conclusion they observed that the band gap in all treated samples from temperatures ranging from *100 °C* to *600 °C* remains relatively constant at *3.2 eV*, except when iron was used as the metallic dopant, in turn, they associated this effect of band gap tuning to the presence of bi/tri-crystal formations of anatase, brookite and rutile. Additional analysis showed the forming of a network of quantum dots in the aqueous precipitates with sizes between *5* and *10 nm*.

Understanding this additional background imposes a further acknowledgement of the various synthesis techniques employed in the obtaining of TiO₂:Co alloys, and is therefore important to study these results to correctly interpret the ones presented in the following chapters. In this manner, the preparation of the TiO₂:Co thin films was carried out using the DC Magnetron

³ This requires the usage of a vacuum chamber operating at 7 to 70 Pa.

Co-Sputtering technique, which offers several advantages relative to some of the methods explained previously, and constitutes an advancement in the materials science line of research of the Physics Department and the Science Faculty.

1.4 Structural properties of materials

Material science often focuses in the research of the crystalline structure of materials, and it can do so by applying experimental and theoretical techniques of characterization. The goal of said research is to determine the crystalline lattice inside a material, along with the most probable position of the atoms inside of it in order to correlate these properties with further characteristics of the material under study; further development of material science lies on the discovery of new, never previously observed crystalline structures in new materials fabricated with diverse methods, it is therefore almost an unduly requisite for this work to present and analyze the structural properties of the fabricated material, namely TiO₂:Co thin films.

Although there is a handful of structural characterization techniques, researchers often begin their respective analysis with one particular technique, which is also the first study that will be presented in Chapter 3, and it refers to the X-Ray diffraction technique. Although the experimental aspects of such a technique will be handled with detail in the next chapters, this section in particular addresses the theoretical use and principles of this technique. Given that understanding the type of crystal structure, possible crystalline phases present, lattice parameters, crystallite size, etc., is a crucial part of the structural characterization, a theoretical method was developed for refining a given diffraction pattern based on the experimentally acquired data [46], and it is remarkably useful for the determination of the previously mentioned characteristics in a material. The following discussion will focus exclusively in this method, given its importance for this work.

In a broad sense, the profile refinement method is used to “refine” the crystal structure model of a material, which means that it uses theoretical tools to model an experimental diffraction pattern (obtained with an X-Ray diffractometer), and then apply the least square method to determine the best possible fit for said pattern. In doing so, several parameters have to be adjusted in order to establish the adequate fit, and as a conclusion, the crystal structure, atomic positions, unit cell parameters, crystallite size, microstrain, residual strain, and most

important of all, the crystalline phases present inside the material can be determined or inferred, giving this technique the property of being not only a structural characterization technique, but also a compositional characterization technique.

The diffraction pattern for each material is unique and works as a fingerprint for researchers, who can identify the chemical compounds inside a powder sample or thin film sample, given only the requisite for the sample to be crystalline, by which it means, for it to have a periodical arrange of atoms at a large scale, a material can have either one unique crystalline phase on its structure or several, which implies that crystalline materials can basically be sorted into two major groups: Monocrystalline and Polycrystalline samples; a monocrystal characterizes itself because only one diffraction peak will be observed through-out the entire range of possible diffraction angles, whereas a polycrystal exhibits several diffraction peaks, which indicates the presence of more than one crystalline phase⁴, this can happen when two or more compounds are used as precursors for the obtaining of a new material, and also on natural minerals found on the crust of the earth. Materials that are not crystalline, often named amorphous, do not have a periodical arrange of atoms and do not exhibit any diffraction peaks and therefore the profile refinement method becomes useless for its original purposes.

The fabrication or natural origin of a material can have several effects on its crystalline structure, two materials can be chemically identical and yet have different diffraction patterns, a clarifying example of this fact is graphite and diamond, both are essentially bonded carbon atoms, but the crystalline structure is completely different, and therefore the diffraction pattern will also be different. This is also the case with TiO_2 , as it was mentioned before, this material can exhibit a rutile, anatase or brookite crystalline structure, the three of which have an identical chemical formula, but their diffraction pattern will differ greatly on the position of the diffraction peaks.

Suppose a diffraction pattern from a polycrystalline sample, such as the one present in **Fig. 1-1** (this curve is from one of the substrates used in the present work). In this diffractogram, there are several diffraction peaks or angles for which a constructive interference condition for the reflected radiation is fulfilled, which can be said to be equivalent to fulfilling the Bragg

⁴ This fact will be clarified in Section 2.2.1.

diffraction condition (eq. (2.1)). Given that several crystalline phases may be present in this sample; the profile refinement method can give aid to identify the structural properties of the material at an initial stage.

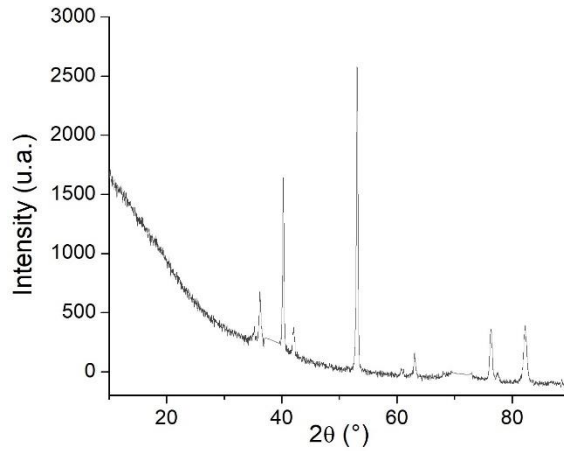


Fig. 1-1: Diffraction pattern of a polycrystalline titanium foil sample. Results are generally presented as Intensity vs. 2theta (2θ).

For real diffraction data, the intensity Y_{ic} of each individual data point i is calculated using the following equation:

$$Y_{ic} = Y_{ib} + \sum_{k=k1}^{k2} G_{ik} I_k \quad (1.1)$$

Where Y_{ib} is the intensity of the background radiation at a point i in the pattern, $k1$ and $k2$ are the reflections contributing to the data point i in the pattern given that sometimes multiple Bragg diffraction peaks overlap, and this results in multiple contributions to the observed intensity at a single data point. G_{ik} corresponds to the peak profile function which describes how the intensity of the diffraction peak is distributed over a range of 2θ rather than at a single point (this profile is due to instrument broadening, sample broadening and other factors.), and I_k is the theoretical intensity of the Bragg diffraction peak k , which is empirically fit with a series of equations, consisting of several functions designed to better adjust the shape of a diffraction peak.

This intensity can be modulated by varying its different parameters in order to correctly fit the observed peak of the diffraction pattern. The diffraction peak intensity is spread out over a range of 2θ , the total area of the diffraction peak profile is the predicted intensity I_k . Although the refinement method adequately predicts a given intensity of a given diffraction peak, it is important to also mention that these peaks can also change in shape from the instrument contributions, which grant a characteristic broadening and shape to the diffraction peak based on their own unique optics and geometry, this means that every separate combination of components such as slit apertures, Soller slits, beta filters, monochromators or detectors will have their own contribution to the shape of the peak.

The refinement, as it was mentioned above, is carried out by minimizing the conventional residue function using the least square method. The mentioned function is cited in eq. (1.2).

$$R = \sum_j w_j |Y_{j(o)} - Y_{j(c)}|^2 \quad (1.2)$$

Where $Y_{j(o)}$ and $Y_{j(c)}$ are the observed and calculated intensities, respectively, in the j -th step of 2θ and w_j is the weight or pondering value for each intensity, whether it be observed or calculated. This method is remarkably accurate in the quantitative analysis of diffraction patterns than any other method based on peak intensity analysis [47].

Knowing the structural properties of the material, such as the unit cell lattice parameter, atom positions, spatial group, peak positions, peak shifting, etc., leads to the determination of the crystal structure of the material and its composition by comparing the calculated diffraction pattern with a universal data base of crystallography that contains the majority of the diffractograms of every possible element or compound ever discovered by other research groups, the most renown database is the Powder Diffraction File (PDF) which contains over 300 000 diffraction patterns, all of which have a PDF card assigned that shows useful information regarding that specific crystal structure, including the lattice parameters, type of crystal system (or Bravais lattice), and even literature references.

In addition to the previously mentioned applications, the profile refinement of a sample serves as a support for further calculations that come from the variation in peak shape of a given

diffraction peak. Such variations are properly consistent with the peak broadening in a sample, which is mainly due to three different phenomena: Crystallite size, microstrain and instrumental broadening of the peaks. The latter can be corrected with a calibration curve of the diffractometer using a reference sample such as LaB₆, and the other two contributions can be determined using a Williamson-Hall [48] plot which uses the full width at half maximum (FWHM), the lattice strains from displacements of the unit cells about their normal positions and other factors in order to quantify these physical phenomena and gain more insight into the behavior of the material.

The crystallite size L is often calculated using the Scherrer formula [48], which is cited in eq. (1.3). This relation depends on the position of the diffraction peak to be evaluated ($\cos \theta$), the FWHM ($B(2\theta)$), the wavelength of the incident radiation (λ), and a parameter K which is a constant of proportionality (also called the Scherrer constant) that depends on the shape of the crystal and the size distribution; as a general case, the value of this constant is taken as 0.94.

$$B(2\theta) = \frac{K\lambda}{L \cos\theta} \quad (1.3)$$

The total microstrain of the sample is calculated using eq. (1.4):

$$B(2\theta) = 4\varepsilon \frac{\sin \theta}{\cos \theta} \quad (1.4)$$

Where $B(2\theta)$ once again is the FWHM, and ε is the strain factor for the crystal plane separation that varies as:

$$\varepsilon = \frac{\Delta d}{d} (\%) \quad (1.5)$$

The microstrain produced from the mentioned displacements inside the unit cells are produced by dislocations, domain boundaries, grain surface relaxation and other contributions. By analyzing the diffraction pattern of a sample, it is possible to determine whether the broadening of the peaks is mainly due to the crystallite size or to the microstress.

A useful way to make said analysis comes from the Williamson-Hall plot, which gathers both contributions as shown in eq. (1.6).

$$B(2\theta) = \frac{K\lambda}{L \cos \theta} + 4\varepsilon \frac{\sin \theta}{\cos \theta} \quad (1.6)$$

Rearranging the previous equation yields:

$$(B(2\theta) \cdot \cos \theta) = \frac{K\lambda}{L} + (4\varepsilon \cdot \sin \theta) \quad (1.7)$$

In this manner, it is possible to obtain a linear fit for the FWHM as a function of the diffraction angle and ultimately determine that the intercept of this line with the vertical axis is directly related to the crystallite size L and its slope is related to the microstrain ε , this analysis is often referred to as a Williamson-Hall plot. Conclusively, both contributions can then be evaluated and further treatment of the data can establish whether it is accurate to assume that both contributions are present on the sample, or if only one of them is responsible for the peak broadening.

The structural characterization of a sample can give a basic idea that a certain experiment is producing the expected results or not; this fact can be used in order to alter or maintain the course of action in a research work and make decisions regarding the possible applications of the material. A contribution to materials science is evident once a material fabricated by a new experimental technique is structurally characterized and compared with the reports from other research academies, as is the case with this work.

1.5 Morphological and topographical properties of materials

The surface study of a material is fundamental in its characterization process; for that purpose, in the material science discipline there exists several microscopy techniques to observe and analyze the topography and morphology of a sample, and then correlate its characteristics with the deposition or fabrication method. For this work in particular, two major techniques employed in the characterization of the TiO₂:Co thin films were the Scanning Electron

Microscopy (SEM) and the Atomic Force Microscopy (AFM), which will be discussed in the following chapter. Both of these techniques are useful to determine the morphological and topographical properties of the thin films, and the following lines will focus on some of the available physical parameters to be measured from SEM and AFM micrographs.

SEM microscopy works under the principle proposed by De Broglie, by which an electron in motion has a characteristic associated wavelength depending on its momentum and Planck's constant. Based on this fact, it can be concluded that the use of a SEM to study the surface of a sample represents an enhancement of 3 orders of magnitude in optical resolution⁵ compared with a standard optical microscope, implying a tremendous advantage for this technique in material science research. A SEM micrograph represents an intensity map of the scanned region in the surface of the sample, which is visualized as a grey-scale image where the darkest zones indicate a greater depth than the bright ones. **Fig. 1-2** shows a typical SEM micrograph for a sample of potato starch [49].

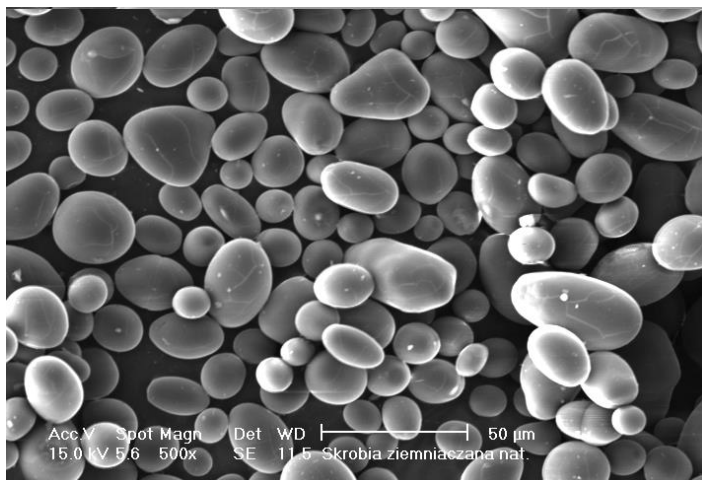


Fig. 1-2: SEM micrograph of potato starch particles [49].

Evidently, the surface morphology of the sample showed in **Fig. 1-2** is of granular nature, and although the morphology of a sample can vary greatly depending on the deposited material, fabrication parameters, employed substrate, chemical precursors, etc.; the micrograph presented was chosen as an example because it exhibits clean boundaries between structures over its surface, and the use of specialized software can aid in the determination of the average

⁵ This conclusion will be clarified in Section 2.2.2

grain size of the material given the scale localized at the bottom of the micrograph itself. With this information, it could also be determined whether the grain sizes follow a defined statistical distribution that gives an idea of any possible dependence of the grain growth with regards to any of the fabrication parameters. In addition, the crystallite size of the samples can be compared to the grain size in order to corroborate any calculations made via the Scherrer equation (eq. (1.3)). However, recalling one of the previous ideas, not every sample has a granular structure with clear, defined boundaries over its surface, in general there are several types of structures that have been discovered by material science research groups, which include: Flower-like, rod-like, tubular, spherical, porous, ring-like, platelet-like, sheet-like micro and nanostructures, among others. All of which can be studied with the SEM microscope and further analyzed with specialized software in order to determine lengths, sizes, diameters, and even the proper thickness of a thin film, which is an important parameter for advanced studies, such as the optical characterization of a material.

On the other hand, the atomic force microscope (AFM) offers a different spectrum of parameters to be calculated from its measurements. Starting with the physical principle of operation (which will be addressed in a posterior section), this technique differs in the type of information the user can extract and analyze, whilst still being a morphological and topographical characterization technique. An AFM micrograph consists on a two dimensional profile of a certain specific region in a sample (although it can also be three dimensional) typically a few squared nanometers in size, in which the user can observe the various peaks and valleys, and overall topography of said region. This technique offers a greater resolution than a SEM equipment (depending on the specifications) and can work with conductive, semiconductor or insulator materials, whereas a SEM microscope has to be uniquely applied on conductor surfaces.

When measuring a sample under an AFM, it is important to first optimize the quality of the image, which is done using specialized software for AFM analysis [50], designed to enhance the visualization of the different features a micrograph may hold. Often images may reveal distortions caused by either by tilt samples or non-linear scanner behavior [50], in this manner, with the goal of optimizing the image, processes such as image leveling and noise filtering are in order with every obtained micrograph. The most common tool used in this regard are the line by line leveling, matrix filtering and Fourier filtering; these last two features

are used to eliminate noise from an AFM image caused by irregularities in the surface roughness, sample impurities, humidity, mechanical instabilities and electronic instabilities.

Once a micrograph is duly optimized and freed from distortions, a quantitative description of the surface topography is then necessary in order to infer the physical properties of the fabricated material. To that end, several parameters have been implemented to evaluate the surface profile, the most common of which are consistent with the amplitude or height parameters, which in turn are also the principal characterization objective in an AFM study. Among said parameters, the average sample roughness (R_a) and the root mean square sample roughness (R_q) are the most used amplitude coefficients; the latter is described mathematically by eq. (1.8) and it gives the overall deviation in height of the micrograph, and depending in the objective of the study it can be calculated for a two dimensional (2D) or three dimensional (3D) profile, eq. (1.8) shows the case when a 3D profile is in order.

$$R_a(N, M) = \frac{1}{NM} \sum_{x=1}^N \sum_{y=1}^M (z(x, y) - \bar{z}(N, M)) \quad (1.8)$$

The root mean square (RMS) roughness of a sample is mathematically cited in eq. (1.9) and its formula is quite similar to a standard deviation calculation, which is exactly what this parameter yields for the heights in a sample relative to a mean line. This height parameter is used to study temporal changes in the creation of a new surface as well as spatial differences when the features of a surface are being studied using different scales [50], the reason for this lies on the fact that RMS roughness is more sensitive to large deviations with respect to the mean line and much like the previous roughness, it can also be calculated for a 2D profile and a 3D profile, eq. (1.9) references once again the case for a 3D profile.

$$R_q(N, M) = \sqrt{\frac{1}{NM} \sum_{x=1}^N \sum_{y=1}^M (z(x, y) - \bar{z}(N, M))^2} \quad (1.9)$$

Both of the previously mentioned height parameters are obtained, as it was mentioned above, via a specialized image processing software, and they both grant information regarding a very

important physical property, which is the roughness of a sample at a nanometric scale. With that information, any possible applications for the material are then susceptible for determination and further progress may be done in the research for a potential new material.

1.6 Optical properties of materials

Additional characterization of materials usually concerns other physical responses in order to evaluate their potential applications. It is of particular interest for this work the determination of the optical response in the thin films when electromagnetic radiation is directed towards their surface; the main idea consists in illuminating a sample with monochromatic radiation all through a wide range⁶ of the electromagnetic spectra and then collecting the transmitted, reflected or absorbed intensity. To that end, a commonly used equipment employed is a UV-Vis-NIR spectrophotometer, which is a device designed to measure the transmitted, reflected and even absorbed intensity of an optical medium relative to the total incident intensity, its basic principles of operation are further discussed in the next chapter.

As light interacts with a specific surface, three physical phenomena can occur, namely: Transmission, reflection and propagation [51], the conditions for either one of these processes to take place, depend on the surface composition and thickness. Once a light beam of certain wavelength starts propagating through a medium, different processes can occur as well, such as: *Refraction*, which causes the light waves to propagate with a smaller velocity than in free space, *Absorption*, which occurs if the frequency of the incident radiation is resonant with the transition frequencies of the atoms in the medium, *Luminescence*, which is a name given to the spontaneous emission of light by excited atoms inside a solid state material, and *Scattering*, which is the phenomenon where light changes its direction and quite likely its frequency after interaction with the medium in addition. If a light beam has enough intensity to reach the back side of an optical medium, it can then be reflected or transmitted, meaning that the amount of transmitted radiation can clearly be related to both absorption and reflection at the front and back surfaces of a sample or material.

Quantification of the previously mentioned physical phenomena can be made through the use of three optical parameters, namely: Spectral transmittance (T), spectral reflectance (R) and

⁶ A typically used range includes the ultraviolet, visible and near infrared region.

absorbance (A). The first two wavelength-dependent relations are defined mathematically in terms of power ratios between transmitted and reflected powers, relative to the total incident power, respectively; the absorbance of a medium, also called the Optical density (O.D.) is defined as eq. (1.10) describes.

$$O.D. = -\log_{10} \left(\frac{I(l)}{I_0} \right) \quad (1.10)$$

Where $I(l)$ is the intensity at the total length l of the medium and I_0 is the intensity at the surface of the medium. By the physical principle of the conservation of energy, transmittance, reflectance and absorbance must fulfill the principle described in eq. (1.11).

$$T + R + A = 1 \quad (1.11)$$

The absorbance of a medium itself is related to another quantifiable coefficient, called the absorption coefficient (α), which is independent of the length of a sample and is defined as the fraction of the power absorbed in a unit length of a medium [52]. Assuming a beam propagating in direction z through an optical medium, then the decrease in power per unit area (also referred to as Intensity $I(z)$), in an infinitesimal slice of thickness dz will be defined by eq. (1.12).

$$dI = -\alpha dz \times I(z) \quad (1.12)$$

Once this expression is integrated, the result is known as the Beer law (eq. (1.13)).

$$I = I_0 e^{-\alpha z} \quad (1.13)$$

Recalling equation (1.10), it is therefore concluded the dependence of the absorbance on the absorption coefficient (eq. (1.14))

$$A = \frac{\alpha l}{\ln(10)} = 0.434 \alpha l \quad (1.14)$$

Given these elements, it is possible to obtain an overall comprehensive idea of the optical behavior of an optical medium. However, there exist additional theoretical elements to further gain insight into some optical properties of materials, such as the optical band gap and the absorption coefficient.

In 1974, Jan Tauc et al. [53] published a method to determine the optical gap energy of materials based on their absorption coefficient, the incident wavelength and their electric conductivity nature, specifically, for semiconductor compounds (for this specific case, amorphous germanium). Later on, Davis and Mott [54] [55] would expand the reach of this research and covered a greater reach of semiconductors. They showed that the optical absorption strength depends on the difference between the photon energy and the band gap like eq. (1.15) shows.

$$(\alpha h\nu)^{1/n} = A(h\nu - E_g) \quad (1.15)$$

Where h is the Planck constant, ν is the frequency of the incident photon, α is the absorption coefficient, A is a proportionality constant, and E_g is the band gap energy of the material, the factor n depends on the nature of the possible electronic transitions that govern the material, in general it depends on whether a transition is direct or indirect, and allowed or forbidden. For every possible combination of these transitions the value for n is:

- ✓ $n = 1/2$ for direct, allowed transitions.
- ✓ $n = 3/2$ for direct, forbidden transitions.
- ✓ $n = 2$ for indirect, allowed transitions.
- ✓ $n = 3$ for indirect, forbidden transitions.

In the particular case of titanium dioxide, the type of transitions that occur inside the material are consistent with indirect, allowed transitions, implying a value of $n = 2$. In this manner, the basic procedure for a Tauc analysis consists in acquiring the absorbance plot of a given material that spans a range of energies below and above the band gap energy transition, and then by plotting the factor $(\alpha h\nu)^{1/n}$ as a function of the energy ($h\nu$), it is possible to extrapolate a fraction of the curve to the value where $(\alpha h\nu)^{1/n}$ is zero, and as a result obtain the E_g from eq. (1.15) as $E_g = h\nu$.

These are some of the optical properties that were evaluated for the thin films presented in this work. The study of the optical response is relevant not only regarding the possible applications of the material, but also because it enhances and grants insight towards the development of new technologies and new research inside the Group of Nanostructured Materials and their Applications.

1.7 Physical properties of TiO₂ and Co

It has been mentioned previously that cobalt is a metallic, ferromagnetic and grey-silver colored transition metal, which is not produced naturally in the crust of the earth, save for some deposits found in iron alloys from meteorites. Free cobalt is a byproduct of the mining exploitation of elements such as copper and nickel, which are melted so that the element can be extracted; the final product is commercially known as electrolytically refined cobalt. Its crystalline structure is hexagonal (HCP) with an atomic packing factor of 0.74 [56].

Some of the physical properties this element exhibits are summarized in **Table 1-1**.

COBALT	
Symbol	Co
Atomic number	27
Group	9
Period	4
Aspect	Grey-silver
Block	d
Density	8.90 g/cm ³
Atomic mass	58.93 u
Ionic radius	0.63 Å
Atomic radius	125 pm
Covalent radius	126 ± 3 pm
Electronic configuration	[Ar] 3d ⁷ 4s ²
Oxidation states	+2, +3

Oxide	Amphoteric
Crystalline structure	HCP
State (at ambient temperature)	Solid
Melting point	1768 K
Boiling point	3200 K
Enthalpy of fusion	16.06 kJ/mol
Electronegativity	1.88
Molar heat capacity	24.81 J/(mol·K)
Electric conductivity	17.2 x 10 ⁶ S/m
Thermal conductivity	100 W/(m·K)

Table 1-1: Physical properties of cobalt [56].

The cobalt energy band diagram is presented on **Fig. 1-3a**. Given the conducting nature of this element, the band model predicts a superposition of the valence band with the conduction band, implying the inexistence of a gap energy and therefore that the electrons from the valence band may do the transition to the conduction band with a minimum increase in energy.

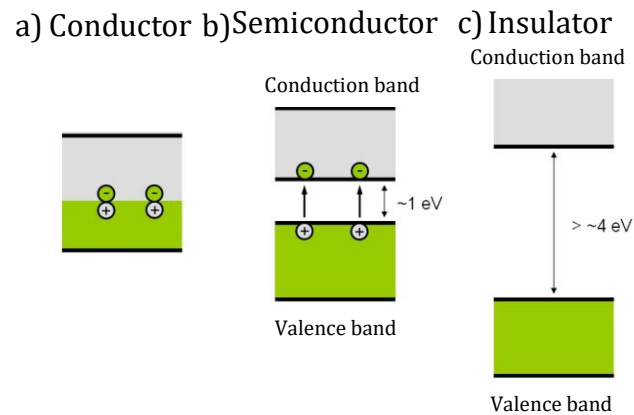


Fig. 1-3: Band diagram for: a) A conducting material, b) a semiconductor material and c) an insulating material [57].

On the other hand, as it was mentioned in previous sections, TiO_2 is an inorganic compound, semiconductor (type n in its bulk form at ambient temperature [58]), naturally occurring in the surface of the earth and white-colored once it has been extracted from the mineral. This material presents different properties that researchers use in order to perform experiments

in photo catalysts, coatings, organic molecules degradation, etc. Some of the characteristic properties of this oxide are summarized in **Table 1-2**.

TITANIUM DIOXIDE			
Molecular formula	TiO ₂		
Density (rutile)	4200 kg/m ³		
Melting point	2103 K		
Boiling point	2773 K		
Crystalline structure	Rutile	Anatase	Brookite
	Tetragonal	Tetragonal	Orthorrombic
Atomic radius	O	0.066 nm (Covalent)	
	Ti	0.146 (metallic)	
Ionic radius	O (-2)	0.14 nm	
	Ti (+4)	0.064 nm	
Hardness (Mohs scale)	5 – 6.5		
Resistivity (rutile)	3 x 10 ⁵ Ω·m (T = 773 K)		
Heat capacity	18255 J/(kg·K) (T = 298.15 K)		
Thermal conductivity (rutile)	6.531 W/(m·K)		
Young modulus (rutile)	273 GPa		
Electronic mobility (rutile)	~ 1 cm ² /V·s		
Hall constant (rutile)	2 x 10 ⁻⁶ m ³ /c		
Gao (rutile)	~ 3 eV		

Table 1-2: Physical properties of titanium dioxide [2].

Due to its semiconductor nature, in the band structure of TiO₂ there is in fact a gap energy between the conduction band and the valence band as **Fig. 1-3b** shows. This implies that for this material, the Fermi level is located between the maximum energy of the valence band and the minimum energy of the conduction band [59]. In order for the energy carries to begin their mobility through the conducting band, an amount of energy equal or superior to the gap energy must be applied to the material, causing the conduction of electric charge inside of it.

2. Experimental aspects

Once the theoretical background for this work has been properly analyzed and interiorized, an evaluation of the experimental scope surrounding this project is in order. In this manner, the following sections will address in depth the entire experimental formalism employed in the fabrication and characterization of the synthesized samples.

Several acknowledgements are in order at this point towards the laboratories that made possible the developing of this section and although not every collaborator can be listed in this document, I would like to extend my gratitude to the entire Physics Department and specially the X-Ray diffraction and Materials Characterization laboratories who allowed me to perform the characterization of the fabricated samples using their robust equipment and provided the pertinent guidance towards a correct analysis of the physical properties of the samples. On the other hand, the laboratory for Fabrication of Nanostructures (Lab. 121C) from the Group of Nanostructured Materials and their Applications, also located in the Yu-Takeuchi building of the Physics department deserves an even greater recognition, because it holds the entire equipment necessary for the sample fabrication and it was the place where I was able to learn, manipulate and apply the knowledge gained throughout the Masters program and point it towards the finalization of this work.

2.1 Fabrication and synthesis parameters of the TiO₂:Co alloys

As it has been mentioned in previous sections, the deposition technique employed in this work is the DC Magnetron Co-Sputtering method for thin film fabrication, this is an enhanced variation of the Thermal Evaporation method [60]. Magnetron Sputtering essentially consists in pulverizing a target⁷ (via ion-bombarding) inside a specific atmosphere in a high vacuum

⁷ Made of the material which will be deposited

chamber, to later redirect the ejected particles towards a determined substrate; the physical principles under which sputtering works are momentum and energy conservation.

Inside the chamber, two electrodes must be placed; one of them is the target to pulverize (negatively polarized cathode), and the other one is the substrate (positively polarized anode). When a high enough voltage is applied between the two electrodes, a glowing electric discharge is produced between them, causing the atoms in the gaseous atmosphere to ionize, forming a highly energetic gas known as plasma. These positively ionized atoms are accelerated towards the target, producing a bombardment in its surface (**Fig. 2-3**); if the ion energy is too low, there will only be energy exchange with the most superficial atoms producing migration effects, however when the ion energy is high enough to reach a threshold value known as “sputtering threshold”, interaction with the surface of the target ejects the neutral atoms in the surface, causing them to become gaseous, these atoms travel towards the substrate, and are condensed there. Two aspects are worth mentioning in this regard, first, the pressure in the chamber must be low enough so that the mean free path of the particles ejected from the target is large enough for them to reach the surface of the target; this is shown graphically in **Fig. 2-1**.

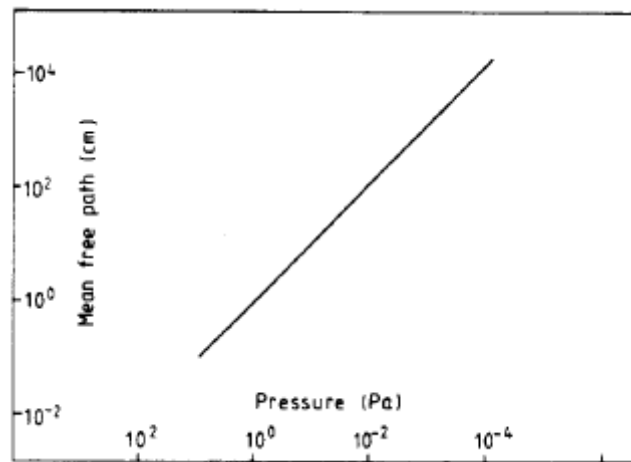


Fig. 2-1: Particle mean free path as a function of the system pressure [61].

The second aspect concerns the sputtering threshold; as **Fig. 2-2** shows, there are specific voltage and current conditions for the glowing discharge to occur, and in general they depend

on the type of gas forming the atmosphere inside the chamber, however it has been determined [61] that the current density between the electrodes must exceed 1 mA/cm^2 .

Ionic bombarding not only pulverizes the target, but also produces the emission of secondary electrons which are simultaneously accelerated towards the plasma. Once in there, the secondary electrons have enough energy to produce new ions through a cascade ionization caused by the impact with the gas atoms, compensating in this manner the loss of charge produced by the collisions of the charged species with the walls of the chamber and the electrodes [18].

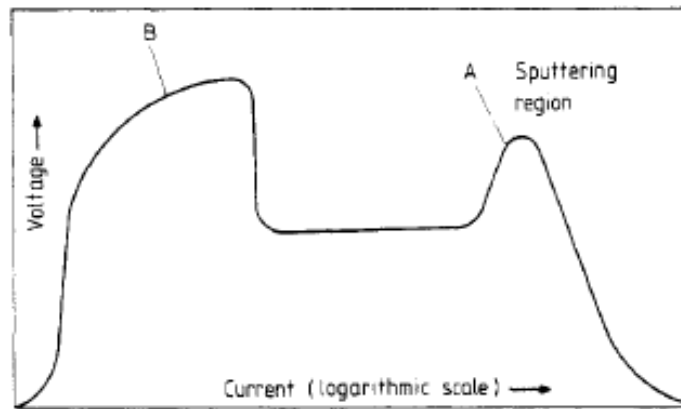


Fig. 2-2: Voltage behavior as a function of the electric current of a gas inside a vacuum chamber. Region A indicates the ideal conditions for sputtering to occur [61].

This process not only takes place over the target, but also on the substrate, and therefore determines the properties of the growing film; 95% of the incident ion energy is lost in the form of heat; the other 5% is transmitted towards the secondary particles. The minimum energy values for the process to occur depends not on the ion mass, so much as it does on the specifications of the target material [62].

Additionally, sputtering is done in the presence of a magnetic field imposed over a DC discharge that increases ion density that attacks the cathode [63]. **Fig. 2-3** shows the schematic diagram of the sputtering operation; plasma is bound to the surface of the cathode by a magnetic field produced by permanent magnets located under the target and an electric field perpendicular to its surface. Secondary electrons are affected by the Lorentz force and travel

in spiral trajectories which further increase the path that these particles undergo and also increase the probability of electrons colliding and ionizing other atoms, which at the same time make it possible for the work pressure to decrease; electrons are confined in an area close to the cathode, mostly ionizing the closest particles to them.

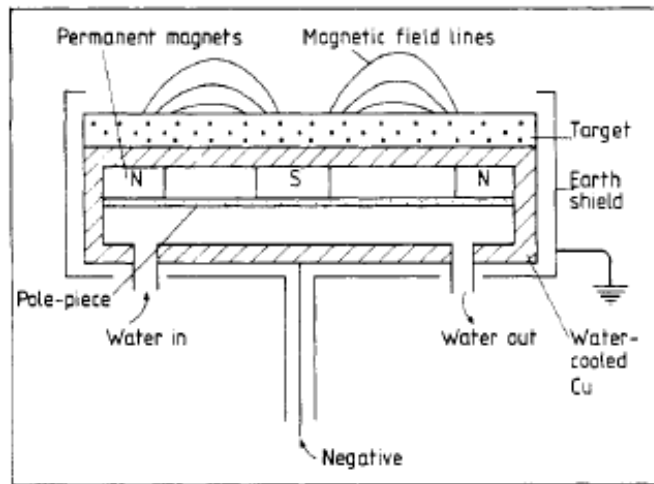


Fig. 2-3: Schematic diagram of the Magnetron Sputtering method [61].

A small disadvantage this method presents is the shape of the field lines, which make it difficult for the target to be uniformly pulverized by the plasma, which reduces the life of the target because not all of the material is used (only 20 to 30% of its total surface is used). However and advantage the method exhibits for its potential application in the fabrication of TiO₂:Co is that it improves the adherence of the particles to the substrate and that it also allows to work in inert atmospheres, such as Argon and Nitrogen.

A variant of this technique, which was used for this work, consists in employing two targets simultaneously to make the deposition. The particles coming from each target are deposited on the substrate at the same time, forming in this manner the required alloy on its surface, this variation is known as DC Magnetron Co-Sputtering and its schematic diagram of operation is presented in **Fig. 2-4**. Basically, after loading the substrates and closing the vacuum chamber, the system is deprived of all the air molecules inside using vacuum pumps until a pressure of around 5×10^{-6} torr is reached, then the entire chamber (but specially the surface of the targets) is cleansed pushing high purity nitrogen for 3 minutes at a rate of 20 sccm inside the chamber. Once this process is done, the system is again brought to lower pressures to extract the

nitrogen, while the heating sources are powered on in order to bring the substrates to the desired deposition temperature. Subsequently, once the substrate temperature is reached, the inert gas⁸ used for ionization can be inserted into the chamber at the same rate used for the nitrogen; once the work pressure is set at 2.5×10^{-2} torr (using a gate between the pumps and the chamber) the magnetrons can then be turned on and each target power can be set, at this point the plasma glowing discharge takes place and sputtering of the targets is effective, however there are also shutters above them blocking the passage of particles from said targets to the substrates so it can be controlled the exact moment at which the deposition may begin. The argon plasma is left to pulverize the targets for three minutes and then the shutters are opened so that deposition may begin. The time of deposition is recorded with a chronometer and then the shutters are closed so that no more particles may be deposited over the substrates, the magnetrons are powered off, and the system is left to cool down at ambient temperatures, or if it were the case the heating sources are further lit to make annealing processes over the samples at low pressures.

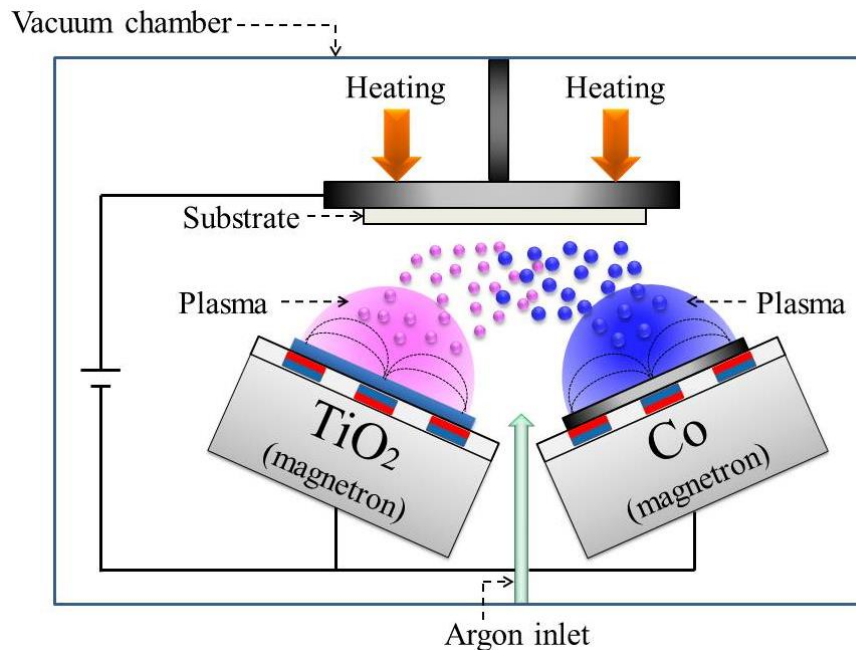


Fig. 2-4: Schematic diagram of the DC Magnetron Co-Sputtering technique.

⁸ In this case, high purity 5N argon

For the extraction of the substrates, the pressure difference between the chamber and the laboratory must be considered, because a sudden opening of it may result in equipment damage or injury, therefore the chamber must be vented with nitrogen until the same pressure of the laboratory is reached, and then the chamber can be opened and the substrates extracted from it. The previously describes procedure must be carefully followed in order to have a successful deposition, paying special attention to the experimental parameters of deposition and subsequent annealing processes, therefore only authorized personnel inside the laboratory may operate the machine, accompanied at all times by another member of the staff.

The equipment located in the laboratory for Fabrication of Nanostructures (Lab. 121C) is a DC-Magnetron Co-Sputtering machine, provided by INTERCOVAMEX, equipped with a stainless steel vacuum chamber, a DC power source, two magnetrons, three gas lines, a pneumatic system to activate shutter valves, six tungsten filaments that act as a heat source for the substrates, an additional DC source to supply the filaments with the necessary current and a refrigeration system to cool down the magnetrons. The three gas lines adapted are used for the injection of: 5N type nitrogen, 5N type argon and pure nitrogen⁹ for the venting of the vacuum chamber. The machine is useful to deposit various types of thin films and can reach temperatures as high as 475 °C and pressures as low as 2.6×10^{-6} torr with the help of mechanic and turbomolecular pumps.

In the year 2005 Han, Wu, et al [64], reported the use of this technique for the synthesis of ferromagnetic TiO₂:Co thin films, however the kind of signal they used is a Radio Frequency signal (RF), in this case the polarization of the electric tension between the electrodes is alternated at typically high frequencies (13.6 MHz), which is advantageous for the deposition of thin films made out of insulating materials, with the aggregated value that purchasing a RF power source capable of reaching the necessary voltages ($>10^{12}$ volts) is more expensive than acquiring a DC source. In the paper published by Han, et al., TiO₂ and Co targets were used in order to fabricate thin films at different substrate¹⁰ temperatures ranging from ambient temperature to 750 °C, the films were later characterized structurally, compositionally and morphologically. Within the synthesis parameters, it is worth mentioning that they employed

⁹ This nitrogen is not entirely pure, because it comes from the plant that supplies all the building with nitrogen, so it carries some impurities with it.

¹⁰ The substrates were made of LaAlO₃

target powers between *50* and *100 Watt* for the TiO_2 target, and between *15* and *100 Watts* for the Cobalt target; the work pressure was *5 mT*. The results obtained indicate that given a *30 W* and *100 W* target power in the Co and TiO_2 targets respectively, the anatase crystalline phase is present on the thin films (using a substrate temperature of *750 °C* and *5 mT* work pressure), however for a different substrate temperature (*600 °C*), they had to employ a *12 mT* work pressure and target powers of *100 W* (TiO_2) and *45 W* (Co) in order to observe an indication that the $\text{TiO}_2\text{:Co}$ alloy was present in the X-Ray diffractograms. A relevant conclusion of this study lies on the fact that the deposition temperature constitutes a critical parameter in the obtaining of the material, because for temperatures below *450 °C*, no crystalline phase whatsoever was present on the diffraction patterns; this fact was highlighted by the authors because it poses a contradiction against the results found with other research groups, in which the presence of polycrystalline thin films over silicon (100) substrates at temperatures as low as *350 °C* is reported.

Taking this bibliographic investigation as a fundamental background, several experiments were carried out in the laboratory for the fabrication of the thin films. After numerous intents at obtaining the $\text{TiO}_2\text{:Co}$ alloy, it was later established the definitive parameters for the synthesis of the thin films, and in this manner, four different series of depositions are presented in this work (**Table 2-1**). The idea of varying the synthesis parameters of the thin films fabricated was to observe and analyze the variation of the physical properties of the alloys once a specific parameter was changed under control; the conditions that were kept constant at all times were:

- ✓ Work pressure: $P_W = 2.5 \times 10^{-2} \text{ torr}$.
- ✓ TiO_2 target power: $P_{\text{TiO}_2} = 120 \text{ W}$.
- ✓ Co target power: $P_{\text{Co}} = 75 \text{ W}$.
- ✓ In-situ annealing temperature: $T_A = 450 \text{ °C}$.
- ✓ In-situ annealing time: $t_A = 2h$.
- ✓ Argon flux: $F_{\text{Ar}} = 20 \text{ sccm}$.

Series	Substrate temperature (T_s)	Deposition time (t_d)	Substrate
Series 1 (TiO ₂ thin films)	250 °C	30 min	Glass
			Titanium foil
			Silicon wafer
Series 2 (TiO ₂ :Co thin films)	250 °C	15min	Glass
		30 min	Titanium foil
		45 min	Silicon wafer
Series 3 (Co thin films)	250 °C	30 min	Glass
			Titanium foil
			Silicon wafer
Series 4 (TiO ₂ :Co thin films)	250 °C	30 min	Glass
	100 °C		Titanium foil
			Silicon wafer

Table 2-1: Synthesis parameters used in the fabrication of the samples presented in this work.

As an additional study, post-deposition annealing processes were carried out on the samples, implementing some thermal excitation to the surface to evaluate any change in the physical properties, namely three different annealings were made and classified as:

- ✓ Annealing A: 500 °C for 5 hours.
- ✓ Annealing B: 550 °C for 5 hours.
- ✓ Annealing C: 600 °C for 5 hours.

Only the thin films deposited on glass were annealed after the deposition. This process was made on an oven exposed to ambient conditions capable of reaching temperatures even higher than the ones that were used inside the DC magnetron machine. Beforehand, it was evident that this process would implement oxygen into the alloy matrix and therefore would severely affect the physical properties of the films.

With the samples fabricated, it was then possible to perform all the pertinent studies to determine the physical properties of the alloys fabricated in the laboratory. Taking advantage

of the robust equipment located at the Physics Department and other academic institutions, a comprehensive analysis of the thin films is presented in the subsequent sections.

2.2 Characterization techniques

As important as it is to fabricate the samples, perhaps even more relevant is their adequate characterization. The correct determination of the physical properties in the $\text{TiO}_2\text{:Co}$ thin films allows the determination of the potential applications in which the material could adequately perform. With that in mind, the main objective of this section is to present the functionality of some of the main characterization techniques employed along the duration of this work.

2.2.1 X-Ray diffraction

This technique consists of a compositional and structural method that allows not only the identification of the composition of a mono or polycrystalline material, but also its crystalline phases, crystalline structure, preferential orientation, etc. It consists on bombarding a sample with ionizing radiation (highly energetic) at different angles and detecting the reflected radiation from the sample to interpret the angles at which constructive interference between two separate waves coming from two adjacent planes of the lattice in the material exists [47].

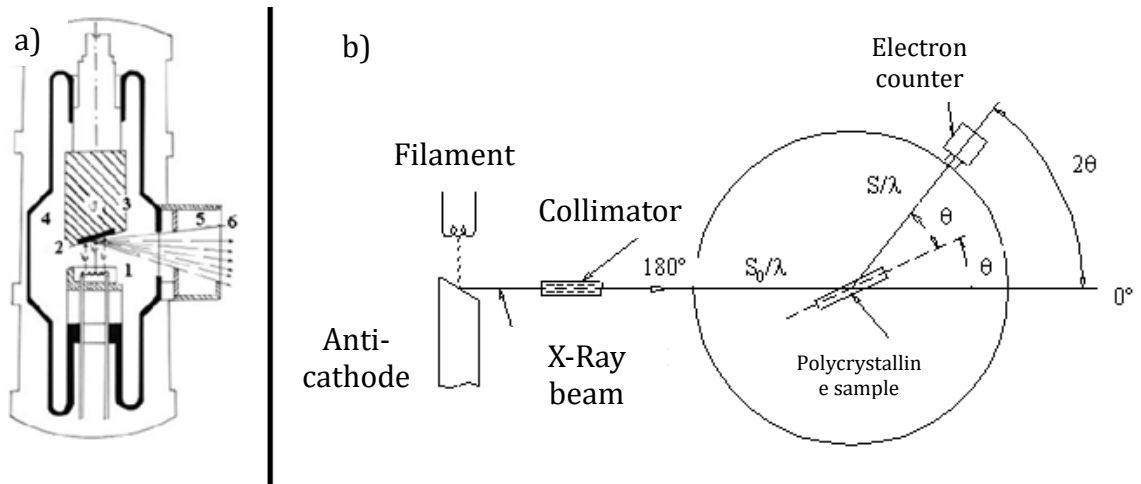


Fig. 2-5: a) X-Ray tube diagram. 1) Cathode, 2) Focus, 3) Anode, 4) Vacuum environment, 5) Diaphragm, 6) X-Ray beam, b) Operation schematics of an X-Ray diffractometer [65].

The measuring process is done with an X-Ray diffractometer [65], which is a device that basically consists of: An electron source¹¹ that works as a cathode, an X-Ray source¹² that works as anti-cathode, a vertical goniometer coupled with a sample-holder, a monochromator, a collimator, a detector and a cooling system for the X-Ray tube; these elements are placed in the system as **Fig. 2-5** shows.

The measurement begins with the emission of highly energetic electrons from the cathode; this emission is achieved by applying a *40 mA* current intensity to the tungsten filament which by the thermionic emission effect produces electrons that are then ripped from the source. Concordantly, electrons are accelerated towards the anticathode (X-Ray tube) using a *40 kV* acceleration voltage between the electrodes, and once in there, the first physical process by which X-Rays are produced occurs:

X-Ray emission by electronic incidence: X-Ray production is a consequence of the deceleration of electrically charged particles [66]. In this case, emission occurs when highly energetic electrons collide against a target given that the kinetic energy of the incident particles is very high, as a consequence, these particles can penetrate the inner energy levels of the atoms present in the target and then displace the electrons located in the K orbitals therefore leaving a vacancy on the first energy level, which will be occupied by an electron of the outer orbitals (L or M). When an electron undergoes a sudden decrease in its energy, dropping from a higher energy level to a lower energy level inside the atom, a photon with the characteristic frequency of X-Ray radiation will be emitted from it, the energy of this photon is characteristic for every material. **Fig. 2-6** shows this process of emission.

¹¹ Typically a tungsten (W) filament.

¹² Commonly a copper or cobalt made tube.

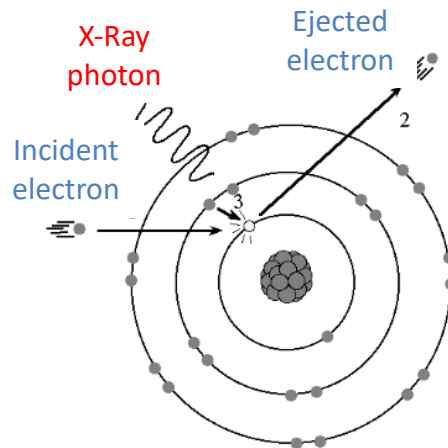


Fig. 2-6: Diagram of the X-Ray emission process by electronic incidence [67].

Once the highly energetic photons are produced, they will pass through a collimator and a monochromator to guarantee that the incident radiation is as coherent as possible; this is important because the diffraction would not be detected from the sample if the incident wave is not in the same phase.

As the X-Rays reach the sample, two non-mutually exclusive physical phenomena take place, the first is the emission of X-Rays by photonic incidence, and the second one is the X-Ray diffraction process.

X-Ray emission by photonic incidence: Given that every electromagnetic wave consists on oscillating electric and magnetic fields, the oscillation of the electric field in the incident radiation causes the electrons inside the atoms of the samples to oscillate at frequencies similar to those of X-Rays, this implies that said atoms will undergo excitation and relaxation processes (due to the transitions experimented by their electrons) having as a last consequence the emission of electromagnetic radiation. In other words, the atoms in the sample absorb and re-emit X-Rays, allowing the detector to receive the reflected radiation (in this case electronic transitions between $L \rightarrow K$ or $M \rightarrow K$ orbitals are also present). **Fig. 2-7** shows the diagram of this process; it also shows that as the wave reaches a set of crystallographic planes, two dispersion directions are perceived (transmitted and reflected directions).

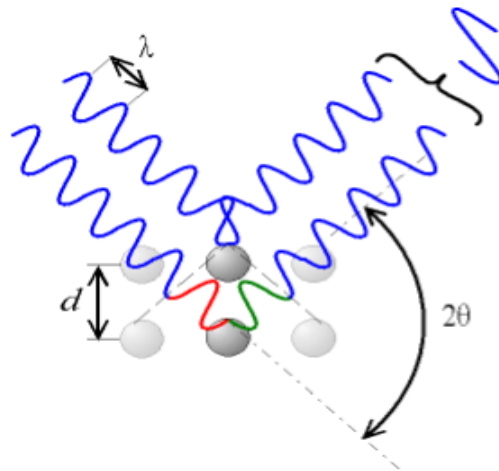


Fig. 2-7: Diagram of the X-Ray emission process by photonic incidence. Two incident waves are reflected with the same phase from the sample.

Finally, the last and most relevant physical process in this technique constitutes the X-Ray diffraction: Every monocrystalline material can be considered as a large set of diffraction slits in which the line division distance corresponds to the distance (d) between two adjacent planes of the crystalline lattice. Once the radiation reaches the planes of the material, these are diffracted at a determined angle; if two waves emitted from the sample are in the same phase, the maximum intensity condition, also known as constructive interference, will be achieved and therefore the detector will receive an abrupt increase in radiation which will be shown as a peak in the diffraction pattern like the one present in **Fig. 2-8a**.

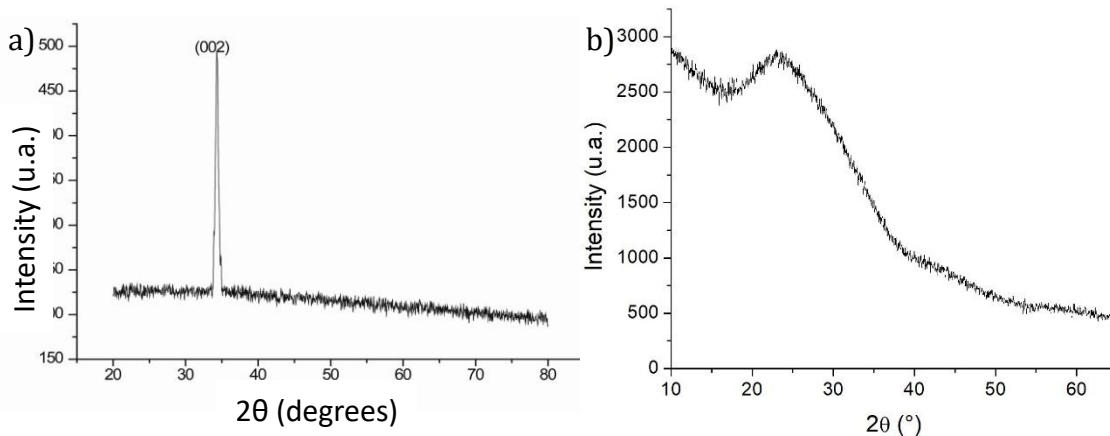


Fig. 2-8: X-Ray diffraction pattern of: a) A monocrystal (ZnO over a glass substrate) [68] and b) Amorphous soda-lime glass [69].

The maximum intensity condition will be present as long as the incident angle is adjusted in a way that it corresponds to a discrete solution of the Bragg relation:

$$\theta = \text{Sin}^{-1} \left(\frac{\lambda}{2 d_{hkl}} n \right) \quad (2.1)$$

In equation (2.1), λ is the wavelength of the radiation, n is an integer number and d_{hkl} is the distance between adjacent planes.

The radiation reflected from the sample reaches a scintillation counter and inside it the signal is amplified, allowing the computer to grant a curve of the intensity as a function of the angle (2θ) for further studies. The angle at which a diffraction peak is registered depends exclusively on θ , therefore the entire set of angles in a crystal at which diffraction occurs depends only on the dimensional characteristics of its lattice and not on its atoms positions [70], this implies that every X-Ray diffraction pattern is characteristic for every material and therefore allows the unequivocal identification and characterization of it.

Naturally, this discussion also applies to polycrystalline materials, with the difference that, in this case, there will be a higher number of angles at which constructive interference occurs, which results in a diffractogram exhibiting more peaks. In amorphous materials, compositional characterization is not possible with this technique due to a lack of a large-scale periodic structure inside the material, which will not allow the diffraction between planes and therefore the pattern will present what is called an “amorphous halo” like the one showed in **Fig. 2-8b**, the radiation coming from the background of the sample is called ‘Brehmsstrahlung’.

The samples were characterized using the X’Pert Pro diffractometer from PANalytical equipped with a Cu-K α source producing radiation of wavelength 1.54 \AA , operating at an electric tension of 40 kV and a filament current of 40 mA, measurements were taken in Bragg-Bretano configuration ranging from 10° to 90° (2θ) recording the signal every 0.02° ; the software used to analyze the results was the X’Pert Highscore Plus (which is a licensed program sold with the diffractometer) using the profile refinement method (Section 1.4) to identify the different structural characteristics of the deposited material.

2.2.2 Scanning electron microscopy (SEM)

This is a very useful technique to identify the morphological characteristics of the samples, for this reason, it was of great importance to understand the functionality and physical processes inside the microscope, **Fig. 2-9** shows a schematic diagram of a SEM equipment.

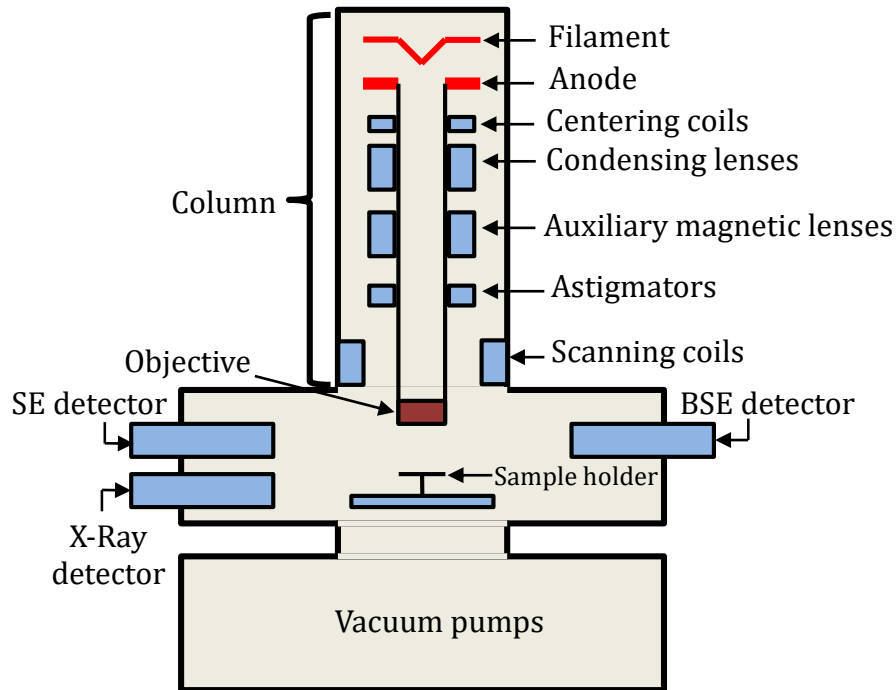


Fig. 2-9: Block diagram of a SEM equipment

This technique is based on the theoretical relation proposed by De Broglie in 1924 in which he proved that an accelerated electron beam has an associated wavelength (λ) given by equation (2.2):

$$\lambda = \frac{h}{mv} \quad (2.2)$$

Where h is the Planck constant ($6.62 \times 10^{-34} \text{ Js}$), m is the mass of the electron ($9.10 \times 10^{-31} \text{ kg}$) and v the velocity at which the particles are accelerated. If an electron beam is accelerated with a voltage V , then the kinetic energy it will gain is given by:

$$E_k = \frac{1}{2}mv^2 = eV \quad (2.3)$$

Where e is the charge of the electron (1.60×10^{-19} C). From this relation it is possible to infer that:

$$v = \left(\frac{2eV}{m}\right)^{1/2} \rightarrow mv = (2eVm)^{1/2} \quad (2.4)$$

Therefore from equations (2.2) and (2.4):

$$\lambda = \frac{h}{(2eVm)^{1/2}} \quad (2.5)$$

Replacing the numerical values in equation (2.5) yields:

$$\lambda = 0.1 \left(\frac{150}{V}\right)^{1/2} \quad (2.6)$$

Which means that the use of a 60000 V or an 80000 V acceleration voltage would imply that a certain electron beam will exhibit wavelengths ranging from 0.005 to 0.0043 nm, respectively. As a comparison, when an optical microscope is used, assuming a wavelength of 500 nm, the limit for resolution is around 217.86 nm¹³; in an electron microscope, this value would be enhanced by at least three orders of magnitude, given the fact that the wavelengths of the particles used are 10^3 times smaller, this proves to show the major advantage of using a scanning electron microscope in material science for the identification of possible surface nanostructures on a sample instead of an optical microscope [71].

The measurement starts with the emission of electrons from the electron gun. This device is a tungsten filament (similar to the one in an X-Ray diffractometer) that is heated using an electric current which consequently emits electrons that are then accelerated using electric tension ranging typically from 5 kV to 30 kV; the temperature at which the filament starts the

¹³ The power of resolution is defined as the distance between the maxima of intensity of two Airy discs when the maximum intensity of one disc matches the minimum intensity of another one [71]

thermionic emission is around 2427 °C, if a greater current is put through the filament, a greater number of electrons will be obtained, however it has to be mentioned that increasing this temperature may compromise the overall life of the filament.

Once the electrons are accelerated, they must travel the entire column distance shown in **Fig. 2-9**, this implies that the entire system must be kept in high vacuum conditions (less than 10^{-6} torr) for the mean free path of the electrons to be enough so they can reach the surface of the sample. An increase in resolution is achieved by focusing the electrons in an extremely thin beam, which is made employing copper lenses along the column. Once the electrons reach the sample, they begin to interact with its surface causing a great deal of physical phenomena and particle emission, the latter process is of great importance for the morphological characterization because the emitted particles are the ones responsible for the obtaining of the micrographs. **Fig. 2-10** shows the different particles ejected from a sample as it is scanned by an electron beam [72].

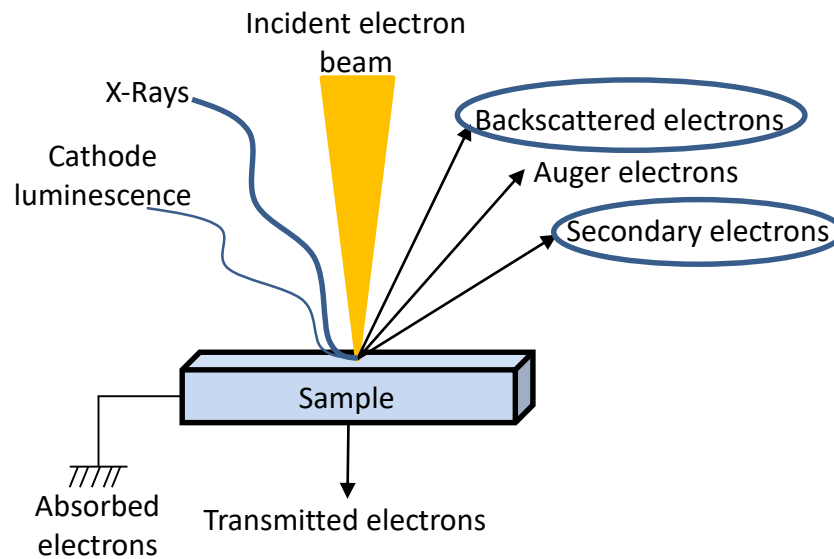


Fig. 2-10: Schematic diagram of the interaction between the incident electrons and the surface of a sample. The different types of particles emitted from it are also presented [72].

The secondary electrons are the particles ejected from the outermost regions of the material under study, these are valence electrons from the atoms that are ripped from them once the energy of the incident electron beam overcomes the ionization potential of an atom. Given the

fact that these are low energetic particles (inferior to 50 eV), only the outermost electrons can be emitted from the sample. After emission takes place, these electrons are detected by the secondary electron detector (scintillator working at 10 kV) coupled with a photomultiplier and an amplifier that translate the different intensities into an image on a computer. These electrons are useful for the study of surface topography.

Backscattered electrons, also known as reflected electrons, are particles directly coming from the incident beam, but reflected after interaction with the surface of the sample, undergoing a change in energy. These are emitted from deeper regions of the sample, not only from its surface, and therefore provide information from layers of the sample different to the ones studied with secondary electrons. Backscattered electrons are more sensitive to the chemical composition of the sample: The greater the atomic number (Z) of an atom inside the material, the greater the quantity of emitted backscattered electrons; therefore, given that the detector assigns a different brightness to different received intensities, the areas with heavier elements will appear brighter in a micrograph, whilst the areas with smaller Z numbers will appear more opaque. The detector of backscattered electrons allows not only a topographical, but also a compositional study of the sample.

Auger electrons come from a different emission process called Auger emission. When an incident electron has enough energy to rip electrons located at the most internal layers of an atom, they create a vacancy in said layer; when an electron from an outer layer of an atom descends to an internal layer, it loses energy which is manifest as the emission of a photon with an energy characteristic to every material and generally laying in the range of the X-Ray region of the electromagnetic spectrum; however in some occasions, the energy liberated from the electronic transition to a lower layer is transmitted to one of the outermost electrons, giving it the necessary impulse to be ejected from the atom. The energy of this emitted electron is equal to the energy lost by the electron undergoing the original transition, minus the binding energy of the electron ejected from the atom [73]. This type of process gives information regarding the atomic energy levels and elemental composition of a sample, however a scanning electron microscope is generally not equipped with an Auger electron detector, given that this would imply ultra-high vacuum working conditions (around 10^{-12} torr).

There is also a Characteristic X-Rays emission process (**Fig. 2-10**) when an incident electron beam interacts with a sample, this radiation is captured by an X-Ray detector and allows the compositional characterization of the material employing the energy dispersive X-Ray spectroscopy (EDXS) technique. In addition, **Fig. 2-10** presents other effects that the incident beam has on the material, which are consistent with cathode luminescence and electronic transmission phenomena, the latter is useful for another, even more rigorous, characterization technique known as transmission electron microscopy (TEM).

An appropriate SEM study requires a proper preparation of the sample, or else it may be damaged or burnt. A main concern lies on the fact that samples studied with a SEM microscope must be made preferably of a conductor material, this way the induced charge caused by the incident electrons will spread throughout its surface and will not focus in the region being studied which may cause burning damage to the sample (as is the case with insulating materials). Therefore, in cases where a biological, dielectric or in general an insulating type of sample is being studied, they should be previously covered by a thin film of a conducting material (typically a gold-palladium alloy).

Samples made for this work were characterized using the VEGA 3SB SEM system made by TESCAN, equipped with a tungsten filament, operating at high vacuum conditions (10^{-6} torr) thanks to the mechanic and turbomolecular vacuum pumps it comes with, the secondary electron detector is an Xflash 410m detector. Micrographs of the samples were taken at three different magnifications, namely *8.00 kX*, *24.00 kX* and *40 kX* with an electron acceleration voltage of *5 kV* and a beam intensity index of *5.00*.

2.2.3 Atomic force microscopy

This technique for topographic and morphological characterization is one of the different types of Scanning Probe Microscopy (SPM) that exist. Atomic force microscopy works under the physical phenomena of electrostatic repulsion and Van der Waals attraction and it corresponds to one of the experimental methods with the best resolution in the world (reaching atomic resolution).

The measuring process consists basically in scanning the surface of the sample with a probe placed on a cantilever (at a 10 \AA separation), detecting any change in its surface through the movement of a light beam coming from a laser, whose reflection from the cantilever points towards a photo-detector that allows the collection of the feedback of the topography in the material. The probe is usually made of silicon nitride (Si_3N_4), and the cantilever itself generally is made of pure silicon, an ideal probe should be one atom thick to guarantee a perfect resolution, however commercial probes have lengths of around 3 to 6 μm with a radius of 15 to 40 nm , which still imply resolutions of up to 0.1 nm , i.e. magnifications reaching $1000000\times$; the AFM microscope capabilities are comparable, if not better, than those of electronic microscopes.

Some advantages it pertains, as compared to other microscopy methods, is that an AFM measurement is done in three dimensions: The horizontal X-Y plane, and the vertical Z direction; the resolution in the Z direction is usually better than in the horizontal plane. In the same way, this technique does not discriminate whether a sample is conducting or insulating and it can be applied even to liquid materials. In addition, it can operate in three separate modes: Contact mode, non-contact mode and tapping mode [74].

In order to understand the different types of operation in an AFM, **Fig. 2-11** shows a curve of the potential energy of an atom or molecule as a function of the distance separating its center from the center of another atom or molecule interacting with it. This function is known as the Lennard-Jones potential and it is an empirical formula that adequately describes the potential energy of the bound state, for example, in a diatomic molecule; explicitly the Lennard-Jones potential is given by eq. (2.7):

$$E_p(r) = E_0 \left(\left(\frac{r_0}{r} \right)^{12} - 2 \left(\frac{r_0}{r} \right)^6 \right) \quad (2.7)$$

Parameters r_0 and E_0 are determined by the structure of the individual particles. For $r > r_0$ the slope of $E_p(r)$ is positive and therefore the force is attractive, for $r < r_0$ the slope is negative and the force is strongly repulsive, whilst for $r = r_0$ the force is zero (minimum of the potential energy). The previous reasoning is an approach describing two isolated particles interacting with each other, in reality this potential is present between the atoms of the sample and the

tip of the probe, which is not one atom wide, rather several atoms experiencing this potential at the same time and reacting to any changes in this repulsive and attractive forces.

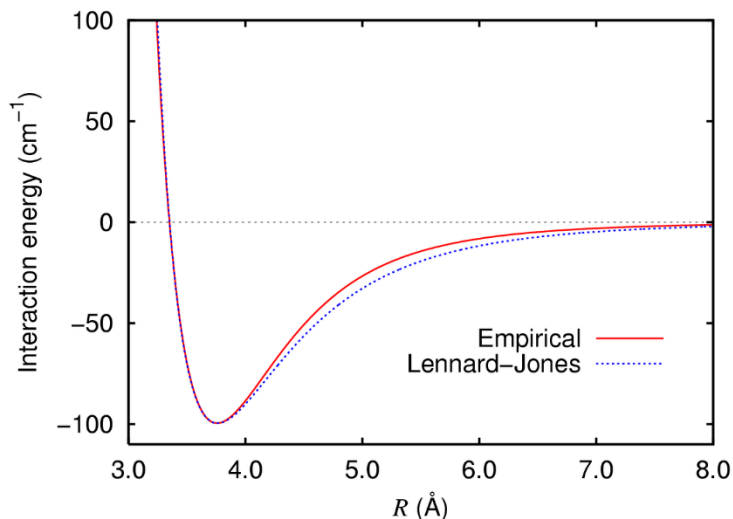


Fig. 2-11: Diagram of the Lennard-Jones potential for two interacting particles [75].

When the distance between the probe tip and the material under study is small (under 10 \AA), the repulsive force will be dominant and the AFM is said to be operating in *contact mode*, it is worth mentioning that the origin of this force are the so-called interchange interactions, which are produced given the overlapping of atomic orbitals at atomic distances [76], this mode is heavily influenced by friction and adhesive forces that may well damage the sample and distort the images. If the tip-sample distance is around 10 \AA , a polarization interaction will occur among the atoms of the sample; when an atom experiences an instantaneous polarization, it simultaneously generates polarizations in the nearby atoms, resulting in an attractive interaction due to the Van der Waals forces between the probe tip and the sample and as a consequence, it is said that the microscope is operating in *non-contact mode*. For tip-sample separation distances greater than 50 \AA , no feedback will be obtained from the surface of the sample.

The *tapping mode* is the middle point between contact and non-contact modes; when the contact mode is applied to a sample, the tip oscillates all over its surface at a small amplitude, however in this process, because of the adhesive forces of the material under study, the tip may result contaminated and the measurement distorted. The tapping mode eliminates this

disadvantage due to the fact that the tip is intermittently in contact with the surface and it oscillates with enough amplitude so as to prevent the tip from getting trapped under said adhesive forces, the result is that this mode provides the best resolution with a minimum damage to the sample; in most cases the non-contact mode is operated as a tapping mode instead. **Fig. 2-12** shows in a graphic manner the difference between the three mentioned operation modes of an AFM.

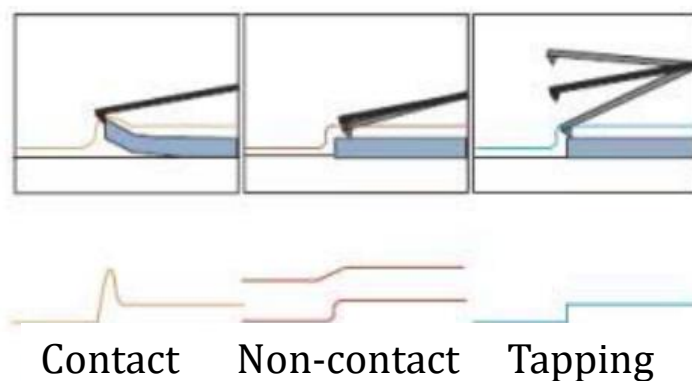


Fig. 2-12: Typical operation modes of an AFM microscope [76].

There are other additional microscopy modes that can be configured into an AFM equipment in order to evaluate other characteristics of a material, to mention a couple of examples, some microscopes can be used to evaluate electrostatic properties such as microelectronic structures, charges on insulating surfaces or ferroelectric domains; other can be employed to evaluate the presence and distribution of magnetic domains in the surface of a sample.

2.2.4 UV-Vis-NIR spectroscopy

Optical characterization of the samples was carried out using a Cary 5000 UV-Vis-NIR spectrophotometer made by Varian, this system is equipped with three different lamps, namely: A mercury lamp, a tungsten lamp and a deuterium lamp capable of covering a wide range of wavelengths from the electromagnetic spectrum¹⁴, the equipment also has the capacity of taking spectral transmittance, reflectance and absorbance measurements of thin

¹⁴ Typically, from 300 to 2500 nm, although when liquid nitrogen is used on a measurement, it can be expanded from 200 to 3000 nm.

films and liquid samples. In this work, it was only considered the transmittance and reflectance measurements taken every nanometer from 300 to 2500 nm.

The measurement is done illuminating the sample under study with monochromatic electromagnetic radiation at a 90° angle and collecting information of the transmitted or reflected radiation after it has interacted with the material in the thin film. The software incorporated with the equipment allows the obtaining of real time measurements as the sample is illuminated with different wavelengths, the resulting data is then stored in .CSV archives for further analysis.

The block diagram presented on **Fig. 2-13** helps to illustrate in a simplified way the path which light undergoes inside the equipment¹⁵, coming from the lamp, reaching the sample and then arriving at the detectors for the transmitted radiation feedback. This diagram also numerates the most relevant components of the equipment in a schematic way in order to get a better understanding of the characterization technique.

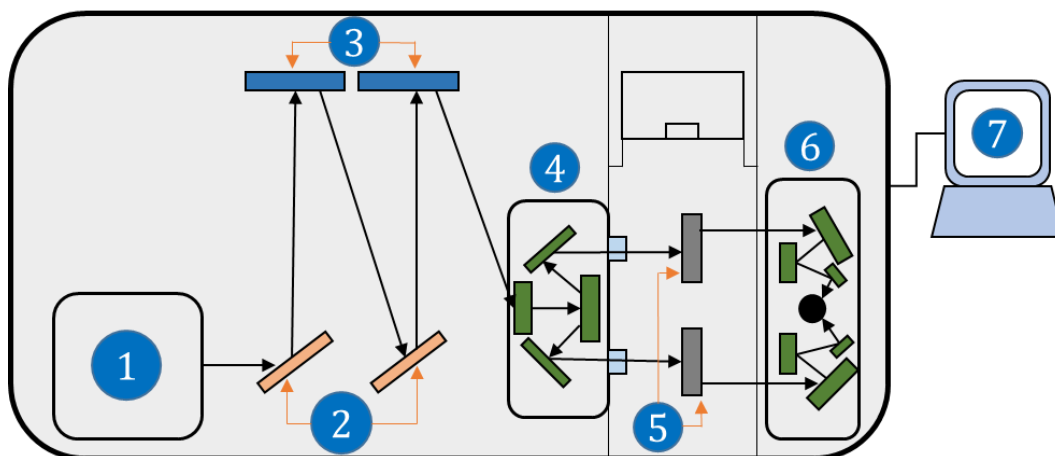


Fig. 2-13: Block diagram of an UV-Vis-NIR spectrophotometer. Black arrows show the path that light undergoes inside the apparatus.

¹⁵ This block diagram applies to a spectral transmittance measurement; the reflectance set up is different because it involves the use of an integrating sphere at point 5.

1. **Lamp compartment:** As it was mentioned before, the apparatus has three lamps: A mercury lamp for the emission of UV light, a tungsten lamp for the visible region of the electromagnetic spectrum and a deuterium lamp for the infrared radiation; every time a measurement of one of the three mentioned regions is completed, a carousel changes the lamp to continue on with the next region.
2. **Slits:** Given the fact that the radiation emitted from the lamps contains not just one, but several wavelengths in it, the diffraction slits allow the refining of the radiation in order to eliminate the interference between different wavelengths.
3. **Monochromators:** These are employed to select a single wavelength that is going to interact with the sample under study; this radiation is planned to be as monochromatic as possible.
4. **Mirror compartment (1):** In this part of the apparatus, several mirrors are employed to focus the radiation coming from the lamps towards the compartment where the sample and the reference are located.
5. **Sample compartment:** This is where the sample under study is placed, along with a reference material. This spectrophotometer has the capacity to employ two light beams that will be transmitted through a sample and a determined reference the user may employ.
6. **Mirror compartment (2):** In this section of the equipment there are, once again, several mirrors that allow the transmitted radiation from a sample to reach the detector (which corresponds to the black circle in **Fig. 2-13**).
7. **Computer:** After the detector has interpreted the information coming from the sample, using an interface through a Serial Port cable, the software of the equipment can then display the measurements in real time as a function of the incident wavelength for further analysis and studies.

3. Results and discussion

After several hours of laboratory work and analysis, this chapter looks to address and present the complete extent of the results obtained from the different characterization techniques explained in the previous chapter, along with its pertinent analysis and discussion. This entire chapter is the result of a remarkable collaboration between the Universidad Nacional de Colombia and other academic institutes, which further increased the scope of this research and gave it different important perspectives regarding its future development.

The $\text{TiO}_2\text{:Co}$ samples deposited using the DC Magnetron Co-sputtering machine under the synthesis parameters described in section 2.1 appeared to be opaque, black thin films with great adherence and visibly uniform. After the samples were subject to annealing processes, the aspect of the films changed, turning from a black to a brown-like appearance and a more translucent behavior.

3.1 Structural characterization

3.1.1 Characterization of as-deposited thin films

- Comparative study of series 1, 2 and 3

Taking as a guide the parameters established in **Table 2-1** of section 2.1, **Fig. 3-1** shows the comparative diffractograms of the first, second¹⁶ and third series of fabricated samples deposited on the three different types of substrates. It is worth mentioning that these diffraction patterns are consistent only with samples subject to in-situ annealing processes in high vacuum conditions.

¹⁶ The diffractogram from the second series taken in this study is the one corresponding to the sample fabricated with a deposition time of 30 minutes.

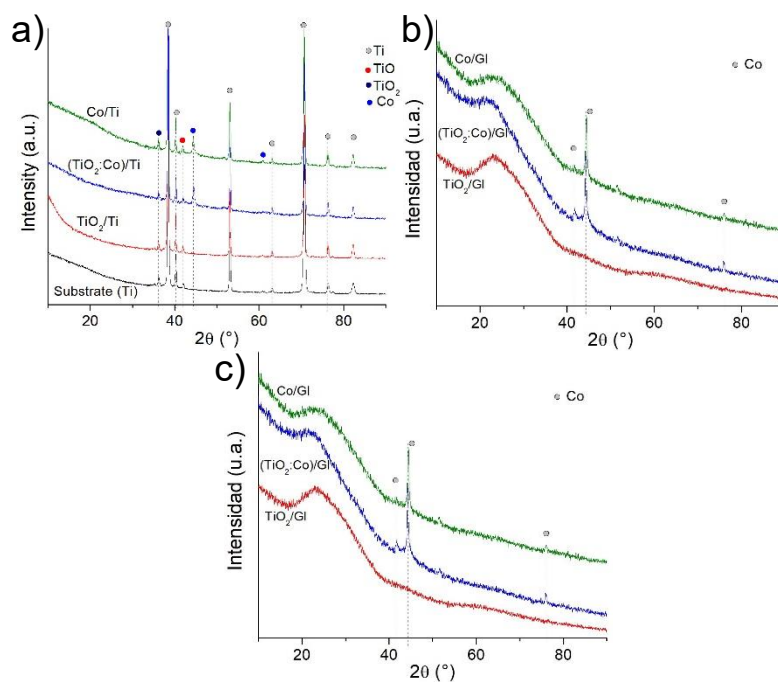


Fig. 3-1: Comparative diffractograms of samples deposited on: a) Titanium foil, b) Soda-lime glass and c) Silicon wafer.

As it is evident from the diffraction patterns, samples in which the cobalt target is used tend to exhibit more prominent diffraction peaks (different to the ones present in their respective substrates) consistent with a cobalt crystalline phase which has a cubic structure and spatial group $Fm3m$ (PDF 00-015-0806). Samples deposited in the silicon wafer (**Fig. 3-1c**) also have additional diffraction peaks associated with silicon oxide phases given the fact that all samples were subject to an in-situ annealing processes at 450 °C for 2 hours and free oxygen coming from the target can bond with superficial silicon atoms; the peak at 69° 2theta represents the preferential orientation of the silicon wafer used.

Fig. 3-1b perhaps holds the most illustrative result regarding the limited crystallization of TiO₂ thin films since the substrate employed was of amorphous nature (glass); the fact that samples made only of TiO₂ do not exhibit diffraction peaks leads to the possible conclusion that sputtering of titania does not procure a periodic arrangement of these molecules and therefore further treatment may be necessary for its proper crystallization; a further evidence of this fact is observed as the crystallite size of the cobalt thin film decreases from 301 Å to 142 Å when the TiO₂ is sputtered on the thin film.

- Series 2 characterization

Fig. 3-2 shows the diffractograms of as-deposited thin films associated with the second series of sample fabrication, the goal of these curves is to show the dependence on the structural behavior of the material as deposition time is increased from 15 to 45 minutes.

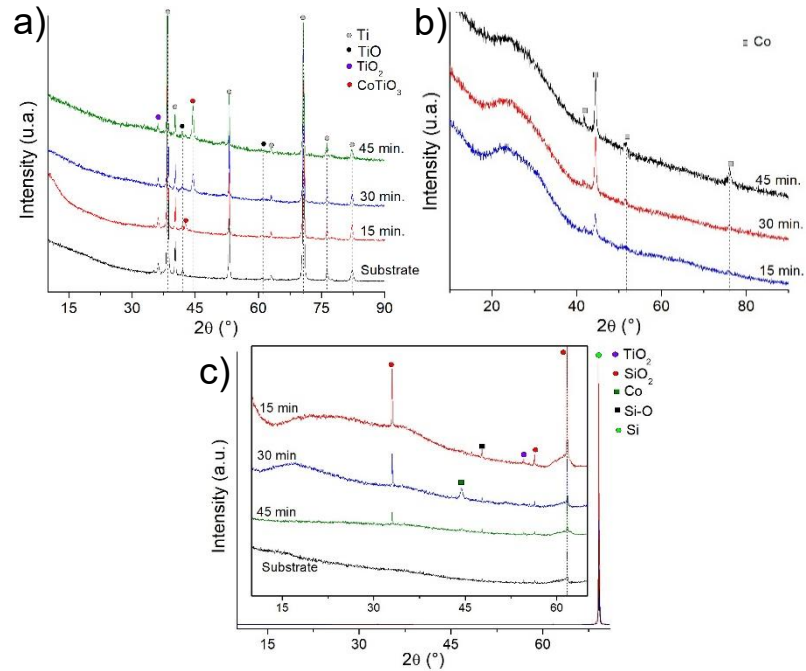


Fig. 3-2: Diffractograms of the samples from Series 2 deposited on: a) Titanium foil, b) Soda-lime glass and c) Silicon wafer.

Fig. 3-2a for example shows the presence of the ternary phase CoTiO_3 (PDF 00-029-0516), which was found using the ICOD crystallographic database; this phase becomes more prominent with increasing deposition times, however for the 15 minutes sample the peak is shifted towards lower values of 2θ , which can be associated with the low concentration of cobalt, given the short deposition time; crystallite sizes for these phase were $177.3 \pm 35.0 \text{ \AA}$ and $204.7 \pm 37.0 \text{ \AA}$ for the 30 and 45 minutes sample, respectively.

The CoTiO_3 phase found is an antiferromagnetic, functional oxide compound that has attracted special interest in the materials science area given that it can be used as a replacement of SiO_2 in CMOS devices [77], as well as its particular sensitivity to changes in relative humidity which make it a candidate for humidity sensor applications [78]. In the case of **Fig. 3-2b**, the curves

show an increase in crystallinity of a cobalt phase (cubic, with a lattice parameter of 3.54 \AA , given by the PDF chart), which is expected given the longer deposition times, and evident from the increase in intensity of the peaks and reduction of the amorphous halo coming from the glass substrate; crystallite size increased from $142.0 \pm 41.0 \text{ \AA}$ to $147.0 \pm 40 \text{ \AA}$ for the 15 and 45 minute sample, respectively, with no evident microstress peak broadening in them¹⁷.

Samples deposited on the silicon wafer (**Fig. 3-2c**) do not exhibit any remarkable change in crystalline phase formation, other than a decrease of the amorphous halo in the diffractogram for samples deposited for a more extended period of time, i.e. 45 minutes.

▪ Series 4 characterization

Continuing with the structural characterization, **Fig. 3-3** shows the diffractograms of the fourth series of samples. The thin films studied in this section correspond to as-deposited films, annealed at $450 \text{ }^\circ\text{C}$ in-situ for 2 hours under high vacuum conditions.

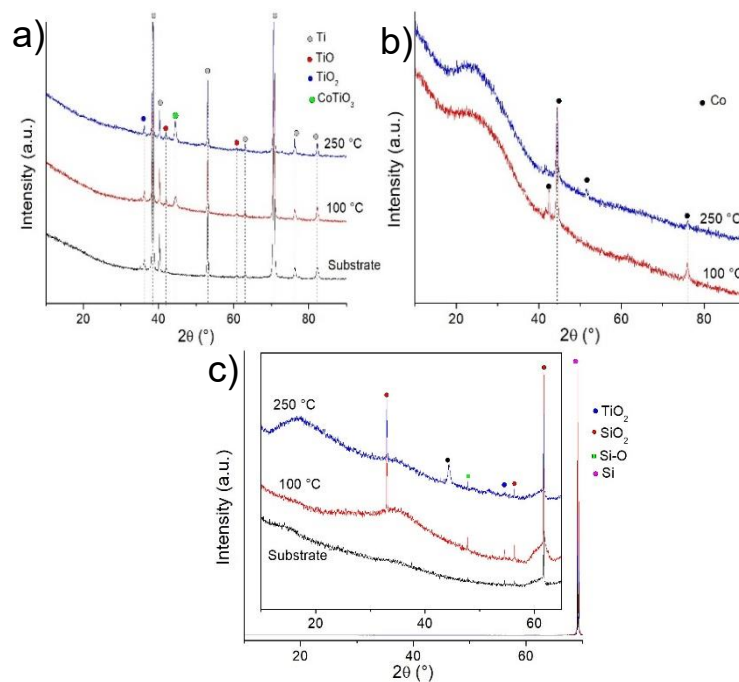


Fig. 3-3: Diffractograms of the samples from Series 4 deposited on: a) Titanium foil, b) Soda-lime glass and c) Silicon wafer.

¹⁷ This was determined analyzing the dependence of microstress broadening with the diffraction angle, finding that it had no direct correlation.

As it can be seen from the diffraction patterns, the behavior and crystalline phases present on the different substrates are similar to the ones identified in Series 2, considering that this study regards the evaluation of any changes in structural properties with substrate temperature (t_s). In this manner, Williamson-Hall plot analysis granted a variation in crystallite size from $189.0 \pm 15.0 \text{ \AA}$ to $178.0 \pm 13.0 \text{ \AA}$ for the cobalt phase present in the samples deposited on glass (**Fig. 3-3b**) as the substrate temperature was increased, which is evidence that greater thermal excitation does not necessarily procure large crystal formations, rather the elevated kinetic energy of the atoms may complicate the bonding and subsequent organization of cobalt atoms in the semiconductor matrix; for samples deposited in titanium foil (**Fig. 3-3a**), the crystallite size of the cobalt titanate phase increased from $107.0 \pm 32.0 \text{ \AA}$ to $177.0 \pm 29.0 \text{ \AA}$ with greater T_s , contrary to the previous result using soda-lime glass. For the deposition in the silicon wafer (**Fig. 3-3c**), the cobalt phase is only present in the sample with the greatest substrate temperature, whilst the $100 \text{ }^\circ\text{C}$ sample exhibited a more prominent amorphous halo, this indicates that in this particular substrate, the material requires an elevated thermal excitation in order to grant a crystalline compound.

Regardless of the fact that monocrystalline (Si wafer) or polycrystalline (Ti foil) substrates were used for the growth of the thin films; as-deposited and subsequently annealed in high vacuum samples presented limitations in the TiO_2 and Co crystallization, which prompted the action of annealing the material in conditions exceeding those of the DC Magnetron equipment, therefore the thin films were subject to the three different annealing processes mentioned in section 2.1 using a furnace capable of reaching temperatures up to $1200 \text{ }^\circ\text{C}$, however this task meant introducing additional oxygen to the material due to the elevated temperatures and the fact that the heating would be done in an uncontrolled atmosphere.

3.1.2 Characterization of thin films subject to annealing processes

- Samples annealed at $500 \text{ }^\circ\text{C}$

Fig. 3-4 shows the diffraction patterns of TiO_2 , $\text{TiO}_2\text{:Co}$ and Co thin films deposited on glass (Gl) substrates and annealed at $500 \text{ }^\circ\text{C}$ for 5 hours in a furnace without a controlled atmosphere. It is worth mentioning that the sample from Series 2 presented in this figure corresponds to the one with $t_d = 30 \text{ min.}$, so the diffractograms would be comparable.

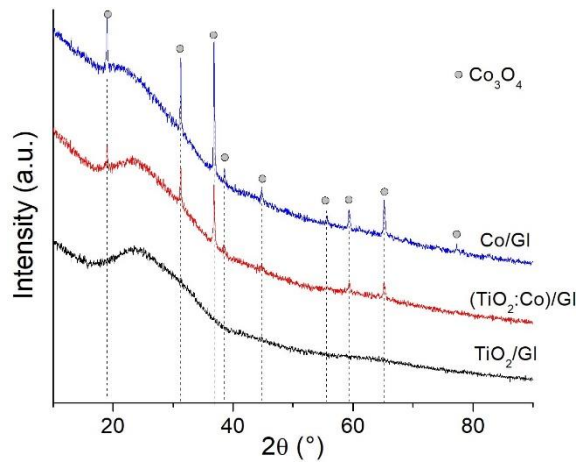


Fig. 3-4: Comparative diffractograms of samples annealed at 500 °C.

As it can be seen from the curves in **Fig. 3-4**, samples containing cobalt exhibited diffraction peaks consistent with a cobalt oxide phase (Co₃O₄, PDF 01-080-1533). The thin film made exclusively of titanium dioxide did not present any crystallization regardless of the prolonged annealing time. Co₃O₄ is characterized as an antiferromagnetic oxide of black appearance mainly used in biological, chemical and industrial applications [79], the most relevant of which concerns its implementation as a magnetic compound with uses in micro batteries and catalytic applications [80]. Once again, the Co thin film is more crystalline than the TiO₂:Co sample, which further corroborates the fact that sputtering of TiO₂ is a relevant factor in compound crystallization, mainly because the thermal excitation is not sufficient for the three different elements to bond and form a crystalline alloy.

In this manner, comparison between both types of thin films showed a crystallite size decrease from $557.0 \pm 57.0 \text{ \AA}$ to $520.0 \pm 50.0 \text{ \AA}$ for the cobalt oxide phase in the cobalt and TiO₂:Co thin films, respectively.

- Samples annealed at 550 °C

The next step in this study consisted in increasing the annealing temperature maintaining the deposition time as a fixed value. **Fig. 3-5** shows the diffractograms of samples from Series 1, 2 (30 min.) and 3.

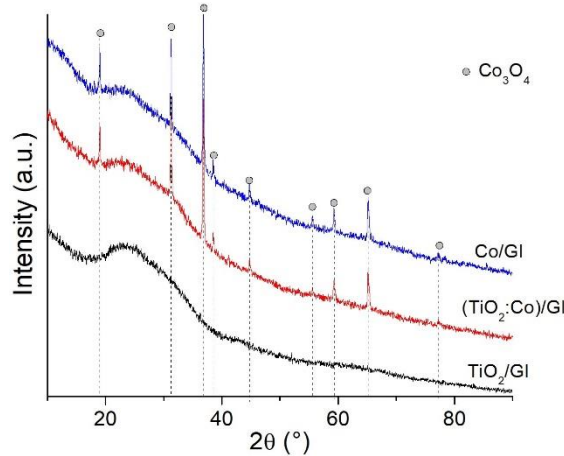


Fig. 3-5: Comparative diffractograms of samples annealed at 550 °C.

Once again, only the cobalt oxide phase is present in samples containing cobalt, whilst the TiO_2 thin film remained completely amorphous. The Co_3O_4 phase contains two different types of cobalt in its structure: Co^{+2} and Co^{+3} , the coexistence of this two species of the element exhibiting two different oxidation states obeys to the fact that this material is a mixed valence compound, therefore sometimes its formula is found to be written as $\text{Co}^{\text{II}}\text{Co}^{\text{III}}_2\text{O}_4$. The mechanism by which this molecule is stable corresponds to the Inner Sphere electron transfer [81] wherein electrons can sometimes be delocalized inside the structure of the material and occupy different valences in the two cobalt species. Crystallite size for the Co_3O_4 phase varied from $773.0 \pm 64.0 \text{ \AA}$ to $604.0 \pm 62.0 \text{ \AA}$ for the cobalt thin films and the $\text{TiO}_2\text{:Co}$ thin film, respectively.

- Samples annealed at 600 °C

Continuing with the annealing studies, as-deposited samples were subject to a 600 °C annealing for the same 5 hours in atmospheric conditions, the results are presented in **Fig. 3-6**.

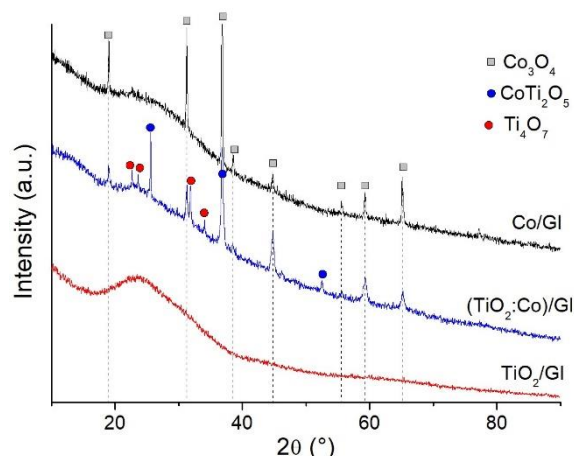


Fig. 3-6: Comparative diffractograms of samples annealed at 600 °C.

In this occasion, there were significant differences between these results and the previous ones. The TiO₂:Co sample presented a greater quantity of diffraction peaks, and therefore greater crystallinity as with the previous two annealings (**Fig. 3-4** and **Fig. 3-5**).

However this was not the only major change in the crystalline characterization because the sample from Series 2 also exhibited the presence of the ternary cobalt titanate phase (CoTi₂O₅, PDF 01-076-1600) and the titanium oxide phase Ti₄O₇ (PDF 00-011-0219), meaning that a TiO₂:Co intermetallic alloy was finally obtained with the DC magnetron deposition with subsequent annealing; this result is important because this type of alloy had not yet been synthesized using this configuration of the sputtering technique; it therefore opens a new perspective regarding the research of intermetallic alloys.

The CoTi₂O₅ compound is a type of cobalt titanate which in this case presents itself as an orthorhombic crystal system with the following lattice parameters: $a = 3.73 \text{ \AA}$, $b = 9.72 \text{ \AA}$ and $c = 10.08 \text{ \AA}$. Its space group is the $Cmcm$ and the space group number is 63. Its first crystallographic description was done in 1970, although a more accurate determination of the previously mentioned parameters was done by Muller-Buschbaum and Waburg in 1983 [82] as part of their study regarding pseudo-brookite compounds of the form A₂BO₅ and AB₂O₅, where A and B are generally transition metal elements. Deeper insight into this crystalline phase will be given in the following sections.

- Series 2 annealing study

Fig. 3-7 shows the dependence of the X-Ray diffraction results as the deposition time is varied from 15 to 45 minutes. Two separate annealing processes are presented as well.

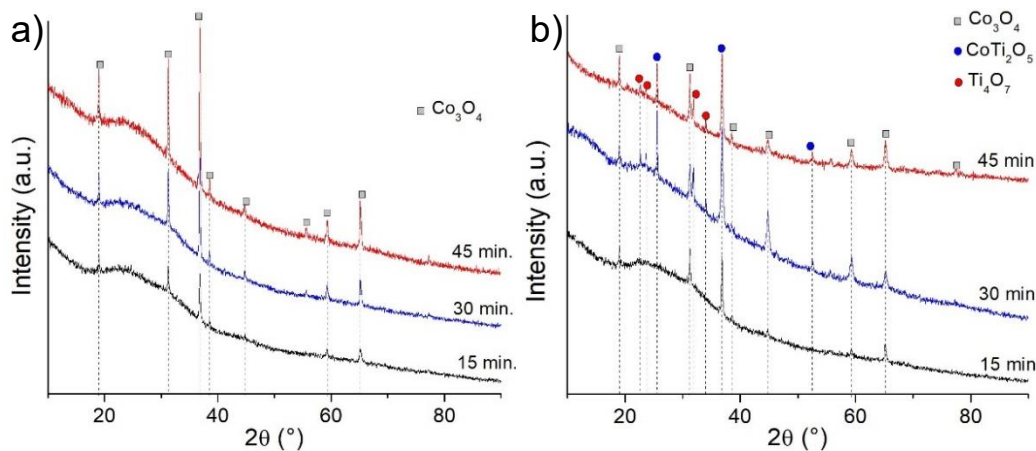


Fig. 3-7: Diffractograms of the Series 2 samples annealed at: a) 550 °C and b) 600 °C for 5 hours.

As it can be seen from the diffraction patterns, annealing at 550 °C does not procure the formation of any crystalline phases different than the cobalt oxide phase found in the previous studies; rather the main difference that the change in deposition time holds for these samples is an increase in crystallinity as a longer deposition time is used, yielding crystallite sizes of $450.0 \pm 49.0 \text{ \AA}$, $604.0 \pm 62.0 \text{ \AA}$ and $643 \pm 67.0 \text{ \AA}$ for the 15, 30 and 45 minutes' sample, respectively.

Samples annealed at 600 °C however, do present significant differences in their crystalline structure when deposition time is varied. The absence of the ternary CoTi_2O_5 phase in the 15 minutes' sample as compared with the other two configurations, indicates that this compound can only occur if a prolonged deposition time and sufficient annealing temperature is employed. The higher content of material in the 45 minutes' sample procures a more crystalline film, however there is certainly a greater preponderance of the Co_3O_4 over the CoTi_2O_5 phase, as compared to the sample with a t_d of 30 minutes. Crystallite sizes for the ternary phase varied from $399.0 \pm 52.0 \text{ \AA}$ up to $494 \pm 54.0 \text{ \AA}$ for increasing deposition times, with no evident microstress peak broadening.

The nature and stability of the CoTi₂O₅ ternary phase has been the subject of investigation for various research groups; one of the first published records of the study regarding said compound was carried out by Brezny and Muan [83] around 1969, whom, via the quenching method, were able to obtain the phase diagram of the alloy system CoO-TiO₂ which is presented in **Fig. 3-8**.

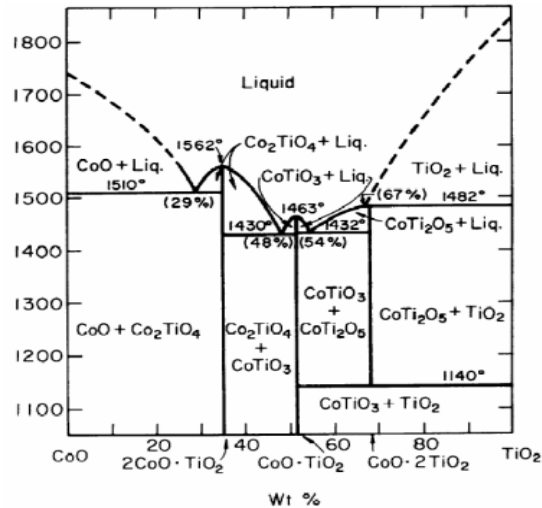


Fig. 3-8: Phase diagram of the CoO-TiO₂ system.

As it is evident from this figure, there are three crystalline phases (Co₂TiO₄, CoTiO₃ and CoTi₂O₅) which are stable in equilibrium, however one particular characteristic concerning CoTi₂O₅ is of note here and it concerns the fact that this phase is of unstable nature relative to the phase assemblage CoTiO₃ + TiO₂ below 1140 °C; such a property may point against the formation of this phase in the fabricated samples, but given the quasi-equilibrium nature of sputtering, it cannot be discarded, regardless of the instability below 1140 °C.

Even if this particular crystalline phase at the moment has a limited range of applications, the works from Balbashov, et al. [84] and Li, et al. [85] have shown a deeper insight into the magnetic, electrical and structural properties of this compound, however its potential use in the spintronic devices line of investigation remains to be seen, and therefore it is officially set as one of the perspectives of this work looking towards its performance in this sort of equipment.

- Series 4 annealing study

Following the sample fabrication order, **Fig. 3-9** shows the diffractograms for samples synthesized at different substrate temperatures ($100\text{ }^{\circ}\text{C}$ and $250\text{ }^{\circ}\text{C}$), annealed at $550\text{ }^{\circ}\text{C}$ (**Fig. 3-9a**) and $600\text{ }^{\circ}\text{C}$ (**Fig. 3-9b**).

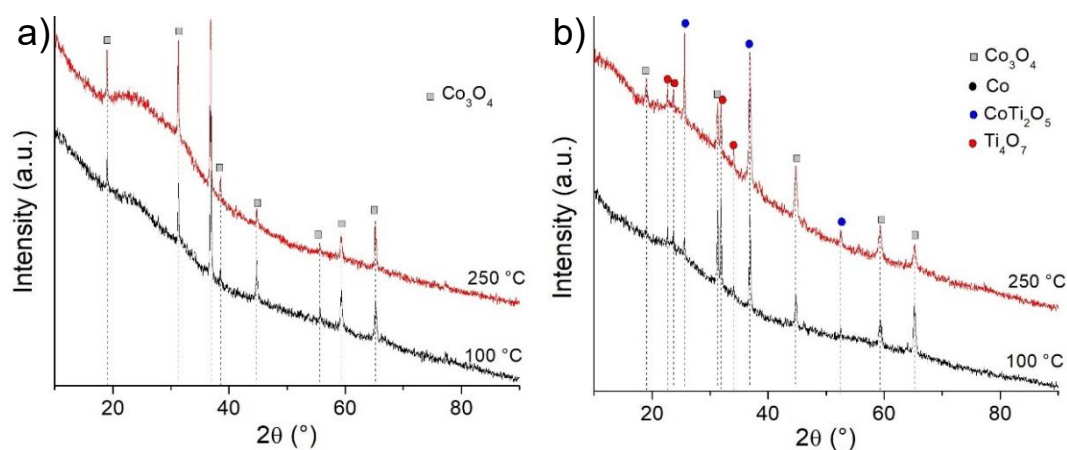


Fig. 3-9: Diffractograms of the Series 4 samples annealed at: a) $550\text{ }^{\circ}\text{C}$ and b) $600\text{ }^{\circ}\text{C}$ for 5 hours.

In this case, the results are comparable with the Series 2 characterization in regards to the fact that a $550\text{ }^{\circ}\text{C}$ annealing is not sufficient for obtaining a crystalline ternary compound, whilst the $600\text{ }^{\circ}\text{C}$ sample does exhibit the already known cobalt oxide, cobalt titanate (CoTi_2O_5) and titanium oxide (Ti_4O_7) phases. Since samples were deposited with the same deposition time of 30 minutes, a greater crystallization of the sample with T_s of $250\text{ }^{\circ}\text{C}$ is expected because the amount of material in both films is similar and therefore there will not be a screening of the ternary phase, as is the case with the 45 minutes sample (**Fig. 3-7b**). Crystallite sizes for the ternary phase varied in this study from $387.0 \pm 50.0\text{ \AA}$ to $399.0 \pm 52.0\text{ \AA}$ as the temperature was increased from $100\text{ }^{\circ}\text{C}$ to $250\text{ }^{\circ}\text{C}$.

Subsequent analysis concerns the morphological and optical characterizations, along with additional studies performed on the material using XPS measurements and PPMS data.

3.2 Morphological and topographical characterization

3.2.1 SEM characterization of as-deposited thin films

The goal of this study was to determine the possible variation in morphology of the TiO₂:Co thin films, given the different substrates, deposition times, substrate temperatures and annealing temperatures used in their fabrication. In this manner, **Fig. 3-10** shows comparative micrographs of TiO₂ samples deposited on the three different substrates; as it can be seen from them, the morphology varied between substrates, exhibiting a non-uniform film over the titanium foil, with considerable obvious cracks along its surface, which compared to **Fig. 3-10b** and **Fig. 3-10c** are certainly more prominent, in fact the thin film deposited over glass does not show any nanostructures at all.

An interesting result can be seen on the sample deposited on the silicon wafer, where the presence of darker areas is appreciated along the entire surface of the thin film; this formations are consistent with the first stages of nucleation of grain-like nanostructures, which may lead to the subsequent presence of crystalline grains spread throughout the surface of the material, this implies that a deposition time of 30 minutes may not be sufficient for the obtaining of a crystalline material, as was confirmed by the X-Ray diffraction measurements.

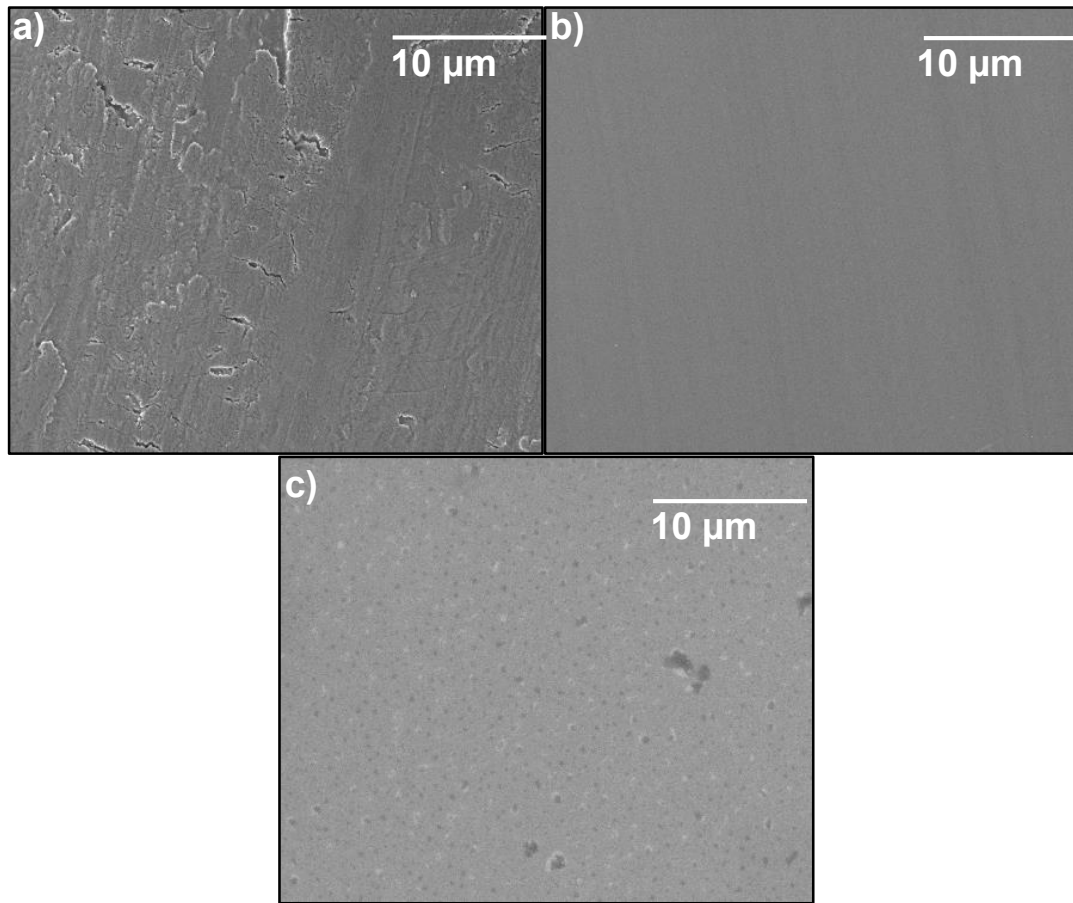


Fig. 3-10: SEM micrographs of samples from Series 1 deposited on: a) Titanium foil, b) Glass and c) Silicon wafer.

Fig. 3-11 shows the deposition of the alloy thin film ($\text{TiO}_2:\text{Co}$) on the three substrates, using a deposition time of 15 minutes, it can be observed that the results are comparable with the micrographs obtained in **Fig. 3-10**, save the fact that the darker spots are now found on the sample deposited on glass. It is worth mentioning that these thin films presented limited crystallization, only a cobalt phase was found over the glass and silicon wafer substrates, whilst a single ternary alloy phase was found using the titanium foil (**Fig. 3-11a**). Samples deposited on titanium foil appear to be with less uniformity given the flexible nature of the substrate, and the fact that it was submitted to a thorough cleaning process with a strong reagent. Given the resemblance of these thin films with the ones made exclusively of TiO_2 , it can be concluded that a deposition time of 15 minutes is not enough to observe large nanostructures on the surface of the material, regardless of the inclusion of cobalt inside the thin film.

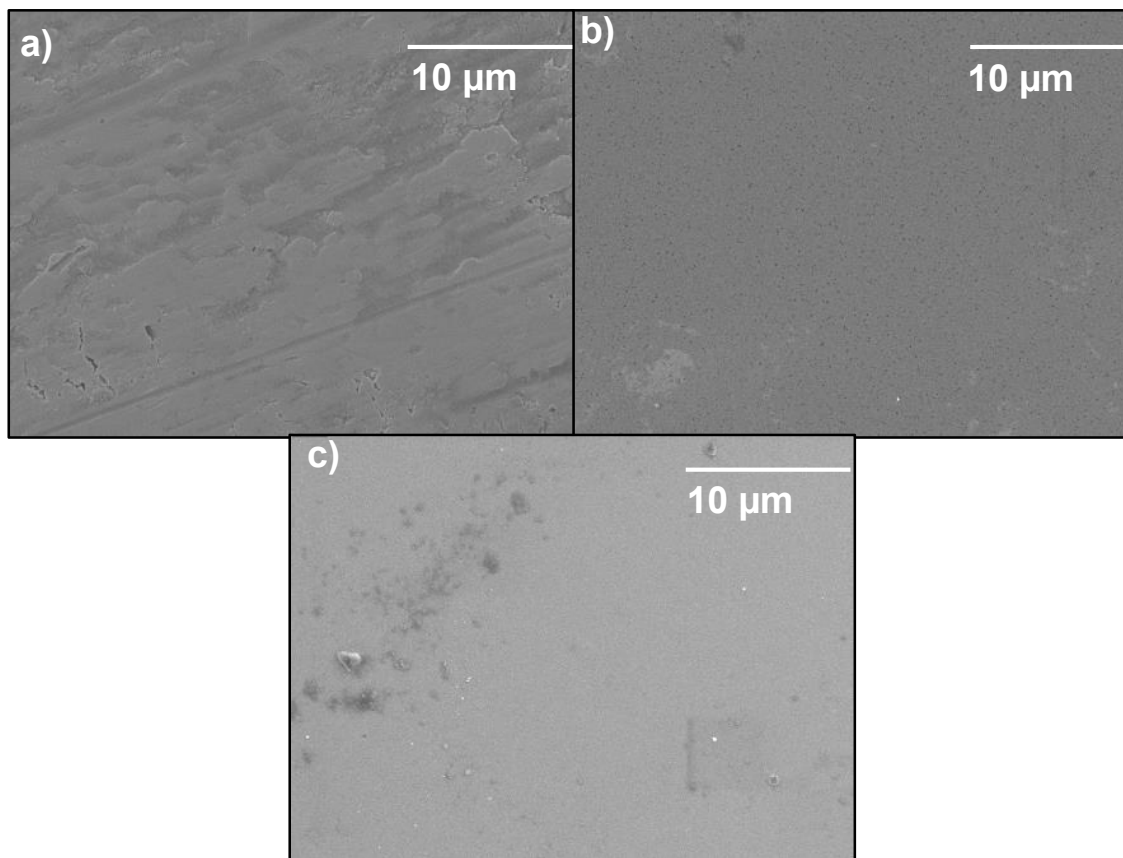


Fig. 3-11: SEM micrographs of samples from Series 2 deposited on: a) Titanium foil, b) Glass and c) Silicon wafer. Deposition time was 15 minutes.

Both **Fig. 3-12** and **Fig. 3-13** show a significant change in surface topography as compared with the previous two studies; these micrographs correspond to samples taken from the second series of fabrication, using 30 and 45 minutes as deposition time, respectively. As it can be seen from the results, the morphology of the thin films is evidently more granular in the three substrates, with the extent of the thin film covering the entirety of the used substrate.

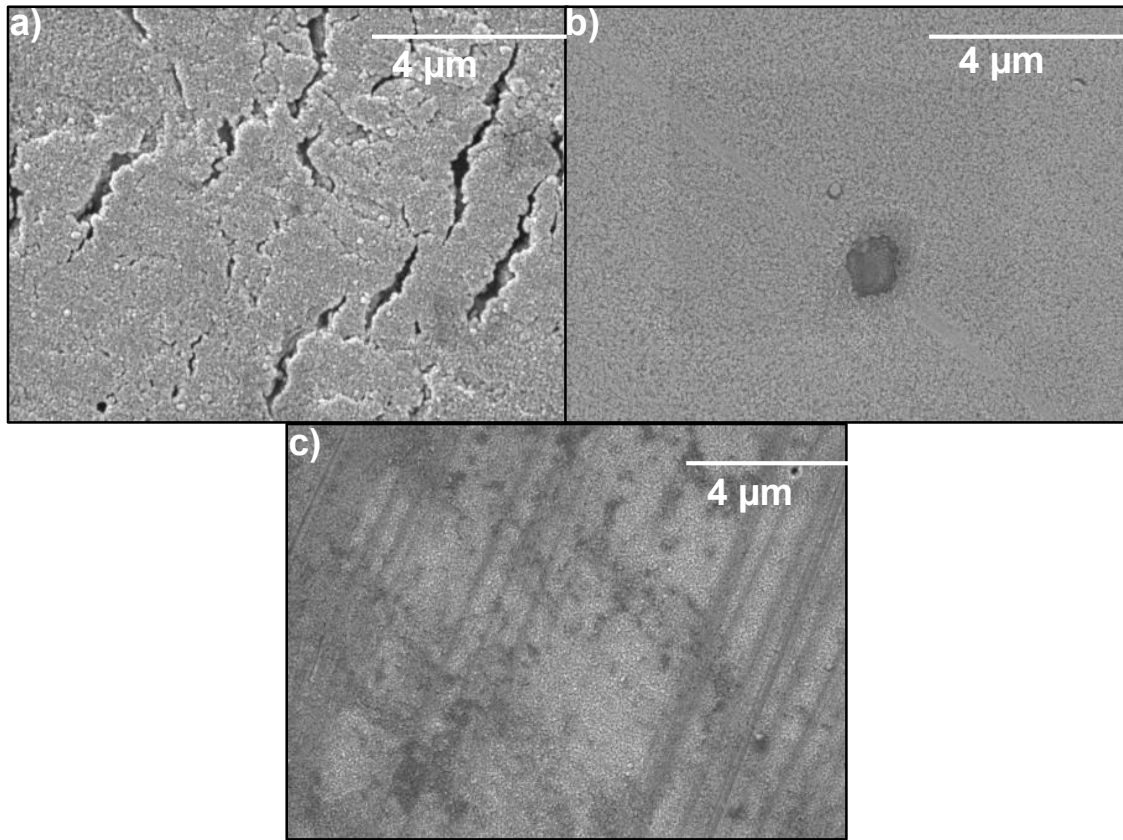


Fig. 3-12: SEM micrographs of samples from Series 2 deposited on: a) Titanium foil, b) Glass and c) Silicon wafer. Deposition time was 30 minutes.

Fig. 3-12a presents larger cracking on its surface as compared with its counterpart of **Fig. 3-13** where there is almost no visible cracks given the larger deposition time. As for **Fig. 3-12b** and **Fig. 3-12c**, the granular nanostructures seemed to be distributed in a more uniform manner, but still leaving some regions on the substrate uncovered by the thin film, which is not the case for the 45 minutes sample, where an expected thicker film was deposited, covering the complete extent of the substrate. It can also be appreciated that the size of the grain-like nanostructures is well below 100 nm and are seemingly larger in the 45 minutes' samples compared to the thin films with a t_d of 30 minutes; the apparent organization on a large scales of the nanostructures may be the cause for the cobalt crystalline phase present on the X-Ray diffractograms.

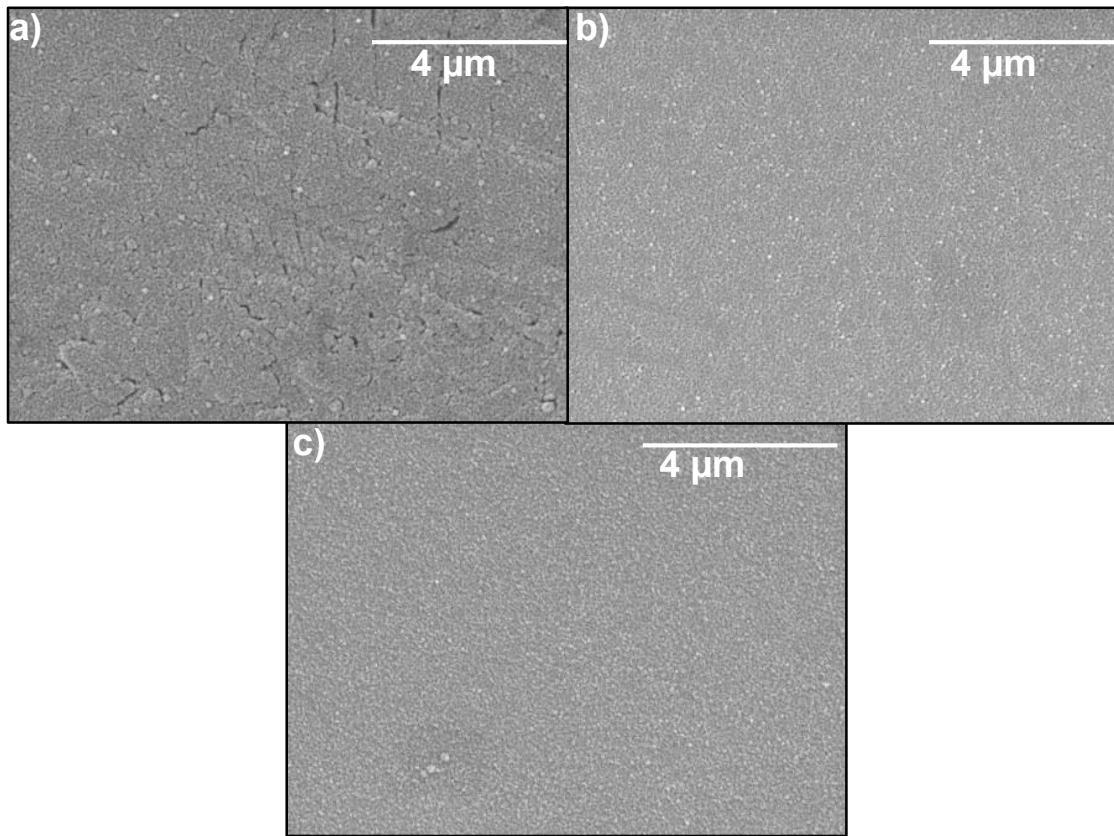


Fig. 3-13: SEM micrographs of samples from Series 2 deposited on: a) Titanium foil, b) Glass and c) Silicon wafer. Deposition time was 45 minutes.

Samples made using exclusively the cobalt target (Series 3) are presented in **Fig. 3-14**. The evidence of grain-like structures in these samples is also appreciated, and therefore allow to conclude that the inclusion of cobalt in the thin films procures the formation of this nanostructures in as-deposited films annealed in-situ. Once again, given the deposition time (30 min), the films deposited on the titanium foil presented considerable cracking, leaving several regions of the substrate uncovered; in the case of deposition over glass and silicon wafer, again a more uniform thin film was observed, with grain sizes inferior to 100 nm. The previous analysis have shown that deposition on glass and silicon wafer are of a similar nature (morphologically speaking) and therefore no relevant disparities between their topographical behavior was found.

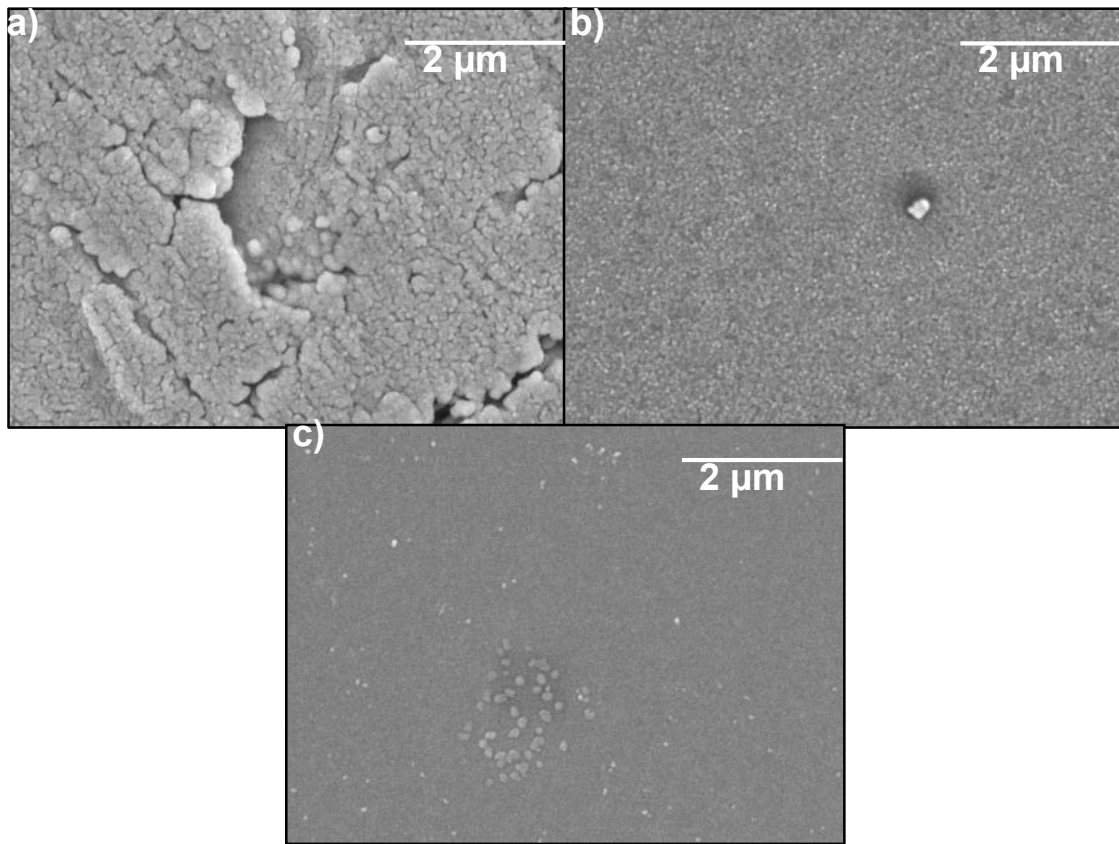


Fig. 3-14: SEM micrographs of samples from Series 3 deposited on: a) Titanium foil, b) Glass and c) Silicon wafer. Deposition time was 30 minutes.

The remaining analysis from the SEM technique, corresponds to the study of the variation of the morphological properties of the $\text{TiO}_2\text{:Co}$ alloys when the substrate deposition temperature was varied from $250\text{ }^\circ\text{C}$ to $100\text{ }^\circ\text{C}$. A recapitulation of **Table 2-1** indicates that the previous five figures are consistent with samples deposited at a substrate temperature of $250\text{ }^\circ\text{C}$ whilst **Fig. 3-15** presents the deposition over the three different substrates at a temperature of $100\text{ }^\circ\text{C}$. As it is evident from the micrographs, the samples deposited on titanium foil exhibit a granular morphology, with cracking over its surface similar to the anterior results; on the other hand, considerable uniformity of the thin film over glass and silicon wafer is observed, however on **Fig. 3-15b** the granular morphology is replaced with platelet-like formations after in-situ annealing at $450\text{ }^\circ\text{C}$, leaving also small cracks over the extent of the thin film, this indicates that deposition temperature in fact has a considerable significance regarding the resulting properties of the material, as was also the case in the structural characterization. Deposition time for these samples was fixed at 30 minutes so these micrographs would be comparable to

the ones presented on **Fig. 3-12**, which were prepared at a $250\text{ }^\circ\text{C}$ T_d . The results imply that the annealing temperature was enough to fuse together the grains with a smaller deposition temperature given the fact that the thermal excitation was not sufficient to form separate grain formations, as was the case when a greater $250\text{ }^\circ\text{C}$ temperature was employed.

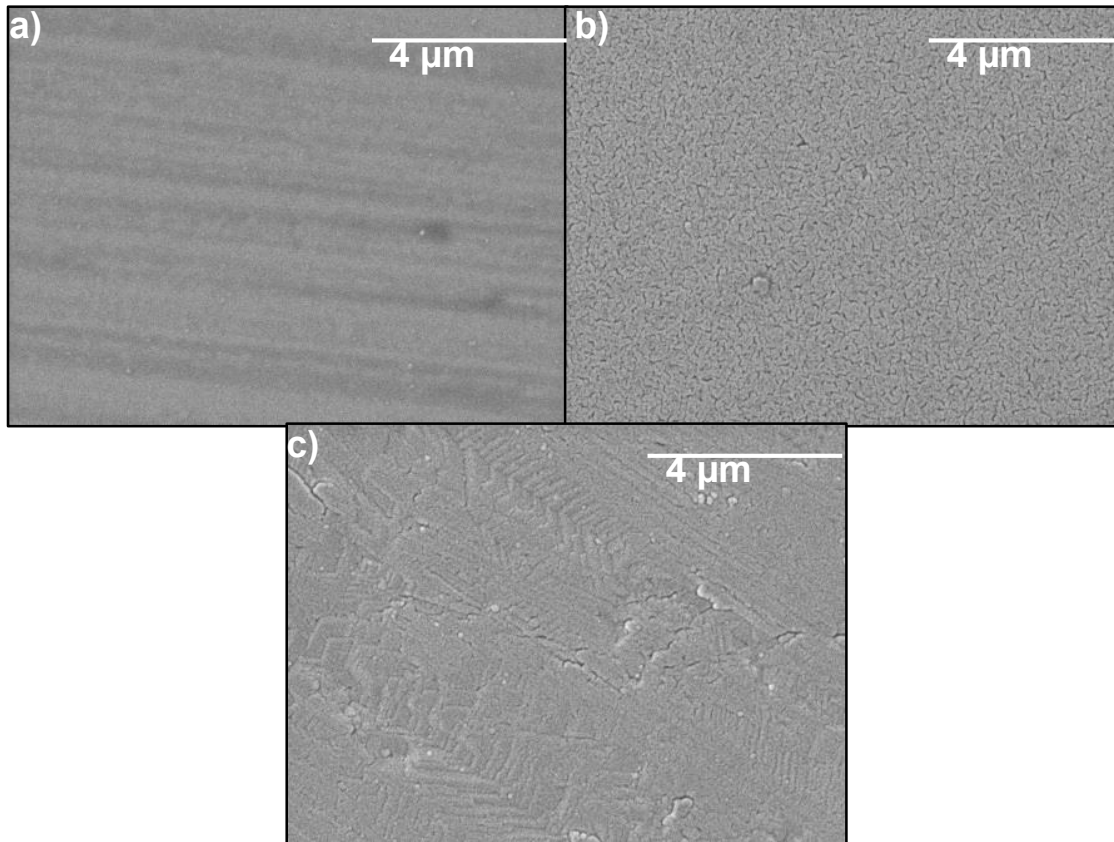


Fig. 3-15: SEM micrographs of samples from Series 4 deposited on: a) Titanium foil, b) Glass and c) Silicon wafer. Substrate temperature was $100\text{ }^\circ\text{C}$.

Having observed, from a structural point of view, how the properties of the material varied after a post-deposition annealing process was made over the samples. SEM micrographs were also taken from this samples, and the resulting images are significantly different than the ones presented along this section.

3.2.2 SEM characterization of annealed thin films

Beginning with **Fig. 3-16**; samples annealed at $600\text{ }^{\circ}\text{C}$ presented in general a radical variation in their morphology following this thermal excitation process. As it can be seen from the images, the thin film made exclusively of TiO_2 did not exhibit obvious changes compared to the as-deposited thin film from **Fig. 3-10b**, which grants a corroboration of the lack of diffraction peaks in the diffractograms for this sample, that not even after submitting it to extreme temperatures, was the material able to crystallize over the substrate or show any nanostructure formations.

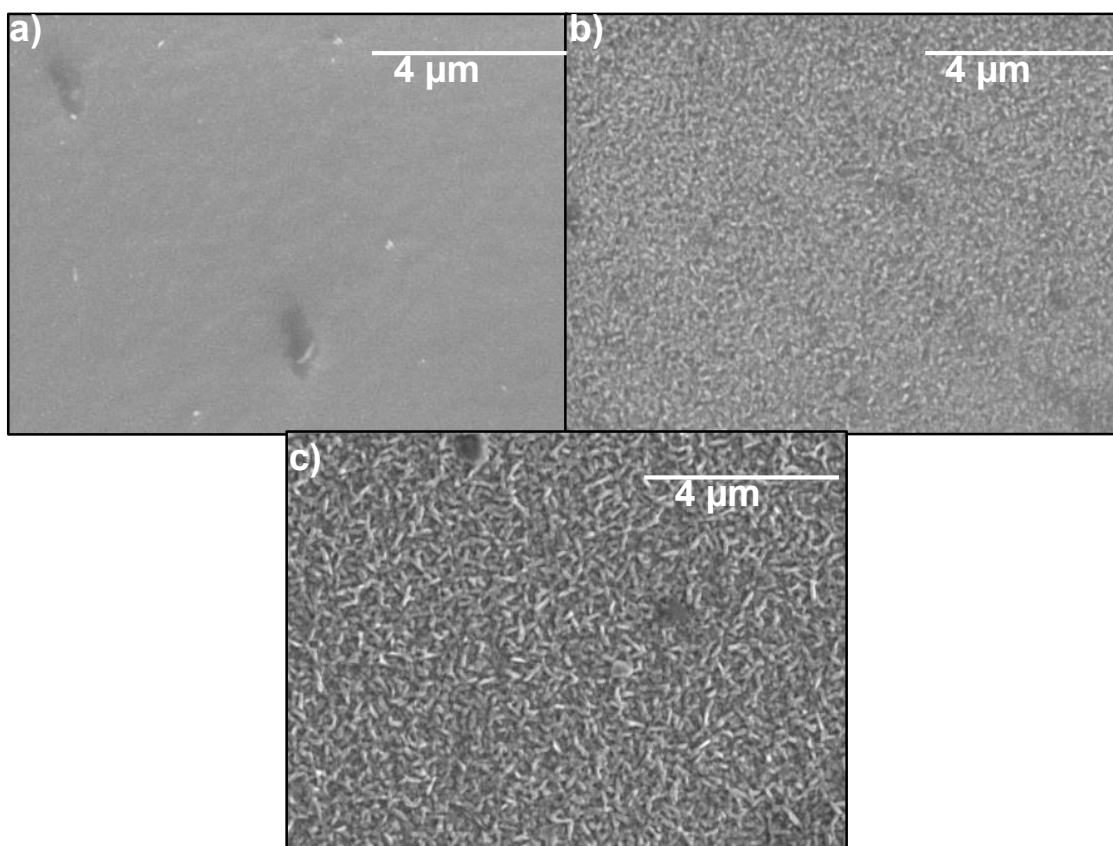


Fig. 3-16: SEM micrographs taken of samples from: a) Series 1, b) Series 2 (30 min) and c) Series 3, annealed at $600\text{ }^{\circ}\text{C}$ for 5 hours.

On the other hand, samples containing cobalt from Series 2 and 3 (**Fig. 3-16b** and **Fig. 3-16c**) do exhibit the presence of grain-like nanostructures, bigger in size than their counterparts from **Fig. 3-12b** and **Fig. 3-14b**, which is a severe difference in morphology of the surface in

the thin films, not to mention a confirmation of the crystalline nature of these samples, evidenced in both the structural analysis made using the profile refinement method (**Fig. 3-6**) and the increased grain size. It is also evident from the micrographs that the grain nanostructures appear to be bigger in size for the cobalt thin film as compared with the alloy thin film ($\text{TiO}_2\text{:Co}$), which is an important result in the evaluation of the growth of this material over soda-lime glass substrates, the inclusion of titanium dioxide causes the material to exhibit limited large-crystal formation and therefore diffraction peaks.

The previously mentioned contrast can also be appreciated in **Fig. 3-17** where the comparative SEM micrographs of the deposition time dependence are presented.

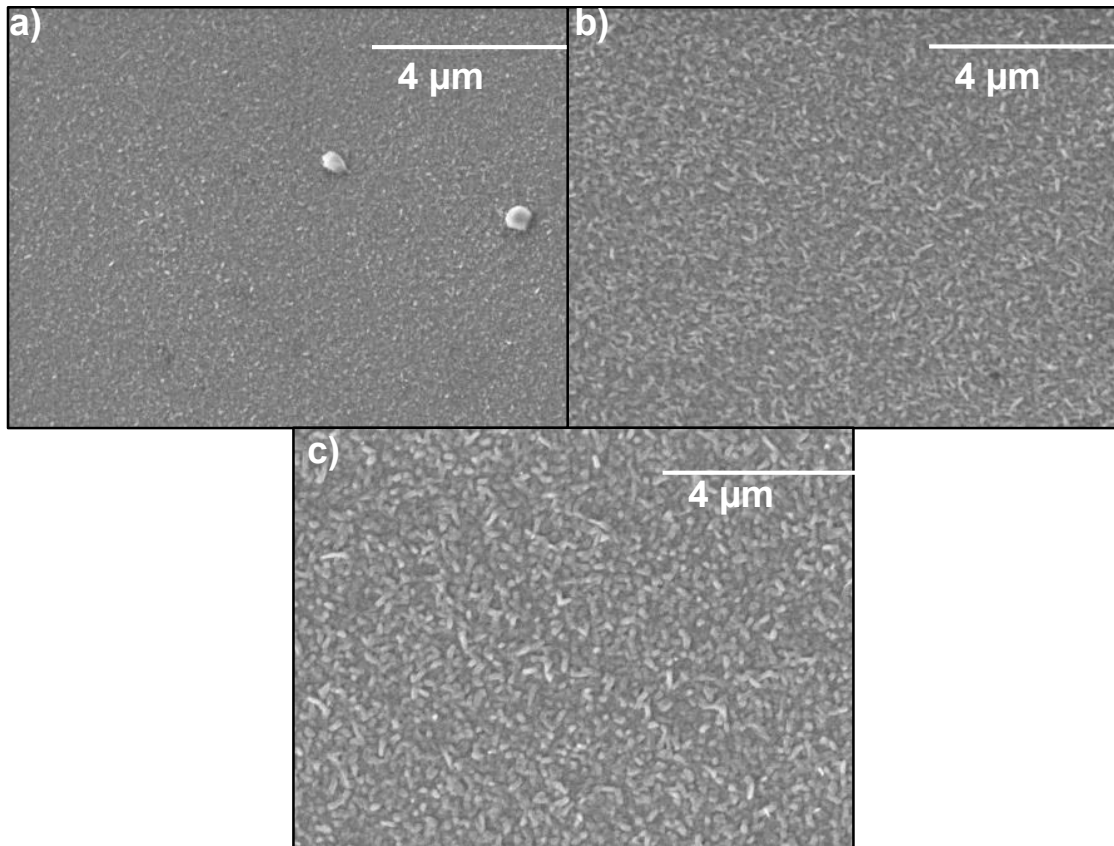


Fig. 3-17: SEM micrographs taken from the annealed second series of fabrication using: a) 15 minutes, b) 30 minutes and c) 45 minutes of deposition time.

However, the increase in the grain sizes (from less than 100 nm to well over 200 nm) are consistent with the increasing deposition time, rather than the alternate use of the magnetron targets. In this case the morphology of the thin films once again severely changes relative with their counterparts of **Fig. 3-11b**, **Fig. 3-12b** and **Fig. 3-13b**, presenting bigger nanostructures and an overall more uniform film after annealing at 600 °C for 5 hours. Recalling the fact that X-Ray measurements granted the presence of a ternary crystalline phase for **Fig. 3-17b** and **Fig. 3-17c**, it is possible to ascertain that said phase was identified given the bigger crystallites formed during annealing and evident now in the micrographs, and also that the decreased grain size for the sample deposited using a t_d of 15 minutes was not sufficient for the alloy to form and therefore exhibit diffraction peaks consistent with CoTi_2O_5 .

Fig. 3-18 shows the comparative SEM micrographs of the substrate deposition temperature study, which corresponds to the fourth series of fabrication according to **Table 2-1**.

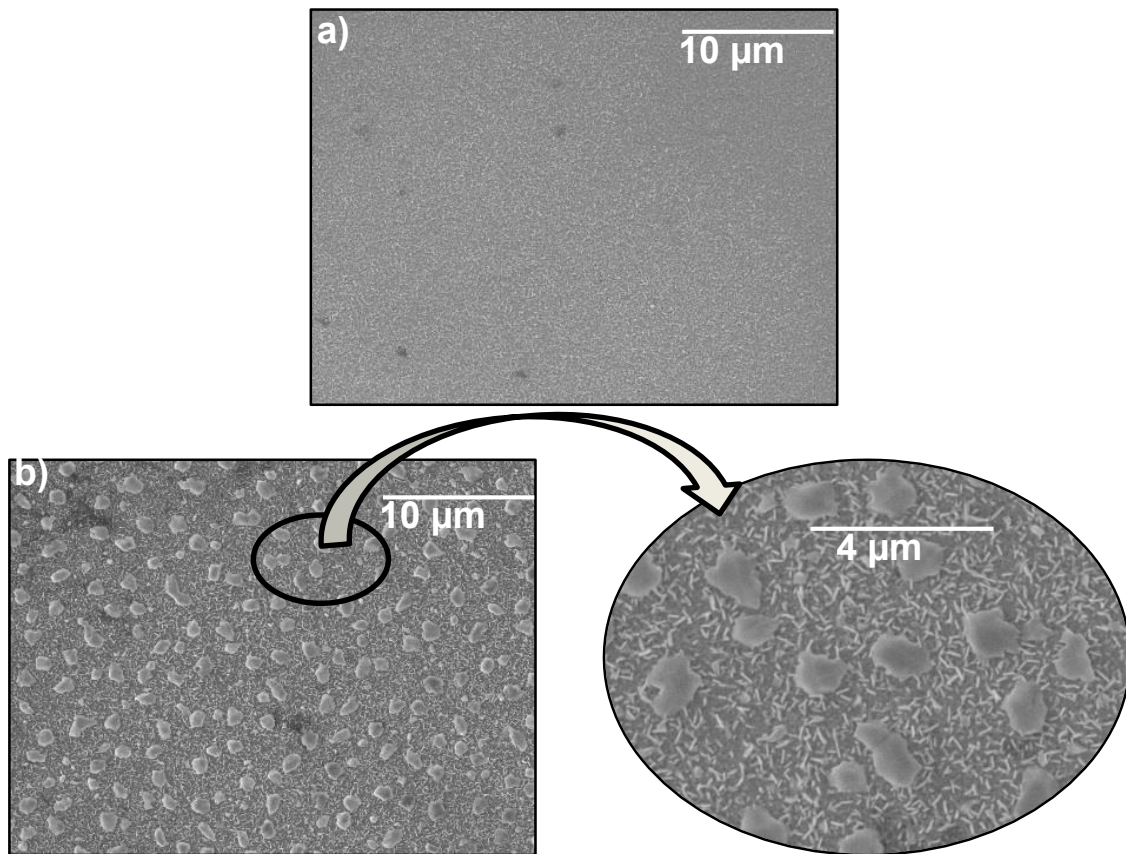


Fig. 3-18: SEM micrographs taken from the annealed fourth series of fabrication using: a) 250 °C and b) 100 °C T_s . Inset shows a magnification of the sample with 100 °C T_s .

As it can be seen from the images, the comparison between the sample deposited at 250 °C and 100 °C is somewhat puzzling; first, both films exhibit the formation of grain-like nanostructures on the surface of the substrate, which is in agreement with the previous studies, however the sample deposited at 100 °C also presents the formation of larger, micrometric grains in the entirety of the substrate, which are on average 1 μm in size and appear to be the result of advanced nucleation of small crystals made of the Co₃O₄ compound. The low deposition temperature seems to favor the increased growth of these structures given the fact that there is not sufficient thermal excitation at the moment of deposition in order for the cobalt to diffuse along the substrate, leaving small concentrations of the element along its surface which then, given the annealing process, are able to form a larger crystal by bonding with the oxygen present in the atmosphere, an indication of this result can be seen also in **Fig. 3-3b**, where a greater crystallite size for the 100 °C sample was determined, even before any annealing processes took place.

An additional important study that can be performed using the SEM technique corresponds to the evaluation of the average thin film thickness, which is presented in **Fig. 3-19**. The left image shows a micrograph taken at a 45° observation angle from the sample fabricated using 15 minutes as deposition time, whilst the right image shows a transversal cut of the sample from Series 2 deposited with a 30 minutes of t_d . As it can be seen from **Fig. 3-19a**, the thickness of this film appears to be well below 150 nm, a fact that is confirmed by **Fig. 3-19b**, in which it can be clearly seen that the thickness of the thin film does not exceed said limit, in fact, from this figure, it was determined that the average thickness for the TiO₂:Co thin film was 100 nm.

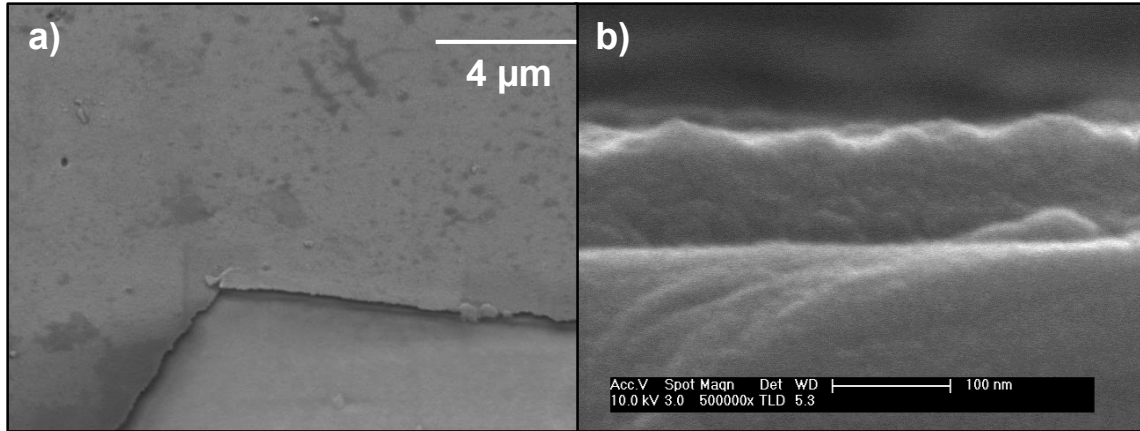


Fig. 3-19: a) SEM micrograph of a $\text{TiO}_2\text{:Co}$ thin film deposited with 15 minutes t_d and b) HR-SEM transversal micrograph of the $\text{TiO}_2\text{:Co}$ thin film with 30 minutes t_d .

This concludes the morphological study using the scanning electron microscope; the results obtained from it gave clarity regarding the growth of the material in crystalline and amorphous substrates as well as the variation of its morphology when it is taken to extreme temperatures. The following study concerns to the atomic force microscopy technique, which granted additional pertinent information regarding the fabricated thin films.

3.2.3 AFM study

As it was mentioned above, the following measurements were taken thanks to the AFM microscope provided in the Universidad de los Andes in Bogotá, Colombia. A special acknowledgment towards the Center of Microelectronics division is in order here.

Based on the previous methodology for the presentation of the results. **Fig. 3-20** shows the AFM micrograph of a $\text{TiO}_2\text{:Co}$ thin film fabricated with 30 minutes of deposition time, 250°C substrate temperature and deposited on a glass substrate.

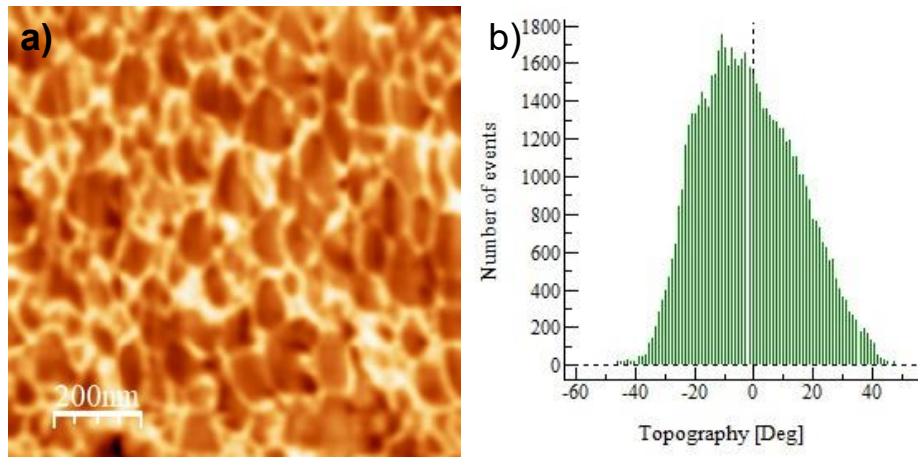


Fig. 3-20: AFM micrograph of an as-deposited TiO₂:Co thin film deposited on glass.

This image was taken using the tapping mode in the microscope and it covers an area of $1\mu\text{m} \times 1\mu\text{m}$. Concordantly, this micrograph yields a granular topography over the surface of the thin film, with the sample image statistics providing a 13.76 nm arithmetical average and 16.73 nm root mean square (RMS) roughness in the material [50]. Comparing the granular morphology in this study with the one done using the SEM microscope (**Fig. 3-12b**), it is evident that the AFM micrograph shows in a more clarifying manner the distribution of the grains over the surface of the thin film, given the fact that the scale in the image is far inferior to the scale in the SEM study.

On the other hand, **Fig. 3-21a** shows the AFM micrograph of the same thin film, after it was subject to a $600\text{ }^\circ\text{C}$ post-deposition annealing process in an uncontrolled atmosphere. As it is evident from it, the uniformly distributed grains appear to be larger in size compared with the structures of **Fig. 3-20**, which was also evident via the SEM micrographs presented above. Additional information from this micrograph yields a normal distribution regime for the height points on the surface (**Fig. 3-21b**), and also an average thin film roughness of 12.52 nm and a RMS of 15.68 nm , evidencing a decrease from the previously mentioned 16.73 RMS in surface roughness after the thermal excitation processes have taken place.

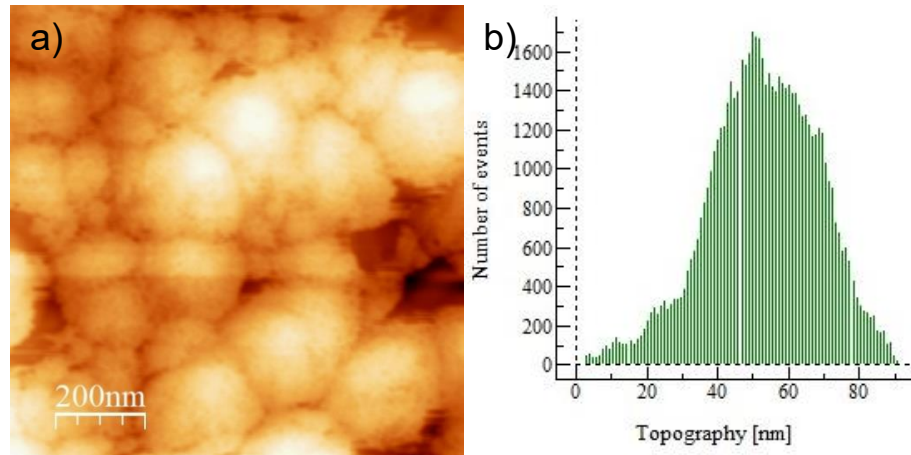


Fig. 3-21: a) AFM micrograph of a $\text{TiO}_2\text{:Co}$ thin film annealed at $600\text{ }^\circ\text{C}$ for 5 hours in uncontrolled atmosphere, b) Distribution of the height points over the thin film surface.

Therefore, a comparison between the thin films before and after annealing processes in uncontrolled atmospheres can be done, evidencing a slightly greater un-evenness in the as-deposited thin film surface than in the annealed thin film. The greater dispersion of the vertical height values from the overall mean in the as-deposited samples is caused by the presence of numerous smaller grains on the surface which lead to more distinct calculated values in amplitude and so it translates in a greater dispersion from a mean value. This is not the case in the annealed thin film, given the fact that the larger grains do not allow the software to detect major changes in the surface and therefore the dispersion from a mean value is not as elevated as in the previous case.

Having understood the various aspects regarding the morphological properties of the thin films, the following section will address the characterization of the optical response in the thin films when they are illuminated with electromagnetic radiation of several wavelengths.

3.3 Optical characterization

Continuing with the characterization process of the thin films, an important aspect which was set to address in this work concerned the variation of the optical behavior of the material depending on the synthesis parameters. For this purpose, as it was mentioned before, spectral transmittance and reflectance measurements were performed on the samples using the Cary 5000 UV-Vis-NIR spectrophotometer located at the Physics Department of the Universidad

Nacional de Colombia. The hereby presented results are a compilation of several comparative measurements taken from the thin films subject to in-situ and post-deposition annealing processes.

3.3.1 Characterization of as-deposited thin films

Given the fact that several of the as-deposited samples were synthesized over opaque substrates, namely titanium foil and silicon wafer, the chosen phenomenon to evaluate for these particulate films was the spectral reflectance, however, given also the mirror-like appearance of the samples, it was then evident that diffuse reflectance measurements would not bear significant results, therefore it was established that specular reflectance would be a more suitable property to evaluate. In this regard, **Fig. 3-22a** shows the comparative study of the films from Series 1 deposited on the three different substrates, whereas **Fig. 3-22b** shows the same set up for the samples from Series 3. As it can be seen from the curves in **Fig. 3-22a**, thin films made exclusively of TiO₂ exhibit a marked difference in reflectance behavior, for example, the material deposited over glass seems to reflect a greater amount of radiation than in the other two substrates which may indicate that absorption processes are most likely present for these surfaces in the entire evaluated spectrum.

In the case of **Fig. 3-22b** a similar differentiation can be made, obtaining a reflectance as high as 54% for the thin film deposited on glass, and as high as 5% for the samples on silicon wafer and titanium foil. This type of process in the glass substrate may appear anti-intuitive, given the fact that the aspect of the material is of opaque nature and therefore a greater absorption may be expected, however, the measurements revealed a strong reflectance of the film, which further enhances the knowledge of the physical properties of this material for its potential applications in science and engineering.

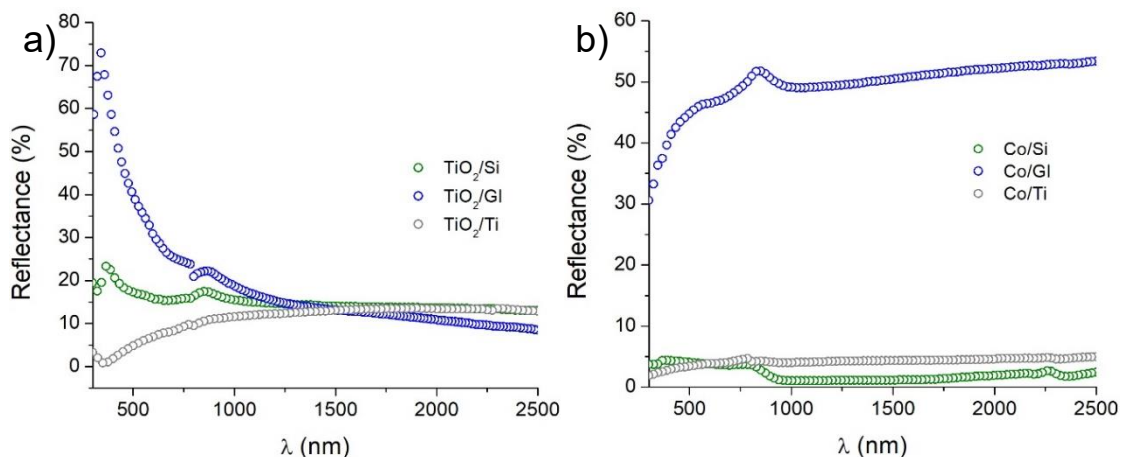


Fig. 3-22: Specular reflectance measurements of the: a) TiO₂ and b) Co thin films deposited on the three different substrates.

Continuing with the study, **Fig. 3-23** shows the comparative reflectance spectra of the TiO₂:Co thin films from the second series of samples according to **Table 2-1**¹⁸. The three plots summarize the three distinct deposition times employed.

In **Fig. 3-23a**, once again, the sample deposited on glass exhibits the greatest overall reflectance, followed by the thin film deposited on the silicon wafer and finally the thin film deposited on the titanium foil, which reaches a reflectance value as high as 25% for the infrared region. A similar behavior can be appreciated for the 30 and 45 minutes' samples (**Fig. 3-23b**) and **Fig. 3-23c**), which conclusively means that regardless the amount of material deposited on the substrates, the soda-lime glass presents a greater reflectivity relative to the incident radiation for wavelengths ranging from 300 to 2500 nm. The increase in reflectance of the samples deposited on titanium foil with increasing deposition time can be associated to the presence of the CoTiO₃ crystalline phase, which is more prominent in the 45 minutes' sample, making this thin films seemingly more sensitive to incident radiation.

¹⁸ For further synthesis parameters, refer to the cited table.

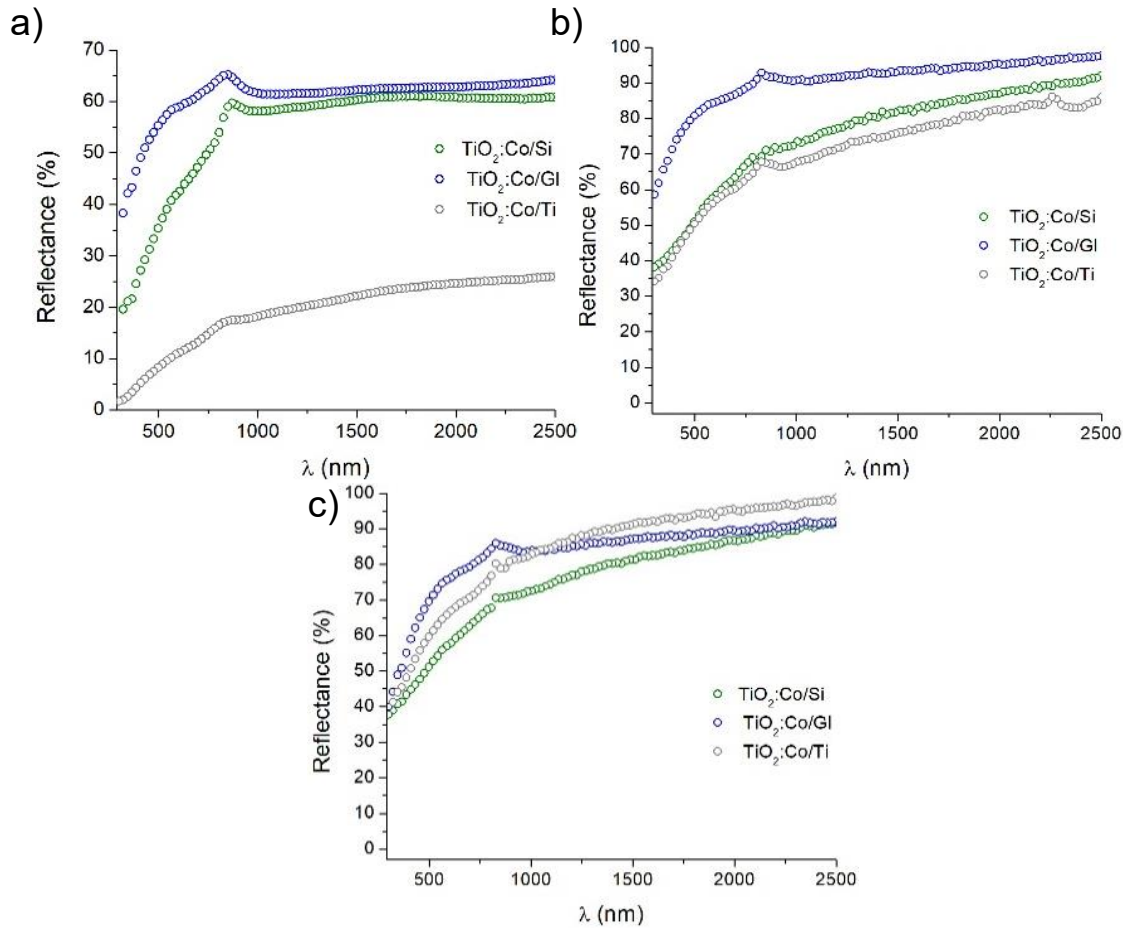


Fig. 3-23: Specular reflectance measurements of the TiO₂:Co thin films using a) 15 min. b) 30 min and c) 45 min of deposition time, over the three distinct substrates.

Fig. 3-24 shows on the other hand the reflectance spectra of the TiO₂:Co thin films from the fourth series of fabrication which, as it already has been mentioned, concerns the study of the physical properties depending on the substrate temperature at the moment of deposition.

Evident results further corroborate the previously two presented behaviors for the reflectance of the material deposited over glass, in which a greater overall reflectance is found exceeding in the majority of the spectra the reflectance of the thin films deposited on the silicon wafer and the titanium foil. Reflectance values close to 100% on the sample deposited over glass at 250 °C in the majority of the evaluated spectrum indicate that almost all of the incident radiation is reflected from the surface, leaving a thin film which is not translucent, nor absorbent, therefore its application for spintronic materials may be endangered by the fact

that it is a requirement in this research area to employ thin films with considerable transmittance values; this reasoning applies naturally to substrates with transparent behavior over a wide range of the electromagnetic spectra such as glass, quartz or other types of materials such as ITO or FTO.

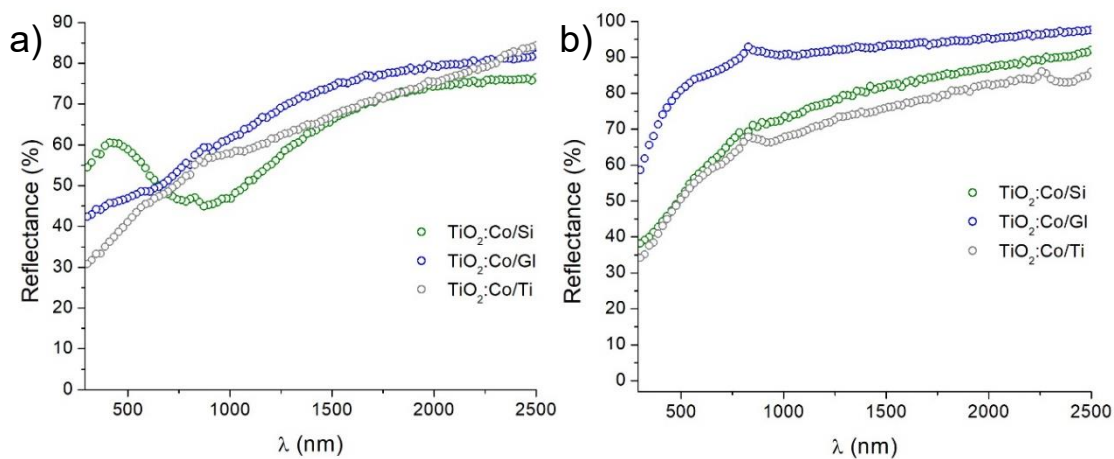


Fig. 3-24: Specular reflectance measurements of the TiO₂:Co thin films using a) 100 °C and b) 250 °C substrate temperature, over the three distinct substrates.

Until this part, given the naturally opaque nature of the silicon wafer and titanium foils substrates, a study regarding the transmitted radiation is not very helpful or informative, however it is possible to evaluate the transmittance for the thin films deposited on glass, which is the comparative study presented in **Fig. 3-25**, where the thin films from Series 1, 2¹⁹ and 3 are presented.

As it can be seen from the spectra, **Fig. 3-25** presents a transparent nature for the thin films from Series 1, while the samples containing cobalt (Series 2 and 3) present limited transmittance. Compiling these results with the reflectance measurements, it can be concluded that the TiO₂ thin films deposited on glass do not absorb light as much as the films containing cobalt; in the former case the radiation is either greatly transmitted (for wavelengths greater than 500 nm) or greatly reflected (for wavelengths smaller than 500 nm), and recalling expression (1.11) from Section 1.6, the absorbance percentage of a sample is calculated by subtracting the reflectance and the transmittance from the 100% incident radiation, giving as

¹⁹ As with previous cases, the samples from Series 2 corresponds to the thin film synthesized with a 30 minutes deposition time.

a result an average low value for absorbance (less than 10%). The TiO₂:Co thin films on the other hand, exhibit low transmittance along the entire evaluated spectra, coupled with an arguably strong reflective behavior in the same region, which grants the conclusion that any possible absorption effects in the thin film occur only for small wavelengths of radiation.

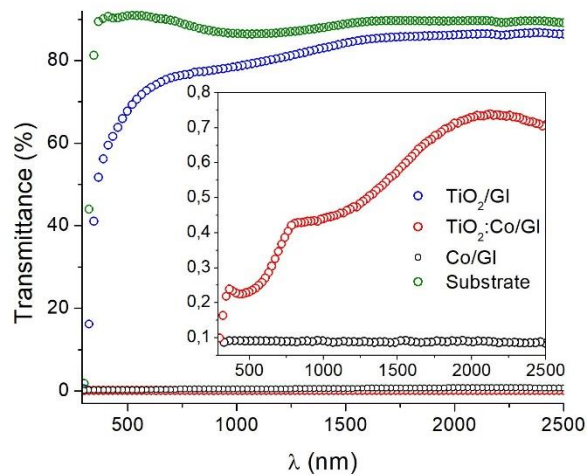


Fig. 3-25: Transmittance spectra for samples deposited on glass from Series 1 (blue) Series 2 (red) and Series 3 (black). Inset shows an amplification of the low transmittance region.

The remaining curve (Co/Gl) shows experimentally the predicted behavior for the thin films containing exclusively cobalt, which is an even lower transmittance of the thin film along the evaluated spectra, a phenomenon that was subject to prediction given the black, dark-like aspect of the thin films. In addition, recalling the reflectance measurements of this same sample (see **Fig. 3-22b**), the reflection of the incident light is quite low and therefore it can be concluded that a great amount of the incident radiation is absorbed by this surface as it was previously thought. In contrast with Series 1 and 2 the absorbance in the third set of samples is in fact greater than in the other two sets and therefore consistent with the nature of the material given the fact that no semiconductor compound was present in this case.

3.3.2 Characterization of annealed thin films

Following the same reasoning of the previous morphological study, the transmittance spectra of the annealed samples are hereby presented, starting with **Fig. 3-26**, which shows a comparative study of the optical response from samples of the first, second and third fabrication series, when monochromatic radiation is directed towards the surface of the thin

films. **Fig. 3-26a** and **Fig. 3-26b** concern the spectra of annealed samples at a temperature of $500\text{ }^{\circ}\text{C}$ and $550\text{ }^{\circ}\text{C}$, respectively. It can be seen from both curves that the behavior is remarkably different between the TiO_2 , $\text{TiO}_2\text{:Co}$ and Co thin films; moreover, recalling the results from **Fig. 3-25**, where the transmittance of the as-deposited thin films was evaluated, it can clearly be observed an increase in transparency over the infrared region for samples containing cobalt, namely samples from Series 2 and 3.

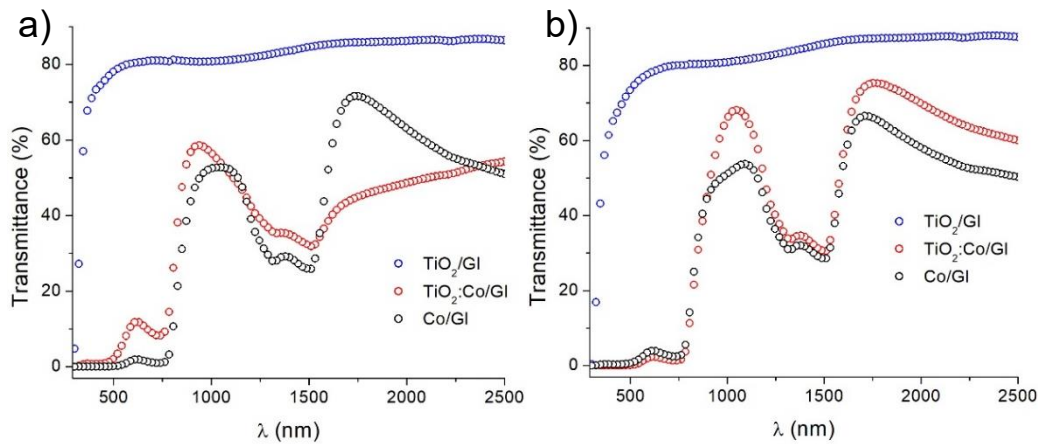


Fig. 3-26: Transmittance spectra of the thin films from Series 1, 2 (30 min.) and 3 annealed after deposition at: a) $500\text{ }^{\circ}\text{C}$ and b) $550\text{ }^{\circ}\text{C}$ in an air atmosphere.

This phenomenon can be associated with the reorganization of the crystalline structure inside the material, which was evident via the X-Ray diffraction measurements when a transition between cobalt and cobalt oxide (Co_3O_4) was observed; therefore, a change in structure clearly causes a change in transparency of the thin films, a characteristic that can be helpful when developing spintronic materials [86] given the fact that a certain transparency of the thin film is required, moreover, a possible decrease in light absorption of the thin films in the region between $\lambda = 750\text{ nm}$ and $\lambda = 1750\text{ nm}$ could be also responsible for this dramatic change, recall that **Fig. 3-25** showed an almost inexistent transmittance of the films, which is compensated with higher absorption values. In addition to the previous analysis, the presence of interference fringes along the evaluated electromagnetic spectrum was evident for samples containing cobalt, which means that the uniformity of the thin films is enough to fulfill the interference condition from eq. (3.1)

$$2nd = m\lambda \quad (3.1)$$

Where n represents the refraction index, d is the thickness of the thin films, m is an integer or half-integer depending on whether the transmittance exhibits a maxima or minima, respectively and λ is the incident wavelength²⁰. Even though in both Series 2 and 3 the interference fringes are present, in the red curve (TiO₂:Co thin film) the attenuation of the transmittance appears to be less pronounced than in the samples containing only cobalt, which grants a deeper insight regarding the addition of TiO₂ over the substrate.

Contrary to the previous plot, **Fig. 3-27** shows a more pronounced attenuation for the alloy thin film as compared with the sample containing exclusively cobalt; this figure shows the optical response of the thin films from series 1, 2 and 3 after they were subject to annealing at 600 °C for 5 hours after deposition and even though a similar comparison between samples can be made regarding the superior transmittance for the TiO₂ thin film, the clear difference between the red and black curves in which the TiO₂:Co thin films exhibits an overall lower transmittance value is most likely associated to the presence of the ternary crystalline phase (CoTi₂O₅) found via the X-Ray diffraction measurements, which was not found in the case of **Fig. 3-26a** and **Fig. 3-26b**.

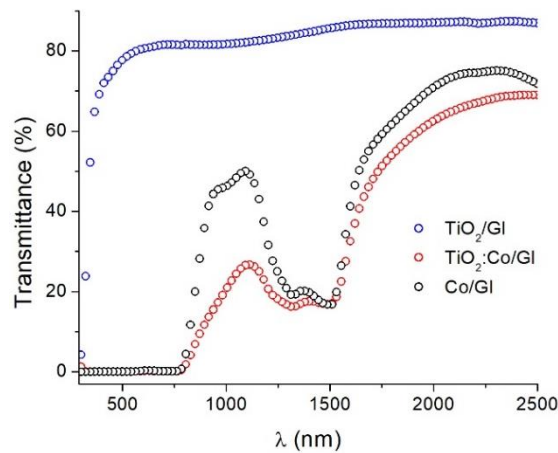


Fig. 3-27: Transmittance spectra of the thin films from Series 1, 2 (30 min.) and 3 annealed after deposition at 600 °C in an air atmosphere.

²⁰ Recalling the previous section, this interference condition was not present in as-deposited samples (Section 3.3.1)

The fact that the formation of a ternary phase not only affects the structural properties of the material, but also its optical properties is an interesting discovery in this work, because the potential applications of the material can now be discriminated depending on the chosen annealing temperature of this type of films. While annealing temperatures below $550\text{ }^{\circ}\text{C}$ produce samples with elevated transmittance (coupled with a lack of bonding between the TiO_2 and Co compounds), the use of a greater annealing temperature bears the generation of a useful intermetallic alloy, but the transparency of the thin films is then compromised.

Evaluating the effect of the deposition time over the optical properties of the $\text{TiO}_2\text{:Co}$ thin films yields the results presented on **Fig. 3-28** and **Fig. 3-29**, the former holds the transmittance plots for the annealing processes carried out at $500\text{ }^{\circ}\text{C}$ and $550\text{ }^{\circ}\text{C}$ whilst the latter concerns the results after annealing at $600\text{ }^{\circ}\text{C}$ in an oven exposed at ambient conditions. Once again an increase in transparency is the most evident result as compared with the as-deposited samples with in-situ annealing²¹; this increase once again is associated with the formation of the cobalt oxide phase and it offers a new scope of potential applications regarding transparent metallic oxide thin films, mostly in the near infrared region.

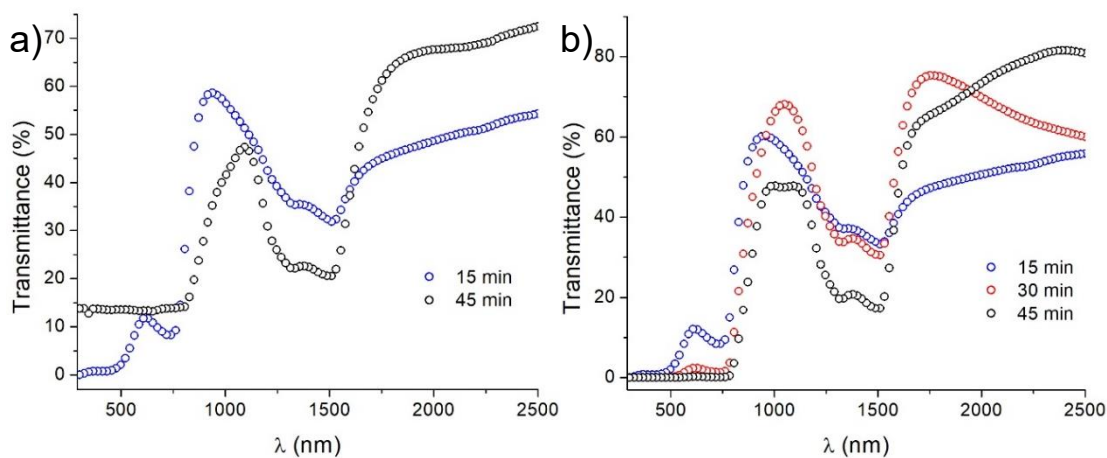


Fig. 3-28: Transmittance spectra of the thin films from Series 2 annealed after deposition at: a) $500\text{ }^{\circ}\text{C}$ and b) $550\text{ }^{\circ}\text{C}$ in an air atmosphere.

²¹ Red curve from **Fig. 3-25**.

As mentioned above, the sudden decrease of transmittance around the 1500 nm mark was associated with the formation of the ternary phase CoTi_2O_5 in the surface of the samples; recalling the X-Ray analysis this phase was only manifested when the material was brought to $600\text{ }^\circ\text{C}$ annealing temperature; in that order, every spectra in **Fig. 3-29** should exhibit a sudden drop in transmittance to values lower than 50%, but the evidence shows that it is not the case for the sample deposited using 15 minutes as deposition time. This fact allows the conclusion and corroboration of the results cited in **Fig. 3-7**, where it was specified that the formation of an intermetallic phase with such a short deposition time was very unlikely.

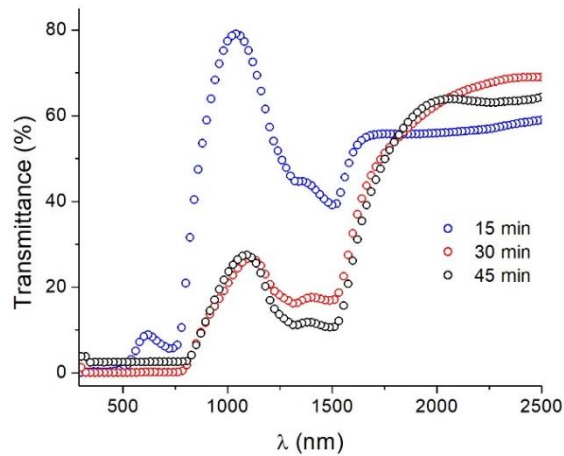


Fig. 3-29: Transmittance spectra of the thin films from Series 2 annealed after deposition at $600\text{ }^\circ\text{C}$ in an air atmosphere.

In addition to this study, it is also worth mentioning the slight “hump” that every cobalt-containing thin film exhibits exactly between 1300 nm and 1500 nm . This phenomenon present in the transmittance spectra is consistent with optically activated intracenter transitions [87] in the cobalt atoms given the fact that its $3d$ shell is unfilled²². The description of said transitions has been a widely studied theoretical line of research, with the Deep Level formalism being the most prominent and successful in understanding the quantum phenomena which a transition metal impurity causes inside a semiconductor, whether it be an oxide, II-VI or III-V-type semiconductor. The presence of this transitions in the impurity atoms are caused by the large magnetic moment of the unfilled $3d$ shells and they are common to almost every quantum structure such as diluted magnetic semiconductors (DMS), one of the

²² Recall that the cobalt electronic configuration is $[\text{Ar}] 3d^7 4s^2$

purposes of the Deep Level theory consist in determining the effect and direct relations that this unfilled level has on the remarkable properties a DMS yields (such as ferromagnetism and semiconductor behavior). A further scrutiny regarding the Depp Level theory and impurity center transitions is set as a perspective for this work given the increasing interest [88] and potential applications of optically active centers inside a semiconductor matrix and DMS research.

Continuing with the optical study, **Fig. 3-30** and **Fig. 3-31** refer to the dependence of the thin film properties when different substrate temperatures were employed in the deposition process (recall **Table 2-1**). Similar interference phenomena are evident from the transmittance spectra in all cases, as well as the intracenter transitions explained above. It is also possible to observe that the behavior of the transmittance is almost identical for the samples annealed at 550 °C and 600 °C, which is an interesting result considering the large difference in substrate temperature.

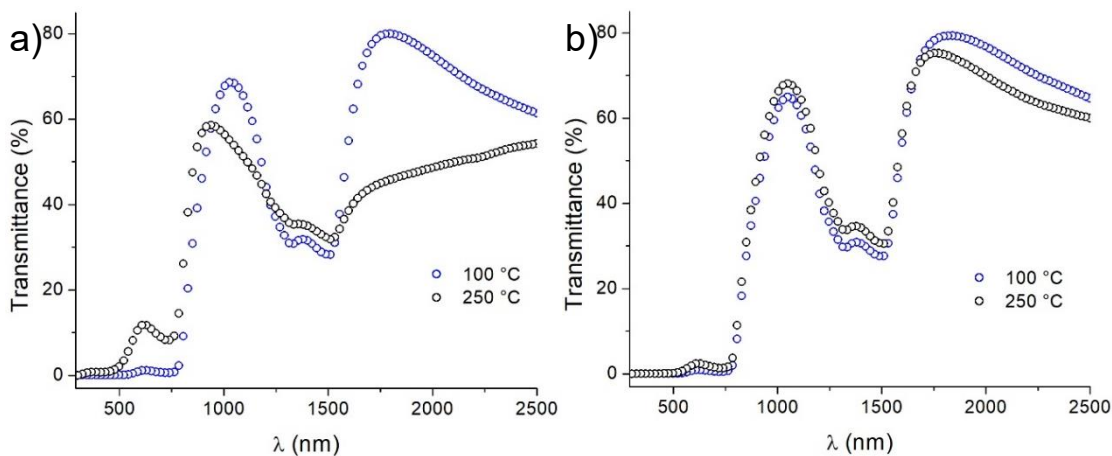


Fig. 3-30: Transmittance spectra of the thin films from Series 4 annealed after deposition at: a) 500 °C and b) 550 °C in an air atmosphere.

The decrease in transmittance for the samples shown in **Fig. 3-31** is quite similar to the one found for **Fig. 3-29**, which as it has been mentioned numerous times above, is directly related to the presence of the ternary intermetallic phase, which this research found to be possible with deposition times greater than 30 minutes and annealing temperatures greater than 600 °C. An interference fringe as well as the intracenter transition phenomena was found also for

the sample deposited with $100\text{ }^{\circ}\text{C}$ T_s which allows to conclude that this temperature already provides the necessary thermal excitation at the surface of the substrate for the compounds to subsequently bond into intermetallic materials. This measurements also granted the fact that the fabricated thin films pertain an optically active impurity, caused by the cobalt atoms which may further increase the scope of applications of the TiO₂:Co intermetallic alloys synthesized.

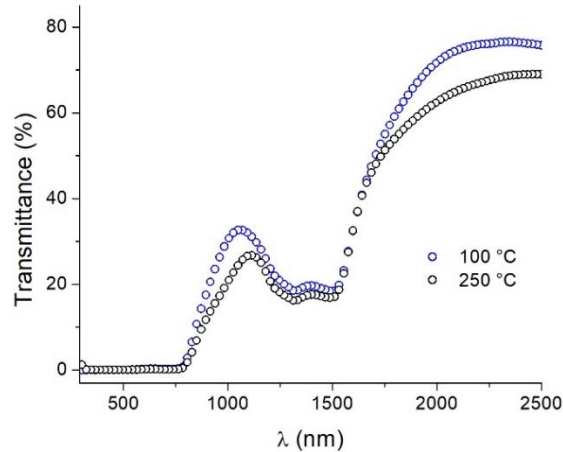


Fig. 3-31: Transmittance spectra of the thin films from Series 4 annealed after deposition at $600\text{ }^{\circ}\text{C}$ in an air atmosphere.

Additional study regarding the optical behavior of the thin films concerned the determination of the optical band gap using the theoretical background of section 1.6, specifically eq. (1.15)²³ which regards the Tauc model for the determination of the gap energy in semiconductor compounds using an absorbance plot. For that purpose, the reflectance spectra of every annealed thin film deposited on glass were measured and then computed with the presented transmittance values to determine the overall absorbance of every thin film fabricated via eq. (1.11)²⁴.

With the value of the absorbance, the absorption coefficient was subject of calculation using the measured thickness of the thin films with the SEM microscope as eq. (1.14) dictates (dividing the absorbance by the thickness times a proportionality constant), and finally the factor $(\alpha h\nu)^{1/2}$ was plotted against the incident photon energy ($h\nu$), just as **Fig. 3-32** shows.

²³ Recalling it: $(\alpha h\nu)^{1/n} = A(h\nu - E_g)$, $n = 2$.

²⁴ $A = 1 - T - R$

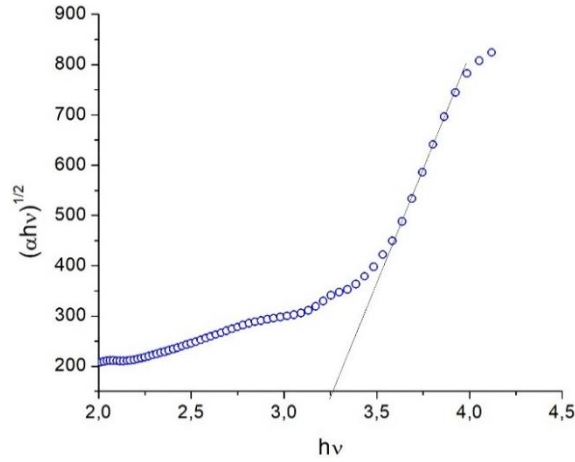


Fig. 3-32: $(\alpha hv)^{1/2}$ vs. (hv) plot for a TiO_2 thin film from series 1 annealed at $600\text{ }^\circ\text{C}$ for 5 hours.

Extrapolation of the linear section of the plot allows the determination of the optical band gap of the sample as $E_g = hv$ (when $(\alpha hv)^{1/2} = 0$), which in this case yields a value of 3.26 eV . Considering the previous example as a guide, the rest of the optical band gaps were obtained and are summarized in **Table 3-1**. Keeping in mind that these results were only calculated in this way for the samples deposited in glass in which both transmittance and reflectance were measured with the UV-Vis-NIR spectrophotometer.

Series	Substrate temperature (T_s)	Annealing temperature (T_A)	Deposition time (t_d)	Gap energy (eV)
Series 1 (TiO_2 thin films)	$250\text{ }^\circ\text{C}$	$450\text{ }^\circ\text{C}$ in-situ	30 min	3.53
		$500\text{ }^\circ\text{C}$		3.45
		$550\text{ }^\circ\text{C}$		3.50
		$600\text{ }^\circ\text{C}$		3.26
Series 2 ($\text{TiO}_2\text{:Co}$ thin films)	$250\text{ }^\circ\text{C}$	$450\text{ }^\circ\text{C}$ in-situ	15min	--
		$500\text{ }^\circ\text{C}$		1.22
		$550\text{ }^\circ\text{C}$		0.90
		$600\text{ }^\circ\text{C}$		1.38
		$450\text{ }^\circ\text{C}$ in-situ	30 min	--
		$550\text{ }^\circ\text{C}$		1.10

		600 °C		--
		450 °C in-situ	45 min	--
		500 °C		0.75
		550 °C		1.22
		600 °C		--
Series 4 (TiO ₂ :Co thin films)	100 °C	450 °C in-situ	30 min	--
		500 °C		1.33
		550 °C		1.18
		600 °C		--

Table 3-1: Gap energies calculates for the TiO₂:Co thin films deposited on glass.

Fig. 3-33 shows an additional two $(\alpha h\nu)^{1/2}$ vs. $(h\nu)$ plots for a couple of samples cited in **Table 3-1**, the evident decrease of the energy band gap is directly related to the use of both targets at the moment of deposition. The extrapolation of the curve shows the determined E_g values.

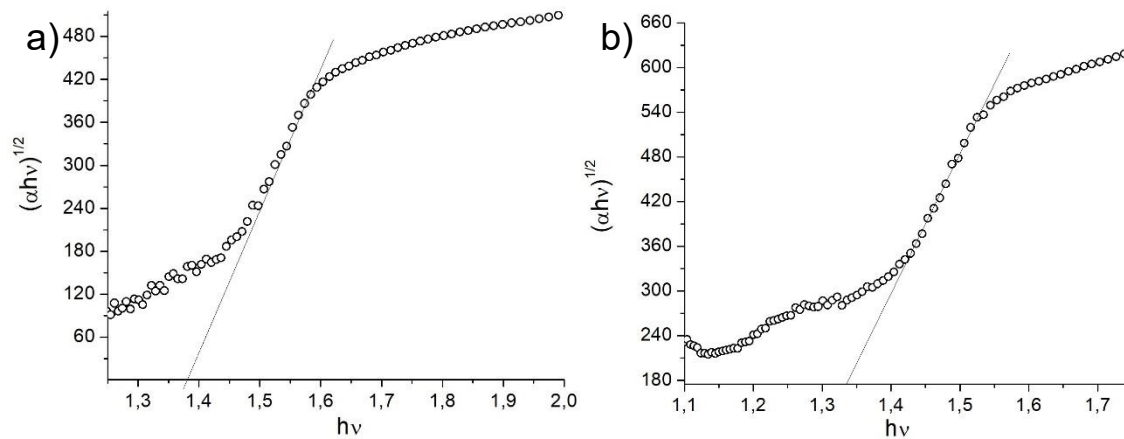


Fig. 3-33: $(\alpha h\nu)^{1/2}$ vs. $(h\nu)$ plot for: a) TiO₂:Co thin film from series 2 (15 min.) annealed at 500 °C and b) TiO₂:Co thin film from series 4 (100 °C) annealed at 500 °C.

This concludes the optical characterization of the thin films. The obtained results granted a great insight into the TiO₂:Co thin film properties, along with its marked variations when using distinct deposition times, substrate temperatures and specially, post-deposition annealing temperatures. The contributions presented here aim towards the objective of further strengthen the material science research discipline and the investigation on spintronic materials and devices for the enhancement of the current commercial equipment.

3.4 Additional characterizations

As it was mentioned before, further measurements from the samples were taken using additional equipment from academic institutions in collaboration with the Physics Department of the Universidad Nacional de Colombia. This section addresses the results obtained from X-Ray Photoelectron Spectroscopy (XPS) measurements taken by the Surface Science Laboratory of the Universidad Industrial de Santander, and also the results gathered from the Physical Properties Measurement System (PPMS) located at the Center for Excellence of New Materials (CENM) in Universidad del Valle. The reported analysis from this particular section appealed to the collaborative spirit of the academic institutions in Colombia, and therefore a special acknowledgment towards these two distinguished laboratories is in order.

3.4.1 XPS measurements

Fig. 3-34 shows the obtained XPS spectrum from a $\text{TiO}_2\text{:Co}$ thin film, the parameters of which are listed in **Table 2-1**, under the ‘Series 2’ row, specifically the sample deposited on glass using a 30 minutes deposition time; in addition, the analyzed sample was subject to annealing after deposition at a temperature of $600\text{ }^\circ\text{C}$ in uncontrolled atmosphere for five hours. The experiments were performed with the surface characterization platform XPS/ISS/UPS-ACenteno built by SPECS (Germany), this platform is provided with a PHOIBOS 150 2D-DLD energy analyzer. In order to obtain the measurements, a monochromatic $\text{Al-K}\alpha$ X-Ray source working at a 200W power was employed. The examined regions for the sample were: C 1S, O 1S, Ti 2p, Ca 2p, Co 2p and Na 1S; at the end of every analysis, the C 1s region was again recorded in order to verify the evolution of the superficial charge during the analysis.

The spectrum was studied using the CASAXPS software (Casa Software Ltd.), employing the SPECS Prodigy-ACenteno library provided with response sensitivity factor values determined by the manufacturer. In this manner, the results regarding the elemental composition and oxidation states derived from the high resolution spectra are found in **Table 3-2**.

Element	Elemental composition (%molar)	Oxidation states
C	50.97	--
O	36.96	O^{-2} ; O^{-3}

Ti	0.08	Ti ⁺⁴
Ca	1.68	Ca ⁺²
Co	7.75	Co ⁺² ; Co ⁺³
Na	2.57	Na ⁺¹

Table 3-2: Elemental composition of a TiO₂:Co thin film measured via XPS data.

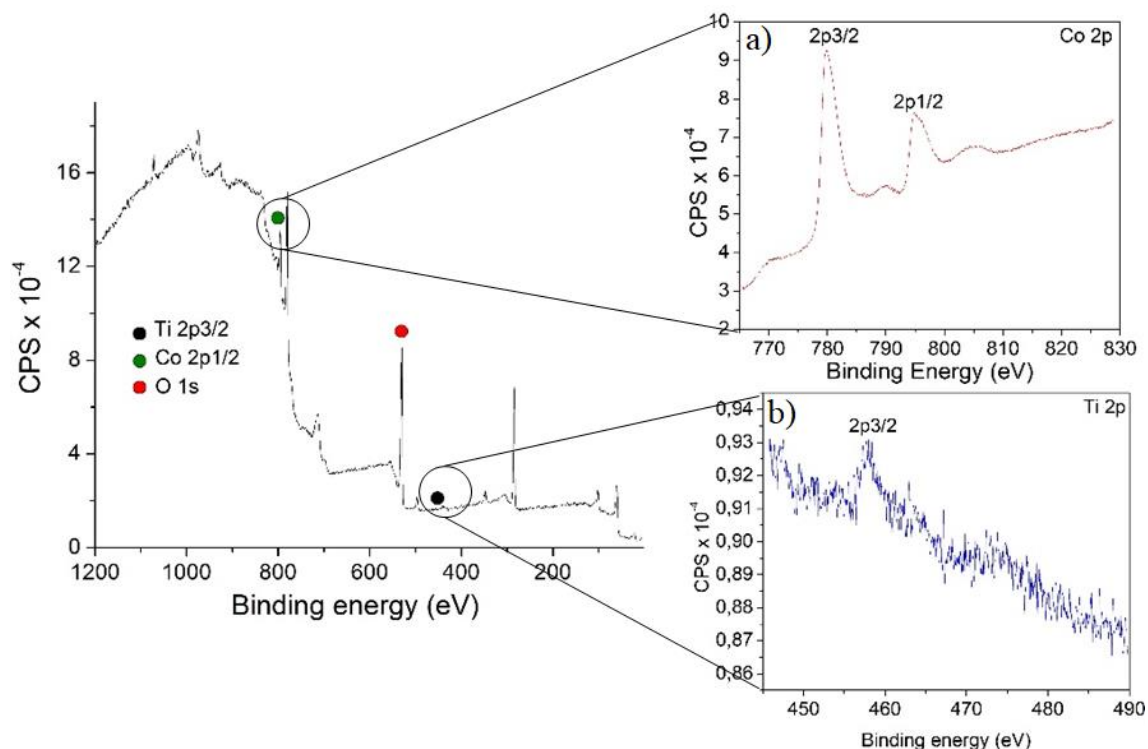


Fig. 3-34: XPS spectra of an annealed TiO₂:Co thin film using a t_d of 30 minutes. Insets a) and b) highlight the Co 2p and Ti 2p peaks of the spectrum, respectively.

As it can be seen from the curve, several peaks were found during the study, these are consistent with elements like carbon, oxygen, calcium, or sodium, however the most relevant energies are highlighted in insets a) and b) where the Co 2p and Ti 2p energies are shown. The peak consistent with Co 2p_{1/2} appeared to be similar in shape with another report from Mutjaba et al [89] which granted the conclusion that this peak was related with the Co₃O₄ compound also found by X-Ray diffraction measurements. Further analysis provided that the energies at which the signal for Co 2p_{3/2} was found were 779.7 eV whilst the energy for the Co 2p_{1/2} peak was located at around 794.6 eV, both of these satellites are consistent with the

Co₃O₄ molecule according to the NIST database [90]. Further reports from Younis et al. [91] and Petitto et al [92] also suggested the existence of the mentioned cobalt species in their respective works, in the same energy intervals as the measured TiO₂:Co thin film exhibited. In addition, according to Greenwood et al. [93], the Co₃O₄ crystalline phase can adopt a spinel-like structure, with the Co⁺² ions located at the tetrahedral interstices and the Co⁺³ ions at the octahedral interstices of the cubic lattice; this particular fact²⁵ is also the reason why the compound is sometimes written as CoO.Co₂O₃ in order to differentiate the two possible locations of the cobalt inside the lattice, along with their different oxidation states. This spinel structure is a type of crystal cubic system that belongs to the spinel group, which in turn are defined as any class of minerals of general formulation $A^{2+}B_2^{3+}O_4^{2-}$, with the cations A and B occupying some or all the octahedral and tetrahedral sites in the lattice, for this particular case, both ions are cobalt atoms with different oxidation states, although in the more general case, said cations are elements of different nature. Each particular cation has the property to be distributed in the lattice depending on its crystal field stabilization energy [94].

For the titanium species found over the sample, the determined oxidation state was +4, which is in agreement with the results obtained from the X-Ray diffractometer, where the CoTi₂O₅ crystalline phase was found, and in order for this molecule to be electrically stable, Ti must have said specific oxidation state (along with a -2 for oxygen and +2 for cobalt oxidation numbers), this result confirms once again the presence of a TiO₂:Co intermetallic alloy formed as thin film over a glass substrate after annealing at 600 °C.

3.4.2 PPMS measurements

The Physical Properties Measurement System located at the Center for Excellence of New Materials has the capacity to measure the magnetic response of materials at different temperatures and different applied magnetic fields. Once again, collaboration between the Universidad Nacional and Universidad del Valle proved to be a fortunate addition to this work. The specific module used for the process was the VSM (Vibrating Sample Magnetometer) configuration, and a total of two studies were performed over the chosen sample. First, the magnetic response of the thin film was studied by applying a magnetic field ranging from -30

²⁵ Along with the properties cited in section 3.1.2 (Samples annealed at 550 °C)

kOe to *30 kOe*, with a magnetic field increase rate of *50 Oe/min* at four different temperatures, namely: *4 K*, *50 K*, *150 K* and *300 K*; this procedure was carried out in order to obtain the behavior of the Magnetization as a function of the applied Magnetic Field (*M vs H*). The second study concerned the dependence of the magnetization in the material with increasing temperature (*M vs. T*), the measured temperature interval ranged from *4K* up to *400K* at a rate of *5 K/min*, applying the Zero Cooled Field (ZFC) configuration, which meant that the sample was brought to the desired temperature in the absence of a magnetic field, i.e. $H = 0 \text{ Oe}$.

The sequence for the *M vs H* testing of the TiO₂:Co thin film consisted initially on de-magnetizing the material in order to “dis-align” any magnetic moments on the sample, then the initial temperature of *4K* was reached by cooling the system at a rate of *5K/min*, subsequently the measurements for magnetization were automatically recorded from *-30 kOe* to *30 kOe*, increasing the applied magnetic field *50 Oe* every minute. This particular value had to be specifically chosen for this sample due to the fact that it exhibited a quick saturation if the field was increased at a greater rate and therefore an evaluation of the region near *0 Oe* would not have been possible. The measurements for the remaining temperatures were performed following the previously mentioned steps.

For the *M vs. T* testing, the system was first brought to ambient temperature (*300 K*) and again, a de-magnetization of the sample was made. Then the initial measurement temperature (*4 K*) was reached cooling the system at a rate of *5 K/min*, and finally the data was collected increasing the temperature until *400 K* with the same rate as before. The data recording process was carried out automatically.

In this manner, **Fig. 3-35** shows the curves of the magnetic moment as a function of the applied magnetic field when the samples were subject to temperatures of *4 K* and *50 K*, each inset of the figure shows the region near the coercive field value; at first glance, both curves seem to obey a superparamagnetic (SPM) behavior, exhibiting limited coercive fields of *239 Oe* and *307 Oe* for the *4 K* and *50 K* measurement, respectively. Similarly, the remnant magnetization is close to zero in both cases (*0.0021 emu* for the *4 K* test and *0.0023 emu* for the *50 K* test), which further supports the SPM condition of the as-deposited thin film, it is important to recall that the sample analyzed was not subject to post-deposition annealing and therefore is very unlikely for it to contain any cobalt oxide or cobalt titanate phases, in fact the only crystalline

phase present in this sample is the pure cobalt phase (Section 3.1.1). Additionally, it can be observed that both curves lack a specific saturation value for the magnetization, which is less pronounced on the 50 K test, this type of behavior outside the coercive field region is most commonly associated with a paramagnetic, or even antiferromagnetic material, therefore a possible overlapping of two distinct magnetic phases is applicable for the $\text{TiO}_2\text{:Co}$ thin film at this temperatures. Superparamagnetic materials currently play a big role in numerous areas of science and technology, among the most interesting applications this type of material yields are: Its use as a ferrofluid for liquid seals, efficient heat transfer and damping [95], evidently the latter case is not applicable for this work, therefore the direct potential use of the fabricated thin films would be oriented towards the information storage field.

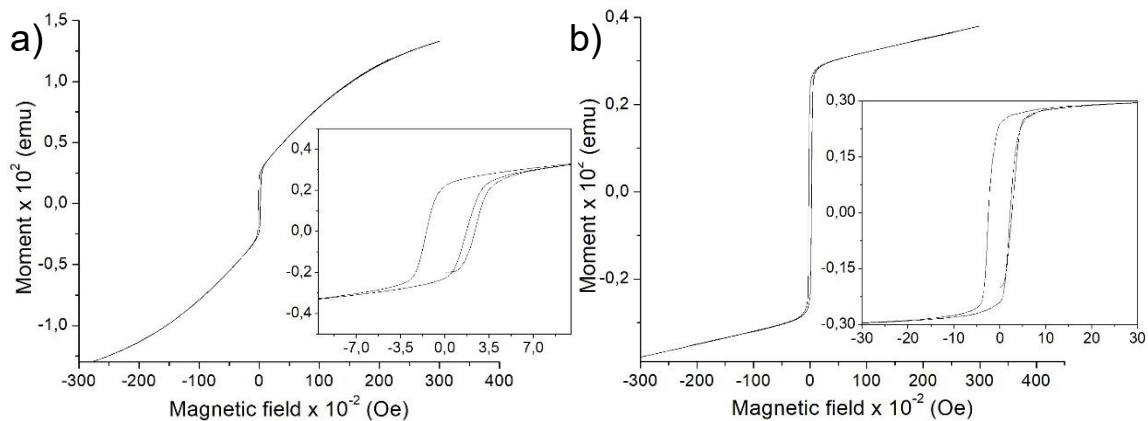


Fig. 3-35: PPMS measurement of an as-deposited $\text{TiO}_2\text{:Co}$ thin film from Series 2, using a t_d of 30 minutes, the data was collected at a sample temperature of a) 4 K and b) 50 K .

Fig. 3-36, on the other hand, shows the M vs. H test for the same sample at two additional temperatures, namely 150 K and 300 K (the latter is close to ambient temperature, both insets once again show the region around $H = 0\text{ Oe}$). As it can be seen from the curves, the samples saturated very quickly with small applied magnetic fields, a behavior that is more prominent than in the previous study. In this manner, coercive fields close to zero in both cases were obtained (123 Oe for 150 K and 0 Oe for 300 K) and a saturation magnetization of 0.0025 emu in **Fig. 3-36a** was determined. On the other hand, the tendency of the curve for the test at 300 K indicates a different type of magnetic behavior for the thin films, typically consistent with diamagnetism, even though the sample exhibits a saturation magnetization of 0.0027 emu in **Fig. 3-36b**, the decreasing nature of the magnetic moment with increasing H indicates that at

said temperature the material tends to exclude the magnetic lines of force, which is a not so convenient property when it comes to the information storage matter.

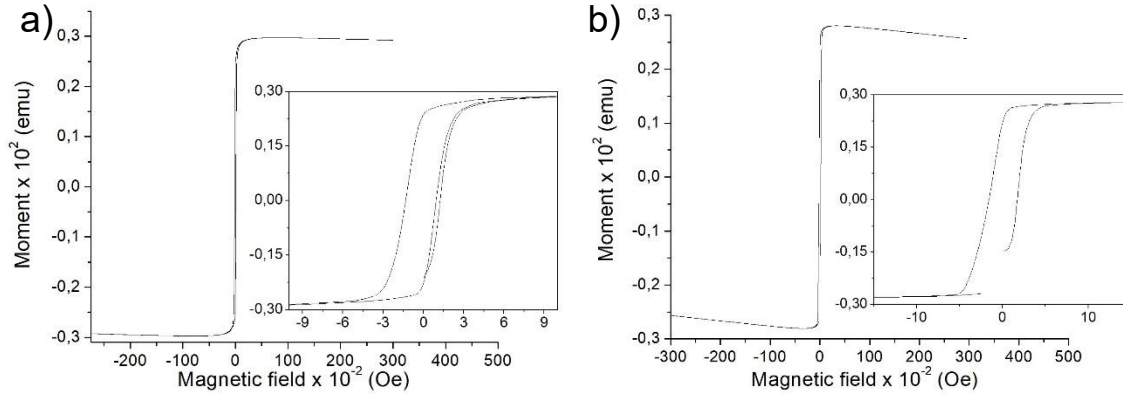


Fig. 3-36: PPMS measurement of an as-deposited TiO₂:Co thin film from Series 2, using a t_d of 30 minutes, the data was collected at a sample temperature of a) 150 K and b) 300 K.

A superparamagnet is a material made of small single-domain non-interacting magnetic grains dispersed in some non-magnetic medium [95], a typical value of the diameter of said grains is around 10 nm; its potential usage in hard disk drives concerns the replacing of the platters where the information (bits) are stored in order to enhance the recording capabilities of conventional hard disk drives given that the grains are sufficiently small and inform in size as possible.

The previous study granted some feedback towards improving the magnetic properties of the compound for it to become a ferromagnetic material and later be applied in spintronic materials development, which is a main research area in the Group of Nanostructured Materials and their Applications. In this case what is desired is for the thin films to exhibit a considerable remnant magnetization and a wider hysteresis loop than the ones found for the TiO₂:Co samples. Perhaps a different handling of the deposition technique and synthesis parameters may hold results more affiliated with the ferromagnetism, especially at temperatures close to the ambient conditions, this further study is set as a perspective for this work.

4. Conclusions and perspectives

4.1 Conclusions

- ✓ TiO₂:Co intermetallic alloy thin films were successfully fabricated via de DC Magnetron co-sputtering method using a cobalt and reduced titanium dioxide targets varying the synthesis parameters like deposition time, substrate temperature and substrate employed (titanium foil, soda-lime glass and silicon wafer). The resulting thin films were of opaque nature which was subsequently damped after the samples were subject to annealing processes in an uncontrolled atmosphere.
- ✓ Structural characterization revealed a limited crystallization of the as-deposited samples, with only the samples containing cobalt exhibiting diffraction peaks consistent with a cobalt phase. The sputtering of TiO₂ in this technique contributes to a decreasing in crystallinity of the samples, to a point where thin films made exclusively of titanium dioxide presented a completely amorphous behavior.
- ✓ Post-deposition annealing of the thin films deposited on soda-lime glass severely increased their crystallinity, only in the samples containing cobalt which was evident in an increase of diffraction peaks in the diffractograms. The resulting crystalline phases were a cobalt oxide phase (Co₃O₄) for the lower annealing temperatures (500 °C and 550 °C) and a ternary cobalt titanate phase (CoTi₂O₅) for the highest annealing process (done at 600 °C). This intermetallic alloy had not been obtained up until now using this deposition technique.
- ✓ Morphological characterization revealed mostly a granular nature of the surface in the thin films deposited in glass, and a platelet-like formation on the other two substrates. The grains in the surface increased in size from approximately 50 nm up to 110 nm after the annealing processes were performed, HR-SEM granted that the average thickness of the thin films was 100nm, which meant that the fabricated samples lie on the ultra-thin film regime. AFM measurements revealed a decrease in root mean

square roughness from *16.73 nm* to *15.68 nm* after the samples were annealed at *600 °C*.

- ✓ Optical characterization of the thin films revealed a greatly reflective nature for the as-deposited samples containing cobalt, accompanied by an overall low transmittance for the same material. The thin films made exclusively of TiO₂ exhibited a prominent transmittance along the evaluated spectra, with a sudden decrease near UV wavelengths, which are consistent with the nature of the material given its gap energy of approximately *3.0 eV* and concordant absorption of radiation at said wavelengths.
- ✓ Post-deposition annealing processes on the samples deposited in glass resulted in a severe increase of transparency, especially in the infrared region, along with the presence of interference fringes and intracenter transitions of the cobalt atoms, which were evident given their unfilled 3d shells. The complementary reflectance measurements allowed the calculation of the gap energies of the samples deposited in glass.
- ✓ Magnetic measurements in a PPMS revealed a superparamagnetic behavior of the annealed thin films, reaching a maximum saturation of *0.0027 emu*. The magnetic response became of diamagnetic nature once the tests were performed at temperatures close to *25 °C* which granted insight regarding the potential application or limitations of the fabricated thin films at different temperatures.
- ✓ X-ray photoelectron spectroscopy further corroborated the presence of an intermetallic alloy in the annealed samples, and also granted a low molar concentration for titanium, a phenomenon that was associated to the limited penetration length of the X-ray beam. Structural properties on the cobalt oxide phase were also studied with this technique, revealing a spinel like structure for the Co₃O₄ compound, in which the cobalt ions with oxidation state +2 are located in the tetrahedral interstices and ions with oxidation state +3 are located in the octahedral interstices.

4.2 Perspectives

Given the fact that material science is an ever growing field of research, several additional work can be done in order to further complement or extend the scope of the research here presented. In this manner, some perspectives from this work look towards the better

understanding of employing this deposition technique in the synthesis of ternary metallic oxide phases in which a semiconductor target is employed as main precursor; this is because up until now the DC magnetron co-sputtering had not been used to deposit this type of materials.

Subsequently, the performance of the fabricated thin films in spintronic devices remains to be fully determined and studied, seeing as it is not only one of the main lines of research at the Group of Nanostructured Materials and their Applications, but also a widely explored and demanded area of investigation given the possible advancement these devices imply for engineering.

Additional study regarding the consequences of intracenter transitions inside the matrix of the $\text{TiO}_2\text{:Co}$ thin films, as well as the further enhancement of their magnetic properties close to ambient temperature would also further the scope of this work because spintronic devices generally require materials which do not exhibit diamagnetism if a potential application at ambient temperature is pursued.

Annex A: Scientific products of this work

Part of this research was accepted for presentation as an oral work in the international conference on Advanced Energy Materials (AEM 2017) which took place between the 11th and 13th of September 2017 in the University of Surrey, Guildford, United Kingdom. The submitted abstract was identified as “Abstract ID 33- Growth and crystallization of Cobalt-doped TiO₂ alloys: Effect of substrate and annealing temperature” and it was later accepted for publication in the journal Applied Surface Science [69].



ARTICLE IN PRESS

Applied Surface Science xxx (2018) xxx–xxx



Contents lists available at ScienceDirect

Applied Surface Science

journal homepage: www.elsevier.com/locate/apsusc



Full Length Article

Growth and crystallization of Cobalt-doped TiO₂ alloys: Effect of substrate and annealing temperature

Andrés J. Bohórquez*, Heiddy P. Quiroz, A. Dussan

Universidad Nacional de Colombia – Bogotá, Dpta. de Física, Grupo de Materiales Nanoestructurados y sus Aplicaciones, Cra. 30 No. 45-03 Edificio 404 Lab. 121C Ciudad Universitaria, Bogotá 11001, Colombia

ARTICLE INFO

Article history:

Received 11 November 2017

Revised 18 April 2018

Accepted 19 April 2018

Available online xxxxx

Keywords:

Sputtering

Alloys

Crystalline phases

TiO₂

ABSTRACT

This work presents a study of the structural and optical properties of cobalt-doped titanium dioxide thin films prepared via the DC Magnetron Co-Sputtering technique using TiO₂ and Co targets with 99.99% purity; these thin films were deposited on three different substrates: Soda-lime glass, titanium foil and silicon wafer. The resulting films deposited on glass were then submitted to annealing processes at temperatures ranging from 500 °C to 600 °C. X-ray diffraction measurements revealed limited crystallization of the as-deposited samples, whilst the annealed samples showed several crystalline phases, including cobalt oxide (Co₃O₄) and a ternary phase (CoTi₃O₇); SEM studies helped to corroborate that the inclusion of TiO₂ into the thin film decreases its crystallinity, obtaining nanostructures smaller in size as compared with samples containing cobalt. UV-vis-NIR measurements revealed an increase in transparency of the thin films after annealing at 600 °C, evidencing extrinsic absorption phenomena, consistent with the formation of binary phases inside the semiconductor matrix. From XPS measurements, the oxidation states for Co and Ti were obtained.

© 2018 Elsevier B.V. All rights reserved.

1. Introduction

Titanium and its alloys have been the center of attention for several applications in recent years such as: aerospace [1], biomedics [2], auto motor devices [2], mechanics [2], chemicals [3,4], among others [5,6]. Their excellent physical, chemical and mechanical properties can vary depending on the element incorporated: Manganese (Mn), Nickel (Ni), Aluminum (Al), Cobalt (Co), Iron (Fe), etc.; these additives stabilize the alloys formation and are also precursors for the formation of intermetallic compounds [7]. If a non-metallic element is incorporated (for example oxygen), the formation of binary or ternary crystalline phases are favored, which will be evident from the internal oxidation of the compound during synthesis [8].

Interaction between Ti and O can occur even at room temperature, forming oxides such as α-TiO or TiO₂ [8]. However, the TiO₂ phase is the most stable of α-titanium alloys; the incorporation of the Co element will depend on the internal oxidation and thermodynamic structure of these alloys.

In this work, we present the synthesis and characterization of Cobalt-doped TiO₂ alloys useful in spintronic applications [9].

These nanostructured thin films were prepared by the DC magnetron co-sputtering method and characterized structural, compositional and optically in order to understand the dependence of film growth and physical properties with the synthesis parameters. Titanium oxide, cobalt oxide and cobalt titanate (CoTiO₃) crystalline phases were identified using the X-ray diffraction technique. Post-deposition annealing generates the formation of metallic oxide phases as well as affects the optical properties of the thin films.

2. Materials and methods

2.1. Experimental details

Cobalt-doped TiO₂ alloys were fabricated in an argon gas environment (99.999% pure) using the DC Magnetron Co-Sputtering configuration. The magnetron powers employed were 120 W for the TiO₂ target (99.99% pure) and 70 W for Co (99.99% pure), the work pressure used was fixed at 2.5 × 10⁻² Torr and the substrate temperature was established at 250 °C. In-situ annealing was performed at 450 °C for 3 h for all samples. The thin films were deposited on soda-lime glass (previously cleaned), titanium foil (50 μm thick and 99.96% pure) and silicon wafer ((1 0 0) plane and 0–10 0 Ω·cm resistivity) substrates. This was done in order to examine

* Corresponding author.

E-mail address: ajbohórquez@unal.edu.co (A.J. Bohórquez).

<https://doi.org/10.1016/j.apsusc.2018.04.177>

0169-4332/© 2018 Elsevier B.V. All rights reserved.

Please cite this article in press as: A.J. Bohórquez et al., Growth and crystallization of Cobalt-doped TiO₂ alloys: Effect of substrate and annealing temperature, Appl. Surf. Sci. (2018), <https://doi.org/10.1016/j.apsusc.2018.04.177>

References

- [1] J. T. Hui Tsai, J. Peng, K. Chu y J. Shiung Cheng, «Performances improvement of vacuum tubes using carbon nanotubes embedded cathodes,» *Vacuum*, vol. 145, pp. 1-3, 2017.
- [2] Wikipedia, "Titanium dioxide," [Online]. Available: https://en.wikipedia.org/wiki/Titanium_dioxide. [Accessed 01 February 2018].
- [3] A. Fujishima y K. Honda, «Electrochemical photolysis of water at a semiconductor electrode,» *Nature*, vol. 238, pp. 37-38, 1972.
- [4] H. Gerishcer y H. Tribusch, «Elektrochemische Untersuchungen zur spektralen Sensibilisierung von ZnO-Einkristallen,» *Berich. Bunsen. Gesell.*, vol. 72, pp. 437-445, 1968.
- [5] M. Dare-Edwards, J. Goodenough, A. Hamnett, K. R. Seddon y R. D. Wright, «Sensitisation of semiconducting electrodes with ruthenium-based Dyes,» *Faraday Discuss. Chem. Soc.*, vol. 70, pp. 285-298, 1980.
- [6] B. O'Reagan y M. Grätzel, «A low-cost, high-efficiency solar cell based on dye-sensitized colloidal TiO₂ films,» *Nature*, vol. 353, pp. 737-740, 1991.
- [7] U. Diebold, «The surface science of titanium dioxide,» *Surf. Sci. Rep.*, vol. 48, pp. 53-229, 2003.
- [8] H. P. Quiroz y A. Dussan, «Synthesis of self-organized TiO₂ nanotube arrays: Microstructural, stereoscopic, and topographic studies,» *J. Appl. Phys.*, vol. 120, p. 051703, 2016.
- [9] A. M. More, T. P. Gujar, J. L. Gunjekar, C. D. Lokhande y O. S. Joo, «Growth of TiO₂ nanorods by chemical bath deposition method,» *Appl. Surf. Sci.*, vol. 255, pp. 2682-2687, 2008.
- [10] A. Bohórquez, H. P. Quiroz y A. Dussan, «Propiedades Estructurales y Ópticas de Nanoestructuras de TiO₂ Depositadas por el Método de Deposición en Baño Químico para Aplicaciones en Sensores UV,» *Inf. Tecnol.*, vol. 27, nº 6, pp. 185-192, 2016.
- [11] M. Wang, Q. Li, H. Yu, S. H. Hur y E. Jung, «Phase-controlled preparation of TiO₂ films and micro(nano)spheres by low-temperature chemical bath deposition,» *Alloy. Compd.*, vol. 578, pp. 419-424, 2013.
- [12] R. Asahi, T. Morikawa, T. Ohwaki, K. Aoki y Y. Taga, «Visible-light photocatalysis in nitrogen-doped titanium oxides,» *Science*, vol. 293, pp. 267-271, 2001.

- [13] P. Roy, S. Berger y P. Schmuki, «TiO₂ Nanotubes: Synthesis and Applications,» *Angew. Chem. Int.*, vol. 50, pp. 2904-2939, 2011.
- [14] M. A. Henderson, S. Otero-Tapia y M. E. Castro, «The chemistry of methanol on the TiO₂(110) surface: the influence of vacancies and coadsorbed species,» *Faraday Discuss*, vol. 114, pp. 313-329, 1999.
- [15] J. Biener, J. Wang y R. J. Madix, «Direct observation of the growth of vanadium on TiO₂(110)-(1x2),» *Surf. Sci.*, vol. 442, pp. 47-54, 1999.
- [16] J. Sambrano, J. Andres, A. Beltran, F. Sensato, E. Leite, F. Stamato y E. Longo, «An ab initio study of oxygen vacancies and doping process of Nb and Cr atoms on TiO₂(110) surface models,» *Int. J. Quantum. Chem.*, vol. 65, pp. 625-631, 1997.
- [17] U. Diebold y N. D. Shinn, «Adsorption and thermal stability of Mn on TiO₂(110): 2p X-ray absorption spectroscopy and soft X-ray photoemission,» *Surf. Sci.*, vol. 343, pp. 53-60, 1995.
- [18] U. Diebold, H. S. Tao, N. D. Shinn y T. E. Madey, «Electronic structure of ultrathin Fe films on TiO₂(110) studied with soft-x-ray photoelectron spectroscopy and resonant photoemission,» *Phys. Rev. B Condens. Matter.*, vol. 50, n^o 19, pp. 14474-14480, 1994.
- [19] Y. Shao, W. Chen, E. Wold y J. Pau, «Dispersion and electronic structure of titania-supported cobalt and cobalt oxide,» *Langmuir*, vol. 10, n^o 1, pp. 178-187, 1994.
- [20] C. C. Kao, S. C. Tsai, M. K. Bahl y Y. W. Chijng, «Electronic properties, structure and temperature-dependent composition of nickel deposited on rutile titanium dioxide (110) surfaces,» *Surf. Sci.*, vol. 95, pp. 1-14, 1980.
- [21] G. Charlton, P. Howes, C. Muryn, H. Raza, N. Jones, J. Taylor, C. Norris, R. McGrath, D. Norman, T. Turner y G. Thornton, «Copper interface induced relaxation of TiO₂(110)-1x1,» *Phys. Rev. B*, vol. 61, n^o 23, p. 16117, 2000.
- [22] S. Petigny, B. Domenichini, H. Mostefa-Sba, E. Lesniewska, A. Steinbrunn y S. Bourgeois, «Molybdenum deposition on TiO₂(110) surfaces with different stoichiometries,» *Appl. Surf. Sci.*, vol. 142, n^o 1-4, pp. 114-119, 1999.
- [23] G. A. Rizzi, A. Magrin y G. Granozzi, «Preparation of epitaxial ultrathin RuO₂-TiO₂(110) films by decomposition of Ru₃(CO)₁₂,» *Surf. Sci.*, vol. 443, pp. 277-286, 1999.
- [24] A. Berk, G. Ménesi y F. Solymosi, «STM study of rhodium deposition on the TiO₂(110)-(1 x 2) surface,» *Surf. Sci.*, vol. 372, n^o 1-3, pp. 202-210, 1997.
- [25] C. Xu, X. Lai, G. W. Zajac y D. W. Goodman, «Scanning tunneling microscopy studies of the TiO₂(110) surface: Structure and the nucleation growth of Pd,» *Phys. Rev. B*, vol. 56, n^o 20, p. 13464, 1997.
- [26] W. T. Wallace, B. K. Min y D. W. Goodman, «The nucleation, growth, and stability of oxide-supported metal clusters,» *Top. Catal.*, vol. 34, n^o 1-4, pp. 17-30, 2005.
- [27] V. N. Ageev y S. M. Sololev, «Investigation of lithium adsorption on the surface of TiO₂ by electron-stimulated desorption,» *Surf. Sci.*, vol. 480, pp. 1-10, 2001.

- [28] P. W. Murray, N. G. Condon y G. Thornton, «Na adsorption sites on TiO₂(110)-1 × 2 and its 2 × 2 superlattice,» *Surf. Sci.*, vol. 323, pp. L281-L286, 1995.
- [29] M. A. San Miguel, C. J. Calzado y J. F. Sanz, «Modeling Alkali Atoms Deposition on TiO₂(110) Surface,» *J. Phys. Chem. B*, vol. 105, nº 9, pp. 1794-1798, 2001.
- [30] R. Souda, W. Hayami, T. Aizawa y Y. Ishizawa, «Chemical analysis of alkali-metal adatoms using low-energy D⁺ scattering,» *Phys. Rev. B*, vol. 48, p. 17255, 1993.
- [31] L. S. Dake y R. J. Lad, «Electronic and chemical interactions at aluminum/TiO₂(110) interfaces,» *Surf. Sci.*, vol. 289, pp. 297-306, 1993.
- [32] A. Berkó, G. Klivényi y F. Solymosi, «Fabrication of Ir/TiO₂(110) Planar Catalysts with Tailored Particle Size and Distribution,» *J. Catal.*, vol. 182, pp. 511-514, 1999.
- [33] Y. Gao, Y. Liang y S. A. Chambers, «Thermal stability and the role of oxygen vacancy defects in strong metal support interaction — Pt on Nb-doped TiO₂(100),» *Surf. Sci.*, vol. 365, pp. 638-648, 1996.
- [34] A. Kolmakov y D. W. Goodman, «Imaging gold clusters on TiO₂(110) at elevated pressures and temperatures,» *Catal. Lett.*, vol. 70, pp. 93-97, 2000.
- [35] Y. Matsumoto, M. Murakami, T. Shono, T. Hasegawa, T. Fukumura, M. Kawasaki, P. Ahmet, T. Chikyow, S. Koshihara y H. Koinuma, «Room-temperature ferromagnetism in transparent transition metal-doped titanium dioxide,» *Science*, vol. 291, pp. 854-856, 2001.
- [36] S. Chambers, S. Thevuthasan, R. Farrow, F. Marks, J. Thiele, L. Folks, M. Samant, A. Kellock, N. Ruzycki, D. Ederer y U. Diebold, «Epitaxial growth and properties of ferromagnetic co-doped TiO₂ anatase,» *Appl. Phys. Lett.*, vol. 79, p. 3467, 2001.
- [37] G. Sadanandam, K. Lalitha, V. D. Kumari, M. V. Shankar y M. Subrahmanyam, «Cobalt doped TiO₂: A stable and efficient photocatalyst for continuous hydrogen production from glycerol: Water mixtures under solar light irradiation,» *Int. J. Hydrogen Energ.*, vol. 38, pp. 9655-9664, 2013.
- [38] W. T. Geng y K. S. Kim, «Interplay of local structure and magnetism in Co-doped TiO₂ anatase,» *Solid State Commun.*, vol. 129, pp. 741-746, 2004.
- [39] C. Huang, Y. Guo, X. Liu y Y. Wang, «Structural and optical properties of Ti_{1-x}CoxO₂ films prepared by sol-gel spin coating,» *Thin Solid Films*, vol. 505, pp. 141-144, 2006.
- [40] Alamgir, W. Khan, S. Ahmad y A. H. Naqvi, «Formation of self-assembled spherical-flower like nanostructures of cobalt doped anatase TiO₂ and its optical band-gap,» *Mater. Lett.*, vol. 133, pp. 28-31, 2014.
- [41] S. H. Kim y S. Y. Choi, «Fabrication of Cu-coated TiO₂ nanotubes and enhanced electrochemical performance of lithium ion batteries,» *J. Electroanal. Chem.*, vol. 744, pp. 45-52, 2015.
- [42] M. Crisan, M. Raileanu, N. Dragan, D. Crisan, A. Ianculescu, I. Nitoi, P. Oancea, S. Somanescu, N. Stanica, B. Vasile y C. Stan, «Sol-gel iron-doped TiO₂ nanopowders with photocatalytic activity,» *Appl. Catal. A-GEN*, vol. 504, pp. 130-142, 2015.

-
- [43] A. Bouaine, G. Schmerber, D. Ihiwakrim y A. Derory, «Structural, optical, and magnetic properties of polycrystalline Co-doped TiO₂ synthesized by solid-state method,» *Mat. Sci. Eng. B-Solid.*, vol. 177, pp. 1618-1622, 2012.
- [44] S. Rout, N. Popovici, S. Dalui, M. Paramês, R. da Silva, A. Silvestre y O. Conde, «Phase growth control in low temperature PLD Co: TiO₂ films by pressure,» *Curr. Appl. Phys.*, vol. 13, pp. 670-676, 2013.
- [45] A. P. Savio, J. Fletcher y F. C. Robles Hernández, «Sonosynthesis of nanostructured TiO₂ doped with transition metals having variable bandgap,» *Ceram. Int.*, vol. 39, pp. 2753-2765, 2013.
- [46] S. A. Speakman, *Profile Fitting for Analysis of XRPD Data using HighScore Plus*, Massachusetts.
- [47] R. A. Young, «Introduction to the Rietveld method,» de *The Rietveld method*, Oxford, Oxford University Press, 2002, pp. 1-7.
- [48] Y. T. Prabhu, K. V. Rao, V. S. Kumar y B. S. Kumari, «X-Ray Analysis by Williamson-Hall and Size-Strain Plot Methods of ZnO Nanoparticles with Fuel Variation,» *WJNSE*, vol. 4, pp. 21-28, 2014.
- [49] J. Szymonska, M. Targosz-Korecka y F. Krok, «Characterization of starch nanoparticles,» *J. Phys.: Conf. Ser.*, vol. 146, p. 012027, 2009.
- [50] M. Raposo, Q. Ferreira y P. A. Ribeiro, «A Guide for Atomic Force Microscopy Analysis of Soft-Condensed Matter,» de *Modern Research and Educational Topics in Microscopy*, Formatex, 2007, pp. 758-769.
- [51] M. Fox, «Classification of optical processes,» de *Optical properties of solids*, Oxford, Oxford University Press, 2007, pp. 1-2.
- [52] M. Fox, «Optical coefficients,» de *Optical properties of solids*, Oxford, Oxford University Press, 2007, pp. 2-5.
- [53] J. Tauc, R. Grigorovici y A. Vancu, «Optical properties and electronic structure of amorphous germanium,» *Phys. Status Solidi*, vol. 15, pp. 627-637, 1966.
- [54] E. A. Davis y N. F. Mott, «Conduction in non-crystalline systems V: Conductivity, optical absorption and photoconductivity in amorphous semiconductors,» *Philos. Mag.*, vol. 22, p. 903, 1970.
- [55] N. F. Mott y E. A. Davis, «Electronic processes in Non-crystalline Materials,» New York, Clarendon Press, 1979.
- [56] Wikipedia, «Cobalt,» [En línea]. Available: <https://en.wikipedia.org/wiki/Cobalt>. [Último acceso: 02 February 2018].
- [57] thetuzaro, «Física del Estado Sólido y Física de Semiconductores: lo que hay que saber,» 2012. [En línea]. Available: <https://thetuzaro.wordpress.com/tag/diagrama-de-bandas/>. [Último acceso: 01 February 2018].

- [58] R. N. Blumenthal, J. Baukus y W. M. Hirthe, «Studies of the Defect Structure of Nonstoichiometric Rutile, $\text{TiO}_2 - x$,» *J. Electrochem. Soc.*, vol. 114, nº 2, pp. 172-176, 1967.
- [59] J. M. Albella y J. M. Martínez-Duarte, «Distribución de energía de los portadores,» de *Fundamentos de electrónica física y microelectrónica*, Madrid, Addison-Wesley, pp. 31-38.
- [60] V. Pardo, Formación de nanoestructuras de silicio por evaporación térmica y pulverización catódica, Barcelona, 2012.
- [61] S. Swann, «Magnetron sputtering,» *Phys. Technol.*, vol. 19, pp. 67-75, 1988.
- [62] «Sputtering,» [En línea]. Available: http://users.wfu.edu/ucerkb/Nan242/L07-Sputtering_a.pdf. [Último acceso: 01 February 2018].
- [63] S. Schiller, U. Heisig y K. Goedicke, «The role of plasmatron/magnetron systems in physical vapor deposition techniques,» *Thin Solid Films*, vol. 54, nº 1, pp. 33-47, 1978.
- [64] G. Han, Y. Wu, M. Tay, K. Li, Z. Guo y T. Chong, «Epitaxial growth of ferromagnetic Co:TiO₂ thin films by co-sputtering,» *J. Magn. Magn. Mater.*, vol. 268, pp. 159-164, 2004.
- [65] D. A. Skoog, F. J. Holler y S. R. Crouch, «Componentes de los instrumentos,» de *Principios de Análisis Instrumental*, Cengage Learning, 2008, pp. 310-317.
- [66] M. Rodríguez-Gallego, de *La difracción de rayos-X*, Madrid, Alhambra, 1982, pp. 72-130.
- [67] A. Martínez, «La mecánica cuántica,» [En línea]. Available: <http://la-mecanica-cuantica.blogspot.com.co/2009/08/la-espectroscopia-de-rayos-x.html>. [Último acceso: 01 February 2018].
- [68] M. Saleem, L. Fang, A. Wakeel, M. Rashad y C. Y. Kong, «Simple Preparation and Characterization of Nano-Crystalline Zinc Oxide Thin Films by Sol-Gel Method on Glass Substrate,» *WJCMF*, vol. 2, nº 1, pp. 10-15, 2012.
- [69] A. J. Bohórquez, H. P. Quiroz y A. Dussan, «Growth and crystallization of Cobalt-doped TiO₂ alloys: Effect of substrate and annealing temperature,» *Appl. Surf. Sci.*, p. doi: <https://doi.org/10.1016/j.apsusc.2018.04.177>, 2018.
- [70] L. V. Azaroff y M. J. Buerge, «Elementary x-ray diffraction theory,» de *The Powder Method in X-Ray Crystallography*, McGraw-Hill, 1958, pp. 5-11.
- [71] J. Renau-Piqueras y M. Faura, «Principios básicos del microscopio electrónico de barrido,» de *Técnicas de microscopía, micromanipulación y análisis de imagen*, Coruña, Universidad de Coruña, Servicio de Publicaciones, 1994, pp. 73-92.
- [72] U. d. Alicante, «Interacción de los electrones con la materia,» [En línea]. Available: <https://ssyf.ua.es/es/formacion/documentos/cursos-programados/2012/especifica/tecnicas-instrumentales-en-el-analisis-de-superficie/sem-sesion-12-de-noviembre.pdf>. [Último acceso: 01 February 2018].
- [73] C. C. Chang, «Auger electron spectroscopy,» *Surface Science*, vol. 25, pp. 53-79, 1971.

- [74] G. Binning, C. F. Quate y C. Gerber, «Atomic Force Microscope,» *Phys. Rev. Lett.*, vol. 56, p. 930, 1986.
- [75] Wikipedia, «Potencial de Lennard-Jones,» 2008. [En línea]. Available: https://es.wikipedia.org/wiki/Potencial_de_Lennard-Jones. [Último acceso: 28 April 2018].
- [76] The University of Utah, «Lecture 10: Basics of Atomic Force Microscopy (AFM),» The Zang Research Group, [En línea]. Available: http://www.eng.utah.edu/~lzang/images/Lecture_10_AFM.pdf. [Último acceso: 28 April 2018].
- [77] T. M. Pan, T. F. Lei y T. S. Chao, «Comparison of ultrathin CoTiO₃CoTiO₃ and NiTiO₃NiTiO₃ high-k gate dielectrics,» *J. Appl. Phys.*, vol. 89, p. 3447, 2001.
- [78] H. Y. He, «Humidity sensitivity of CoTiO₃ thin film prepared by sol-gel method,» *Mater. Technol.*, vol. 22, n° 2, pp. 95-97, 2007.
- [79] A. Askarinejad, M. Bagherzadeh y A. Morsali, «Catalytic performance of Mn₃O₄ and Co₃O₄ nanocrystals prepared by sonochemical method in epoxidation of styrene and cyclooctene,» *Appl. Surf. Sci.*, vol. 256, pp. 6678-6682, 2010.
- [80] S. Farhadi, J. Safabakhsh y P. Zaringhadam, «Synthesis, characterization, and investigation of optical and magnetic properties of cobalt oxide (Co₃O₄) nanoparticles,» *Journal Of Nanostructure in Chemistry*, vol. 3, n° 1, p. 69, 2013.
- [81] ChemTube 3D, «Inner Sphere Electron Transfer Mechanism,» UK Physical Sciences Centre, [En línea]. Available: <http://www.chemtube3d.com/TM-innersphere.htm>. [Último acceso: 29 April 2018].
- [82] H. Mueller-Buschbaum y M. Waburg, «Pseudobrookite mit weitgehend geordneter Metallverteilung: CoTi₂O₅, MgTi₂O₅ und FeTi₂O₅,» *Monatshefte fur Chemie*, vol. 114, pp. 21-25, 1983.
- [83] B. Brezny y A. Muan, «Phase Relations and Stabilities of Compounds in the System CoO-TiO₂,» *J. Inorg. nucl. Chem.*, vol. 31, pp. 649-655, 1969.
- [84] A. M. Balbashov, A. A. Mukhin, V. Y. Ivanov, L. D. Iskhakova y M. E. Voronchikhina, «Electric and magnetic properties of titanium-cobalt-oxide single crystals produced by floating zone melting with light heating,» *Low temperature physics*, vol. 43, n° 8, pp. 1200-1206, 2017.
- [85] J. Li, C. H. Sow, X. S. Rao, C. K. Ong y D. N. Zheng, «Epitaxial growth and magnetic and electric properties of Co-doped TiO₂ thin films,» *Eur. Phys. J. B*, vol. 32, pp. 471-476, 2003.
- [86] B. S. Jeong, «EPITAXIALLY GROWN ANATASE COXTI₁-XO₂,» de *GROWTH AND FERROMAGNETIC SEMICONDUCTING PROPERTIES OF TITANIUM DIOXIDE THIN FILMS: AN OXIDE-DILUTED MAGNETIC SEMICONDUCTOR (O-DMS) FOR SPINTRONICS*, Florida, University of Florida, 2004, p. 88.
- [87] V. F. Agekyan, «Intracenter Transitions of Iron-Group Ions in II-VI Semiconductor Matrices,» *Physics of the Solid State*, vol. 44, n° 11, pp. 2013-2030, 2002.

- [88] K. A. Kikoin y V. N. Fleurov, «THEORY OF DEEP LEVELS IN SEMICONDUCTORS DOPED BY TRANSITION METAL IMPURITIES,» de *Transition Metal Impurities in Semiconductors*, World Scientific, 1994, pp. 75-85.
- [89] J. Mujtaba, H. Sun, G. Huang, K. Molhave, Y. Liu, Y. Zhao, X. Wang, S. Xu y J. Zhu, «Nanoparticle Decorated Ultrathin Porous Nanosheets as Hierarchical Co₃O₄ Nanostructures for Lithium Ion Battery Anode Materials,» *Scientific reports*, vol. 6, p. 20592, 2016.
- [90] NIST, «NIST X-ray Photoelectron Spectroscopy Database,» [En línea]. Available: https://srdata.nist.gov/xps/main_search_menu.aspx. [Último acceso: 28 April 2018].
- [91] A. Younis, D. Chu, X. Lin, J. Lee y S. Li, «Bipolar resistive switching in p-type Co₃O₄ nanosheets prepared by electrochemical deposition,» *Res. Lett.*, vol. 8, n^o 1, p. 36, 2013.
- [92] S. C. Petitto y M. A. Langell, «Surface composition and structure of Co₃O₄,110) and the effect of impurity segregation,» *J. Vac. Sci. Technol. A*, vol. 22, n^o 4, pp. 1690-1696, 2004.
- [93] A. Earnshaw y N. Greenwood, «Cobalt, Rhodium and Iridium,» de *Chemistry of the Elements*, Oxford, Butterworth-Heinemann, 1997, pp. 1113-1143.
- [94] Chemistry LibreTexts Library, «Chapter 8: Ionic and Covalent Solids - Structures,» [En línea]. Available: [https://chem.libretexts.org/Textbook_Maps/Inorganic_Chemistry_Textbook_Maps/Map:_Inorganic_Chemistry_\(Wikibook\)](https://chem.libretexts.org/Textbook_Maps/Inorganic_Chemistry_Textbook_Maps/Map:_Inorganic_Chemistry_(Wikibook)). [Último acceso: 28 April 2018].
- [95] M. Marolt, *Superparamagnetic materials*, Kranj: University of Ljubljana, 2014.
- [96] H. M. Rietveld, «Line profiles of neutron powder-diffraction peaks for structure refinement,» *Acta Crystallogr.*, vol. 22, pp. 151-152, 1967.
- [97] T. R. Hammad, «Does the two-step resistive transition represent an intrinsic property of electron-doped cuprates?,» *Int. J. Mod. Phys. B*, vol. 21, n^o 7, pp. 1051-1058, 2007.
- [98] C. W. Haworth, «Measurement of the Debye-Waller temperature factor for silver and α -iron,» *Philos. Mag.*, vol. 5, n^o 60, pp. 1229-1234, 1960.
- [99] A. W. Rutherford y A. Boussac, «Water Photolysis in Biology,» *Science*, vol. 303, pp. 1782-1784, 2004.